INSTITUTE OF PHYSICS, POLISH ACADEMY OF SCIENCES

DOCTORAL THESIS

Topological properties of selected IV-VI semiconductor nanostructures

---

Author:
Saeed SAMADI BAHNEMIRI

Supervisor:
Prof. dr hab.
Ryszard BUCZKO

June 2023

The research is supported by the Polish National Science Centre (NCN) Grant under project No. 2016/23/B/ST3/03725. Computations were carried out using the computers of Centre of Informatics Tricity Academic Supercomputer & networK (CI TASK).

Abstract

In this thesis, the results of a research on the topological properties of selected nanostructures made of IV-VI materials are presented. Some binary and ternary IV-VI crystals have an inverted band gap and belong to the class of topological crystalline insulators (TCI). As a result of the non-trivial topology of electronic band states, they have an even number of gapless states with Dirac cone dispersion on their surfaces. Remarkable experimental achievements obtained for SnTe and its ternary crystalline solid solutions, such as (Pb,Sn)Te/Se, confirmed the existence of non-trivial surface states. They have stimulated extensive research efforts not only on bulk crystals but also on nanostructures and defects in recent years. Here the results of theoretical studies on nanostructures with defects in the form of (111) oriented twin planes (TP) are discussed. The discussion focuses on three different types of nanostructures. These are super-lattices, thin films and nanowires. In the case of films and wires, the obtained results are compared with the properties of similar structures without defects. The analysis of the results reveals that TPs can be treated as two-dimensional topological structures belonging to the TCI class which are protected by the (111) mirror symmetry. The value of the topological invariant - the mirror Chern number - depends on the type of twinning and is equal to 1 for an anionic TP and to 2 for cationic one. It is also shown that at the one-dimensional edges of these structures, the expected number of topologically protected non-trivial boundary states appears. However, in sufficiently thin film with surface orientation (111) having a TP defect in the middle, the topological effect is destroyed by a hybridization of the electronic surface states with the states located on the defect. The protected edge states still appear and show the quantum spin Hall effect, that is only due to the existence of the same $\mathbb{Z}_2$ invariant that defines the topology of non-defective structures. In the second part of the thesis, the topological properties of a pentagonal SnTe quantum wire are described. Its cross-section shape comes out from the existence of five TPs extending radially from the center. The wire has two non-trivial electronic states: one located in its center and another one located on its five edges. It is established that their presence is related to the topological properties of TPs. The result has been compared with the properties of a wire with a square cross-section, where the edge states are of a different nature; these are topological states of the second order - hinge states. It is shown that they are not as robust against hybridization as the edge states in wires with an odd number of edges.

Streszczenie

W niniejszej pracy przedstawione są wyniki badań właściwości topologicznych wybranych nanostruktur utworzonych z materiałów IV-VI. Niektóre dwu i trzy składnikowe kryształy IV-VI maja odwróconą przerwę energetyczną i należą do klasy topologicznych izolatorów krystalicznych (TCI). W wyniku nietrywialnej topologii elektronowych stanów pasmowych posiadają one parzystą liczbę bezprzerwowych stanów o dyspersji w kształcie stożków Diraca na swoich powierzchniach. Niezwykłe osiągnięcia eksperymentalne otrzymane dla SnTe i jego trójskładnikowych krystalicznych roztworów stałych, takich jak (Pb,Sn)Te/Se, potwierdziły istnienie nietrywialnych stanów powierzchniowych. Pobudziły one w ostatnich latach szeroko zakrojone wysiłki badawcze dotyczące nie tylko kryształów objętościowych ale również nanostruktur i defektów. Tutaj omówione są wyniki badań teoretycznych dotyczących nanostruktur posiadających defekty w postaci zbliźniaczeń (TP) w płaszczyźnie (111). Używając metod ciasnego wiązania badaliśmy trzy różne rodzaje nanostruktur. Są to super-sieci, cienkie filmy oraz nanodruty. W przypadku filmów i drutów otrzymane wyniki porównane zostały z własnościami podobnych struktur bez defektów. Analiza wyników pokazuje że TP mogą być traktowane jako dwuwymiarowe struktury topologiczne należące do klasy TCI i chronione przez symetrię odbicia zwierciadlanego (111). Wartość niezmiennika topologicznego – zwierciadlana liczba Cherna - zależy od rodzaju zbliźniaczenia i wynosi 1 dla TP anionowego i 2 dla TP kationowego. Pokazano także że na jednowymiarowych krawędziach tych struktur pojawia się spodziewana liczba chronionych topologicznie nietrywialnych stanów brzegowych. Jednak w odpowiednio cienkich warstwach o orientacji powierzchni (111) posiadających defekt TP w środkowej warstwie atomowej efekt topologiczny zostaje zniszczony przez hybrydyzację stanów elektronowych powierzchni ze stanami zlokalizowanymi na defekcie. Chronione stany brzegowe wciąż istnieją i wykazują kwantowy spinowy efekt Hala, jedynie dzięki istnieniu takiego samego niezmiennika $\mathbb{Z}_2$ jaki wyznacza topologię struktur niezdefektowanych. W drugiej części opisane zostały własności topologiczne drutu kwantowego o przekroju pięciokątnym. Kształt jego przekroju wynika z istnienia pięciu TPs rozchodzących się promieniście od środka. Drut posiada dwa nietrywialne stany elektronowe: jeden zlokalizowany w samym jego środku oraz drugi zlokalizowany na jego pięciu krawędziach. Ich istnienie związane jest z własnościami topologicznymi zbliźniaczeń. Wynik został porównany z własnościami drutu o przekroju czworokątnym gdzie istnienie stanów krawędziowych ma inny charakter, są to stany topologiczne drugiego rzędu – stany zawiasowe. Pokazano że nie są one tak odporne na hybrydyzację

jak stany krawędziowe w drutach o nieparzystej liczbie krawędzi.

To my dear parents and friends

Acknowledgements

First and foremost, I would like to sincerely express my gratitude to my supervisor, **Prof. Ryszard Buczko**, for providing me with the opportunity to pursue my PhD. I am immensely grateful for his precious advice, helpful suggestions, and support. I deeply appreciate his patience and encouragement in addressing any challenges I encountered throughout my research.

I would like to thank my office-mate, **Rafał Rechciński**, for his helpful suggestions, insightful discussions, and profound knowledge in condensed matter physics. Collaborating with him has been a truly enjoyable experience. I also express my gratitude to him for granting me access to the analysis he conducted, which has been incorporated into the thesis.

I extend my deep appreciation to my colleague, **Dr. Marta Chabowska**, for her unwavering willingness to help and her kindness. Her support has been invaluable throughout my journey.

I want to express my heartfelt gratitude to my best friend, **Houri Rahimi Mosafer**, for her constant companionship and support. Your friendship has meant the world to me, and I am grateful for your presence every step of the way.

Last but not the least, everything we are today and everything we may become tomorrow, is all for the sacrifices our parents made for us. I would like to thank my dear parents for supporting me throughout of my life. I am truly blessed to have you all. I could not have undertaken this journey without your supports.

Contents

List of Figures

List of Tables

Nomenclature

■ Abbreviations

1D, 2D, ...	one-dimensional, two-dimensional, ...
ARPES	angle resolved photo emission spectroscopy
BZ	Brillouin Zone
DFT	density functional theory
HOTI	higher-order topological insulator
QHE	quantum Hall effect
QSHE	quantum spin Hall effect
SK	Slater-Koster
SOC	spin-orbit coupling
TB	tight-binding
TCI	topological crystalline insulator
TI	topological insulator
TP	twin plane
TRIM	time-reversal invariant momentum
TRS	time-reversal symmetry
TSL	twinning superlattice
VCA	virtual crystal approximation

■ Symbols

$\mathcal{A}$	Berry connection
Ω	Berry curvature
γ	Berry phase
C	Chern number
F_{12}	field strength
C_m	mirror Chern number
Θ	time-reversal operator
$\mathbb{Z}_2$	topological invariant

Chapter 1

Introduction

Landau's symmetry-breaking theory, proposed in the 1930s, was highly esteemed as a potent tool for comprehending phase transitions in quantum states of matter. It provided a unique order parameter that arises from spontaneous symmetry breaking. This theory ultimately culminating in the formulation of the Landau-Ginzburg theory and serves as a universal framework for understanding quantum states of matter. However, the quantum Hall effect's groundbreaking discovery in the 1980s [1] disrupted the prevailing viewpoint. The subsequent experimental identification of the integer quantum Hall effect (IQHE), coupled with its profound interpretation as a topological phenomenon by Thouless et al. [2], marked a paradigm shift in our comprehension.

In mathematics, topological classification disregards intricate geometric details and instead focuses on the examination of global characteristics employing topological invariants. One prominent tool in distinguishing topologically distinct objects is the Gauss-Bonnet theorem, which ascribes a numerical value known as the genus to quantify the presence of holes. To illustrate, a sphere can be smoothly transformed into a disk or a bowl, thus demonstrating topological equivalence. Conversely, the transformation of a sphere into a torus necessitates the introduction of a hole, rendering it a non-smooth process. It is worth noting that the genus remains invariant under continuous deformations. In a significant contribution, Thouless, Kohmoto, Nightingale, and den Nijs [2] established a connection between the Hall conductivity in systems exhibiting the IQHE and a topological invariant known as the Chern number. Remarkably, the Chern number illustrates the number of gapless states present at the boundaries of the system.

In subsequent developments, in 1984, M. Berry presented an extensive generalization of the notion of the geometric phase, now widely recognized as the Berry phase. This seminal work shed light on the profound significance of geometric phases as a unifying framework in various domains of classical and quantum physics, with particular relevance to the modern band theory. Haldane's work in 1988 [3] demonstrated that quantum

Hall states, now referred to as Chern insulators, can exist without a net magnetic field. This discovery established the connection between the quantum Hall effect and band theory, highlighting the role of time-reversal symmetry breaking in maintaining the crystal's periodicity. This novel understanding provided valuable insights into the interplay between topology and condensed matter physics, paving the way for further exploration of topological phases in various systems. In 2005, Kane and Mele demonstrated topology without breaking time-reversal symmetry, initially proposed in graphene but limited by insufficient intrinsic spin-orbit coupling (SOC). However, in 2006, Bernevig, Hughes, and Zhang proposed a HgTe/CdTe quantum well, enabling the realization of a quantum spin Hall insulator (QSHI). This breakthrough introduced a novel state of matter with a gap and helical edge states. Subsequently, the two-dimensional topological insulator (TI) commonly known as QSH insulator was experimentally confirmed, characterized by a distinct topological invariant known as the $\mathbb{Z}_2$ index. The $\mathbb{Z}_2$ TIs further expanded to three dimensions, firstly predicted in $Bi_{1-x}Sb_x$ by Fu and Kane in 2007. In 2008, its experimental observation was validated through angle-resolved photoemission spectroscopy (ARPES) [4], along with the discovery of other bismuth-based materials [5, 6].

Advancing in this field, beyond time-reversal symmetry in TIs, the significance of other symmetries in determining topological classifications became apparent. In 2011, L. Fu expanded the range of topological phases by establishing the relationship between topology and spatial symmetries within crystal structures. An exemplary realization of a topological phase with spatial symmetries is found in the SnTe class of IV-VI rocksalt semiconductors. The Dirac-like gapless surface states of these materials are protected by mirror symmetry [7–10]. In this class, the topological classification of the band structure critically relies on specific crystal point group symmetries. Consequently, a topological crystalline insulator (TCI) cannot be smoothly transformed into a normal insulator while preserving certain crystal symmetries. A notable aspect of TCI materials is their ability to tune topological properties through various perturbations, including structural distortion, magnetic doping, mechanical strain, thickness engineering, and disorder. For instance, (111) thin films were anticipated to exhibit a QSH phase [11, 12], while (001) films were found to feature spin-filtered edge states [13], holding potential for applications in topological transistors. Additionally, experimental observations unveiled one-dimensional gapless modes localized at atomic step edges on the (001) surface

[14–16]. Remarkably, in the SnTe class of materials, a distinctive higher-order TIs (HOTIs) phase has been discovered, signifying a recently acknowledged category of topological phases. These HOTIs exhibit lower-dimensional boundary states, including zero-dimensional corner states and one-dimensional hinge states [17]. Nonetheless, the comprehensive classification of TCIs continues to be an ongoing area of research due to the intricate and multifaceted nature of crystallography [18].

The current thesis focuses on examining the topological properties of specific nanostructures of SnTe material class through theoretical calculations. The results of current study are established in Chapter 5. The thesis is structured as follows:

Chapter 2 devotes as an introductory section on topological band theory. It begins by providing key definitions related to band topology and discusses the fundamental concepts of Berry phase and its application to Bloch bands. Important topological invariants, which are discussed throughout the study, are derived, and several examples of models representing various topological classes are presented. Chapter 3 provides a comprehensive review of progressive investigations on IV-VI TCI materials. The focus is primarily on the SnTe class of topological crystalline phases, which have been extensively studied both experimentally and theoretically. In Chapter 4, the TB model is presented as a essential theoretical tools for the calculations. Accordingly, the electronic band structure, topological invariants, and spectral Green's functions are computed using this model. Chapter 5 contains the main results of the current study and divided into three main research directions. In Chapter 5.1 and 5.2, we analyze the impact of lattice twin planes (TP) on the electronic band structure topology within the context of twinning superlattice (TSL) and slab implementations. It is demonstrated in a comprehensive manner that TPs, which occur as defects in crystals, effectively act as two-dimensional (2D) topological objects. Two types of TPs, cationic and anionic, are identified as topologically distinct phases. In Chapter 5.3, the topological properties of (111)-oriented SnTe thin films with a TP are explored. We discuss how the presence of TP in the regime of gapped surface states due to a finite-size effect can influence the topological phase transition as the thickness grows. Lastly, in Chapter 5.4, we explore TCI nanowires (NWs) based on IV-VI semiconductors. It is shown that the presence of TPs in pentagonal NWs leads to the emergence of one-dimensional (1D) topological core states (TCS) at the NW core in the cationic case with their counterparts at hinges.

Chapter 2

Topological states of matter

This chapter introduces the important principles of the topological state of matter using the mathematical field of topology. These ideas are demonstrated within the broader context of band theory in the tight-binding formalism. Through the use of paradigmatic examples, the classification of topological phases based on various symmetry classes is examined and discussed.

2.1 Topology

Topology, a branch of mathematics, examines the properties of smooth and continuous transformations. It does not concern itself with the precise geometric features of objects, but rather concentrates on their general characteristics, represented by topological invariants. For instance, a sphere can be continuously transformed into a bowl or cube, demonstrating their topological equivalence or homeomorphism. However, converting a sphere into a torus is not a smooth procedure as it requires creating a hole [19].

Surfaces that can be deformed into one another are considered topologically equivalent. To differentiate between distinct topological objects, one can assign a number called the genus (g) representing the count of holes, as explained in Gauss-Bonnet theorem [20]. As shown in Fig. 2.1, a sphere has a genus of $g = 0$, whereas a torus has $g = 1$. The genus remains unchanged as long as all deformations are smooth.

2.2 Band Theory

Insulators are materials that exhibit an energy gap for electronic excitations, which separates the ground state from all excited states. The principle of adiabatic continuity gives rise to the concept of topological equivalence. The insulators are considered equivalent if we can transform one into another by continuously modifying the Hamiltonian while

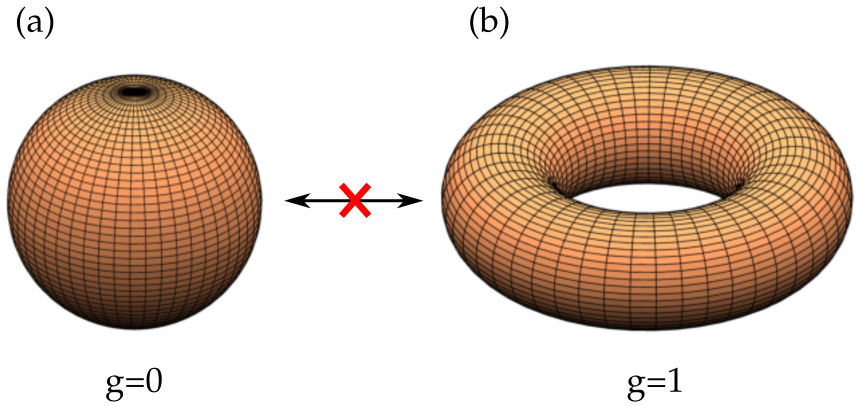

Figure 2.1: Topological distinction between a sphere and a torus. A sphere has a genus, $g = 0$, while a torus possesses a single punctured hole, resulting in $g = 1$.

keeping the system in the ground state throughout the entire process. Such a transformation is possible if there exists an energy gap (E_G) along the deformation process. As a consequence, connecting topologically distinct insulators necessarily involves a phase transition, where the energy gap vanishes.

To comprehend topological equivalence in band theory, one can analyze two band insulators described by Bloch Hamiltonians: $H(\boldsymbol{k})$ and $H'(\boldsymbol{k})$. The main question is whether it is feasible to adiabatically deform one insulator into the other while maintaining the energy gap. Let us consider a single-particle tight-binding Hamiltonian having translation invariance under a Bravais lattice. Translation symmetry enables the identification of single-particle states through their crystal momentum, denoted as $\boldsymbol{k}$. According to Bloch's theorem, they may be written $|\psi\rangle = e^{i\boldsymbol{k}\cdot\mathbf{r}}|u(\boldsymbol{k})\rangle$, where $|u(\boldsymbol{k})\rangle$ is a cell periodic eigenstate of the Bloch Hamiltonian [21],

$$H(\boldsymbol{k}) = e^{i\boldsymbol{k}\cdot\mathbf{r}} H e^{-i\boldsymbol{k}\cdot\mathbf{r}}, \tag{2.1}$$

where $\mathbf{r}$ is the position operator and $\boldsymbol{k}$ is a parameter with the dimension of a wave vector. In the following, we will refer to it as the canonical Bloch Hamiltonian or simply the Bloch Hamiltonian. Bloch's theorem allows us to diagonalize the Hamiltonian as

$$H|\psi_{n,\boldsymbol{k}}\rangle = E_n(\boldsymbol{k})|\psi_{n,\boldsymbol{k}}\rangle. \tag{2.2}$$

Within an insulating band structure, there exists an energy gap that separates the highest occupied band from the lowest empty band. The presence of lattice translation symmetry imposes the condition $H(\boldsymbol{k} + \boldsymbol{G}) = H(\boldsymbol{k})$ for reciprocal lattice vectors $\boldsymbol{G}$. Consequently, the crystal momentum is defined within the periodic BZ, indicated as $\boldsymbol{k} \equiv \boldsymbol{k} + \boldsymbol{G}$, exhibiting the topological structure of a torus T^d in d dimensions.

2.3 Bulk-boundary correspondence

The intriguing physics emerges when the material boundaries are considered. Topological materials exhibit distinct properties in both their bulk and boundary regions that are specific to the system. Knowing the bulk properties, one can topologically classify the Hamiltonian $H(\mathbf{k})$ using band theory. This classification becomes evident when determining the value of a nontrivial topological invariant. When the symmetries that govern the relevant topological invariant are maintained at the boundary of a system, it signifies the existence of topologically protected states. This phenomenon arises when there is a spatial interface between two phases that possess distinct topological properties. It ensures that at some point along the pathway between the two systems, the energy gap must reach zero. Otherwise, the two phases would be considered equivalent [22].

The topological band theory is intended to characterize these boundary modes, and one concrete explanation for why the bulk-boundary correspondence relates the boundary modes to the difference in bulk topological invariants is as follows. Let's assume two semi-infinite systems L and R illustrated in Fig. 2.2 are connected and construct an interface. Each individual system has similar topological classification (both are characterized by index n) but the values of their invariants are different $n_L \neq n_R$. As a topological invariant can only change if the bulk gap closes and no relevant symmetries are broken, a topological phase transition between two distinct gapped systems must be accompanied by the local gap closing. As a consequence, gapless states localize at the interface of the two materials and their number depends on the difference between indices $|n_L - n_R|$.

The connection between topology and possible existence of gapless modes is an interesting phenomenon in physics, and has appeared in many contexts [23–27] and rigorous studies conducted on several symmetry classes [28–30]. In addition, most often, the bulk-boundary correspondence refers to the relation between d-dimensional bulk and boundary modes in $(d-1)$-dimensions [31]. However, topological lines and point defects can be also predicted from the periodic table obtained for classification of topological defects in insulators and superconductors [32]. Furthermore, another extension of the correspondence was established for the so-called higher-order topological insulators, in which the boundary states are unveiled in codimensions $(d-D)$, with $D > 1$ [33].

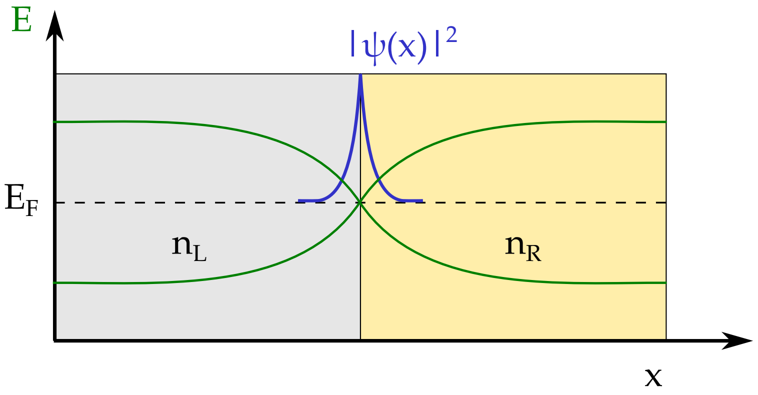

Figure 2.2: Schematic representation of the bulk-boundary correspondence. If two systems L and R, characterized by the invariants n_L and n_R ($n_L \neq n_R$), are joined at interface, there have to be gapless states localized at a domain wall associated with a band gap closing. The number of boundary states is determined by the difference $|n_L - n_R|$.

2.4 Basic concepts of the Berry phase

M. V. Berry played a pivotal role in establishing the groundwork for comprehending topological properties in solid-state physics. In his work [34] he introduced the geometrical phase accompanying adiabatic changes. If a cyclic evolution is considered, an accumulated phase can have a purely geometric character with potentially observable consequences. This phase, now called Berry phase, and the connected quantities, Berry connection and curvature, are used for calculating the so called topological invariants, which themselves allow to distinguish between specific topology classes.

In this section we will provide a background to some of the physical concepts that will be of importance in this thesis. We shall among other things refer and describe phenomenon utilizing Berry's quantities [35].

2.4.1 Cyclic adiabatic evolution

Consider a physical system described by a Hamiltonian that depends on time through a set of parameters, denoted by $\boldsymbol{R} = (R_1, R_2, \ldots)$, i.e.,

$$H = H(\boldsymbol{R}), \quad \boldsymbol{R} = \boldsymbol{R}(t)\,. \tag{2.3}$$

We are interested in studying the adiabatic evolution of the system as $\boldsymbol{R}(t)$ slowly moves along a path $\mathcal{C}$ in the parameter space. To facilitate this analysis, it is beneficial to introduce an instantaneous orthonormal basis composed of the eigenstates of $H(\mathbf{R})$ at each value of the parameter $\boldsymbol{R}$, i.e.,

$$H(\boldsymbol{R})|n(\boldsymbol{R})\rangle = \varepsilon(\boldsymbol{R})|n(\boldsymbol{R})\rangle. \tag{2.4}$$

However, Eq. (2.4) alone does not fully specify the basis function $|n(\boldsymbol{R})\rangle$ as it allows for an arbitrary $\boldsymbol{R}$-dependent phase factor of $|n(\boldsymbol{R})\rangle$. To resolve this ambiguity, a phase choice, also known as a gauge, can be made. In this case, we require that the phase of the basis function remains smooth and single-valued along the path $\mathcal{C}$ in the parameter space. [1]

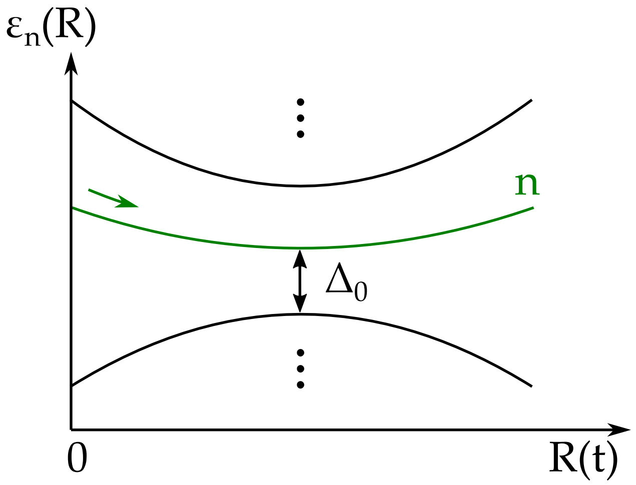

Figure 2.3: If a Hamiltonian varies slowly with time, then an electron at state $|n(\boldsymbol{R})\rangle$ would stay at the same energy level.

Suppose the energy level $\varepsilon_n(\boldsymbol{R})$ remains separated by a energy gap Δ_0 from other levels during the evolution [2]. According to the adiabatic theorem [36, 37], a system initially in one of its eigenstates $|n(\boldsymbol{R}(0))\rangle$ will remain in the same energy level n of the Hamiltonian $H(\boldsymbol{R})$ throughout the process as depicted in Fig. 2.3. Therefore, the only degree of freedom that changes is the phase of the quantum state. We can express the state at time t as

$$|\psi_n(t)\rangle = e^{i\gamma_n(t)} \exp\left[-\frac{i}{\hbar}\int_0^t dt'\varepsilon_n(\boldsymbol{R}(t'))\right]|n(\boldsymbol{R}(t))\rangle\,, \tag{2.5}$$

where the second exponential term is referred to as the dynamical phase factor. By substituting Eq. (2.5) into the time-dependent Schrödinger equation, we obtain

$$i\hbar\frac{\partial}{\partial t}|\psi_n(t)\rangle = H(\boldsymbol{R}(t))|\psi_n(t)\rangle \tag{2.6}$$

---

[1] It is important to note that such a phase choice is guaranteed only in finite neighborhoods of the parameter space. In the general case, the path can be divided into several overlapping neighborhoods, and the wave functions in the overlapping region are related by a gauge transformation of the form $|n(\boldsymbol{R})\rangle \to e^{i\zeta(\boldsymbol{R})}|n(\boldsymbol{R})\rangle$.

[2] It is important to note that the Berry phase descriptions in this section rely on non-degenerate energy levels (Abelian case).

and multiplying it on the left by $\langle n(\mathbf{R}(t))|$, one can express γ_n as a path integral in the parameter space [35]

$$\gamma_n = \int_{\mathcal{C}} d\boldsymbol{R} \cdot \mathcal{A}_n(\boldsymbol{R}) \,, \tag{2.7}$$

where $\mathcal{A}_n(\boldsymbol{R})$ is a vector-valued function

$$\mathcal{A}_n(\boldsymbol{R}) = i\langle n(\boldsymbol{R})|\frac{\partial}{\partial \boldsymbol{R}}|n(\boldsymbol{R})\rangle \,. \tag{2.8}$$

The quantity $\mathcal{A}_n(\boldsymbol{R})$ is known as the Berry connection or the Berry vector potential. Equation (2.7) demonstrates that, apart from the dynamical phase, the quantum state will acquire an additional phase γ_n during the adiabatic evolution.

Obviously, $\mathcal{A}_n(\boldsymbol{R})$ is gauge dependent. When we perform a gauge transformation

$$|n(\boldsymbol{R})\rangle \rightarrow e^{i\zeta(\boldsymbol{R})}|n(\boldsymbol{R})\rangle \tag{2.9}$$

with $\zeta(\boldsymbol{R})$ being an arbitrary smooth function and $\mathcal{A}_n(\boldsymbol{R})$ transforming according to

$$\mathcal{A}_n(\boldsymbol{R}) \rightarrow \mathcal{A}_n(\boldsymbol{R}) - \frac{\partial}{\partial \boldsymbol{R}}\zeta(\boldsymbol{R}) \,. \tag{2.10}$$

Consequently, the phase γ_n given by Eq.(2.7) will be altered by $\zeta(\boldsymbol{R}(0)) - \zeta(\boldsymbol{R}(T))$ after the transformation, where $\zeta(\boldsymbol{R}(0))$ and $\zeta(\boldsymbol{R}(T))$ represent the initial and final points of the path $\mathcal{C}$. This observation has led to the conclusion that one can always choose a suitable $\zeta(\boldsymbol{R})$ such that the accumulated phase γ_n along the path $\mathcal{C}$ is canceled out, thereby leaving Eq.(2.5) with only the dynamical phase. As a result, the phase γ_n has long been considered unimportant and has typically been neglected in the theoretical treatment of time-dependent problems.

This conclusion remained unchallenged until the reconsideration of the cyclic evolution of the system along a *closed path* $\mathcal{C}$ with $\boldsymbol{R}(T) = \boldsymbol{R}(0)$ [34]. The previous phase choice made on the basis function $|n(\boldsymbol{R})\rangle$ required $e^{i\zeta(\boldsymbol{R})}$ in the gauge transformation [Eq. (2.9)] to be single-valued. Therefore, for a closed path, γ_n is well-defined and becomes a gauge-invariant physical quantity, now known as the *Berry phase*, given by

$$\gamma_n = \oint_{\mathcal{C}} d\boldsymbol{R} \cdot \mathcal{A}_n(\boldsymbol{R}) \,. \tag{2.11}$$

Therefore, it is impossible to eliminate $\mathcal{A}_n(\boldsymbol{R})$ through any gauge transformation, analogous to the situation in quantum electrodynamics where an electron moving in a magnetic field acquires a phase in the well-known Aharonov-Bohm experiment [38].

2.4.2 Berry curvature

It is useful to define a gauge-field tensor from the Berry vector potential for a given non-degenrate band n as:

$$\begin{aligned}\Omega^n_{\mu\nu}(\boldsymbol{R}) &= \partial_{R^\mu}\mathcal{A}^n_\nu(\boldsymbol{R}) - \partial_{R^\nu}\mathcal{A}^n_\mu(\boldsymbol{R}) \\ &= i\left[\langle\partial_{R^\mu}n(\boldsymbol{R})|\partial_{R^\nu}n(\boldsymbol{R})\rangle - (\nu \leftrightarrow \mu)\right] .\end{aligned} \tag{2.12}$$

This field is called the Berry curvature. According to Stokes's theorem, after performing a gauge transformation, the Berry phase can be expressed as a surface integral

$$\gamma_n = \int_{\mathcal{S}} dR^\mu \wedge dR^\nu \frac{1}{2}\Omega^n_{\mu\nu} , \tag{2.13}$$

where $\mathcal{S}$ represents an arbitrary surface that is enclosed by the path $\mathcal{C}$. If the parameter space is three dimensional, Eqs. (2.12) and (2.13) can be recast into a vector form

$$\boldsymbol{\Omega}_n(\boldsymbol{R}) = \nabla_{\boldsymbol{R}} \times \mathcal{A}_n(\boldsymbol{R}) , \tag{2.14}$$

$$\gamma_n = \int_{\mathcal{S}} d\mathbf{S} \cdot \boldsymbol{\Omega}_n(\boldsymbol{R}) . \tag{2.15}$$

The Berry curvature tensor $\Omega^n_{\mu\nu}$ and vector $\boldsymbol{\Omega}_\mathbf{n}$ are related by $\Omega^n_{\mu\nu} = \epsilon_{\mu\nu\xi}(\boldsymbol{\Omega}_n)_\xi$ with Levi-Cività antisymmetry tensor. The vector provides an intuitive insight of the Berry curvature, as it can be regarded as the magnetic field in the parameter space.

Besides the differential formula given in Eq. (2.12), the Berry curvature can also be expressed as a summation over the eigenstates

$$\Omega^n_{\mu\nu}(\boldsymbol{R}) = i\sum_{m\neq n}\frac{\langle n(\boldsymbol{R})|\partial_{R^\mu}H(\boldsymbol{R})|m(\boldsymbol{R})\rangle\langle m(\boldsymbol{R})|\partial_{R^\nu}H(\boldsymbol{R})|n(\boldsymbol{R})\rangle - (\nu \leftrightarrow \mu)}{\left(\varepsilon_n(\boldsymbol{R}) - \varepsilon_m(\boldsymbol{R})\right)^2} . \tag{2.16}$$

The summation formula has the advantage that it does not involve differentiation of the wave function, making it applicable under any gauge choice. Unlike the Berry vector potential, the Berry curvature is gauge invariant and therefore observable. This equation can be directly used for numerical evaluation of the Berry curvature, as it only requires input such as eigenstates, eigenvalues, and the gradient of the Hamiltonian.

The dependence of the Berry curvature on the energy spectrum can be seen in Eq. (2.16). The presence of $\varepsilon_n(\boldsymbol{R}) - \varepsilon_m(\boldsymbol{R})$ in the denominator implies that the Berry curvature becomes large value when the energy levels are close to each other. The divergence of $\boldsymbol{\Omega}_n$

occurs when there are degenerate states. This degeneracy at a specific value of $\boldsymbol{R}$ corresponds to a monopole in the parameter space. It is important to note that the discussion thus far has focused on scenarios where a single energy level can be distinguished during adiabatic evolution. However, the analysis can be extended to include degenerate energy levels, where the wave function consists of multiple components for a given energy level [39].

2.5 Berry phase in Bloch bands

In previous section, the Berry phase and related quantities were discussed for a generic system described by a parameter-dependent Hamiltonian. When considering its manifestation in crystalline solids, the band structure of crystals provides a natural platform to investigate the occurrence of the Berry phase effect. It will be demonstrated that in lattice-periodic crystals, the wave vector $\boldsymbol{k}$ plays the role of the parameter $\boldsymbol{R}$ [40].

We will start by invoking the Bloch theorem [41] within the framework of the independent electron approximation under the influence of a periodic potential $V(\boldsymbol{r}) = V(\boldsymbol{r}+\boldsymbol{t})$, where $\boldsymbol{t}$ is Bravais lattice vector. Bloch's theorem allows us to label each eigenstate of the Hamiltonian H by a pair of quantum numbers $(n, \boldsymbol{k})$, belonging to the first BZ. The one-electron wave function then satisfies

$$\psi_{n,\boldsymbol{k}}(\boldsymbol{r}) = e^{i\boldsymbol{k}\cdot\boldsymbol{r}} u_{n,\boldsymbol{k}}(\boldsymbol{r})\,. \tag{2.17}$$

In Eq. (2.17), each eigenstate $\psi_{n,\boldsymbol{k}}(\boldsymbol{r})$ corresponds to a Bloch wave, where $u_{n,\boldsymbol{k}}(\boldsymbol{r})$ represents the lattice-periodic part of the wave function with the same periodicity as the Bravais lattice of the crystal, i.e., $u_{n,\boldsymbol{k}}(\boldsymbol{r}) = u_{n,\boldsymbol{k}}(\boldsymbol{r}+\boldsymbol{t})$. By substituting the Bloch wave function given in Eq. (2.17) into the time-independent Schrödinger equation $H\psi_{n,\boldsymbol{k}}(\boldsymbol{r}) = E_{n,\boldsymbol{k}}\psi_{n,\boldsymbol{k}}(\boldsymbol{r})$ and multiplying it by $e^{-i\boldsymbol{k}\cdot\boldsymbol{r}}$ from the left, we obtain the Schrödinger equation for the periodic functions:

$$\underbrace{e^{-i\boldsymbol{k}\cdot\boldsymbol{r}} H e^{i\boldsymbol{k}\cdot\boldsymbol{r}}}_{H(\boldsymbol{k})} u_{n,\boldsymbol{k}}(\boldsymbol{r}) = E_{n,\boldsymbol{k}} u_{n,\boldsymbol{k}}(\boldsymbol{r})\,. \tag{2.18}$$

Therefore, we can thus identify the BZ as the parameter space of the transformed Hamiltonian $H(\boldsymbol{k})$ and $|u_{n,\boldsymbol{k}}(\boldsymbol{r})\rangle$ as the basis functions, sharing the same Hilbert space [3].

---

[3] Most often, it is convenient to work with the matrix elements of the Bloch Hamiltonian projected into some fixed basis of tight-binding orbitals. Hence, $|u_{n,\boldsymbol{k}}(\boldsymbol{r})\rangle$ denotes the column vector obtained by projecting $u_{n,\boldsymbol{k}}(\boldsymbol{r})$ into a fixed tight-binding basis.

Having a Hamiltonian with a parameter $\boldsymbol{k}$, the quantities from section 2.4.1 and 2.4.2 can be defined in the same way for the energy bands by

$$\gamma_n = \oint_C d\boldsymbol{k} \cdot \mathcal{A}_n(\boldsymbol{k}) \, , \tag{2.19}$$

$$\mathcal{A}_n(\boldsymbol{k}) = i\langle u_n(\boldsymbol{k}) | \nabla_{\boldsymbol{k}} u_n(\boldsymbol{k}) \rangle \, , \tag{2.20}$$

$$\Omega_{n,xy}(\boldsymbol{k}) = i \sum_{m \neq n} \frac{\langle u_n(\boldsymbol{k}) | \partial_{k_x} H(\boldsymbol{k}) | u_m(\boldsymbol{k}) \rangle \, \langle u_m(\boldsymbol{k}) | \partial_{k_y} H(\boldsymbol{k}) | u_n(\boldsymbol{k}) \rangle - (n \leftrightarrow m)}{\left(\varepsilon_n(\boldsymbol{k}) - \varepsilon_m(\boldsymbol{k})\right)^2} \, , \tag{2.21}$$

where the last expression (Berry curvature) is presented in two dimensions. This expression (2.21) has the flavor of second-order perturbation theory and clearly shows that the Berry curvature in the n^{th} band is the result of virtual transitions to other bands and that the inter-band coupling is related to the velocity operator $\partial_{k_j} H(\boldsymbol{k})$, $j = x, y$.

Remarkably, the Berry curvature indicates a key role in understanding solids, since it follows directly from the intrinsic property of the electronic band structure, without need for additional quantities. In the case of 2D BZ, the integral of the Berry curvature over the BZ is quantized:

$$C_n = \frac{1}{2\pi} \int_{BZ} d\boldsymbol{k} \, \Omega_{n,xy}(\boldsymbol{k}) \, . \tag{2.22}$$

The integer mentioned in the previous statement is known as the (first) *Chern number*, which is a characteristic of the non-trivial structure of the Berry curvature in a band. In a system that exhibits TRS, the Chern number is always zero due to the odd symmetry of the Berry curvature in momentum space. Therefore, breaking TRS is a necessary condition to have a band with a non-zero Chern number. One way to break TRS is by introducing an external magnetic field to the system. Additionally, it can also be accomplished by dividing the Hamiltonian into the eigenspace of the subsystem.

The Chern number can also be understood as an obstruction to having a well-defined Berry connection across the BZ. Indeed, if a well-defined Berry connection exists, then $C_n = 0$, while $C_n \neq 0$ means that there is no well-defined connection with one gauge. The total Chern number of a multiband system is a sum over all occupied states n, defined as

$$C = \sum_{n \in occ} C_n \, . \tag{2.23}$$

As we will see in Section 2.6.1, the Chern number is directly connected to the experimentally observed quantization of the Hall conductivity.

2.6 Topical examples

2.6.1 Integer quantum Hall effect

The first experiments exploring the quantum regime of the Hall effect were performed in 1980. K. von Klitzing measured the Hall resistivity ρ_{xy} on 2D electron gas (2DEG) [1]. He discovered that Hall resistivity ρ_{xy} sits on a plateau for a range of magnetic field, before jumping suddenly to the next plateau. The resistivity value on the plateau gives rise to

$$\rho_{xy} = -\frac{1}{\nu}\frac{h}{e^2} \quad (\text{quantum Hall formula}), \tag{2.24}$$

where ν is an integer. Today, measurements have confirmed that the value of ν is measured to be an integer to the high accuracy. This exact quantization in various materials points out that measuring ρ_{xy} in low temperature with strong magnetic field is a quantum mechanic phenomenon and violates classical interpretation [42]. The robustness of quantization, however, was not explained in the first experiment. Then, Laughlin figured out the connection of the quantized Hall conductivity based on a gauge theory [43]. Subsequently, Thouless, Kohmoto, Nightingale, and den Nijs (TKNN) [2], in parallel to Avron, Seiler, and Simon [44], linked the Hall conductivity to the total Chern number within occupied bands times the quantum of conductance e^2/h. Hence, this relation obtained by TKNN can be expressed by the following formula:

$$\sigma_{xy} = \frac{e^2}{h}\sum_{n\in\text{occ}} C_n\,, \tag{2.25}$$

where C_n denotes Chern number of each band defined in Eq. (2.22). With this efforts the Berry phase and Hall conductivity are well related and it confirms that this formulation only depends on the Bloch wavefunctions of the system. Thereby, the nonzero TKNN invariant would imply that the Berry connection is not well-defined (single-valued) and it directly connects the nontriviality to the emergence of the dissipationless current at the interface of a quantum Hall system. This edge modes appearing at the boundaries are actually topologically protected and their existence can be calculated with a non-zero Chern number in the bulk of 2D magnetic BZ.

2.6.2 Chern insulators

In last section it was shown how the TKNN invariant (or Chern number) can relate edge-state channels to quantized Hall conductance. Now, we shall see this connection in more general 2D insulators (e.g., Chern insulators). This unique feature can be inferred by bulk–boundary correspondence, guaranteeing the existence of zero-energy modes at their boundaries.

Using quantum anomalous Hall (QAH) systems, as a representative system for Chern insulators, the connection between Berry phase and quantized Hall conductivity will be discussed. The QAH systems were realized in different semiconductors such as Mn-doped HgTe quantum wells (QWs) [45], Mn-doped InAs/GaSb QWs [46] and chromium-doped $(\mathrm{Bi}, \mathrm{Sb})_2\mathrm{Te}_3$ thin films [47].

To illustrate the concepts of Chern insulators, it is helpful to employ a toy model proposed by Qi, Wu, and Zhang (QWZ) [48]. While the hexagonal lattice model introduced by Haldane [3] was historically the first model of a Chern insulator. We opt to utilize the QWZ model due to its simplicity. This model is sometimes called *half BHZ* [4] [3, 22, 49, 50].

QWZ Hamiltonian

The simple QWZ model Hamiltonian has only two bands in the bulk, providing a helpful realization of the charge QHE without an external magnetic field. The Hamiltonian H is defined in two dimension, constraining the fermions living on a 2D square lattice. The unit cell has one site which has two degrees of freedom (pseudo-spin or quasi-spin). Depending on the context, the degrees of freedom may describe the components of spin-1/2 electron or the orbitals. The former leads to spin-orbit coupling and the latter has an effect on hybridization of the bands. The QWZ Hamiltonian can be expressed as [22, 49, 50]

$$
\begin{aligned}
H = &\sum_{m_x=1}^{N_x-1} \sum_{m_y=1}^{N_y} \left(|m_x+1, m_y\rangle\langle m_x, m_y| \otimes \frac{-\sigma_z - i\sigma_x}{2} + h.c. \right) \\
&+ \sum_{m_x=1}^{N_x} \sum_{m_y=1}^{N_y-1} \left(|m_x, m_y+1\rangle\langle m_x, m_y| \otimes \frac{-\sigma_z - i\sigma_y}{2} + h.c. \right) \\
&\qquad\qquad +(2-u) \sum_{m_x=1}^{N_x} \sum_{m_y=1}^{N_y} |m_x, m_y\rangle\langle m_x, m_y| \otimes \sigma_z
\end{aligned}
\tag{2.26}
$$

---

[4] Bernevig-Hughes-Zhang (BHZ) is time-reversal topological insulator model describing the quantum spin Hall effect (QSHE) systems

where σ_i ($i = 1,2,3$) are the three Pauli matrices and u defines onsite potential. The nearest neighbour hoppings act on the internal degree of freedom, and it is different for x and y directions see [Eq. (2.26)]. The bulk momentum-space Hamiltonian can be obtained using Fourier transform as

$$H(\boldsymbol{k}) = \sin k_x \sigma_x + \sin k_y \sigma_y + (2 - u - \cos k_x - \cos k_y)\sigma_z \,. \tag{2.27}$$

The Hamiltonian is translationally invariant because k_x and k_y are good quantum numbers and can be expanded by the Pauli matrices

$$H(\boldsymbol{k}) = \underbrace{d_0(\boldsymbol{k})\sigma_0}_{E_0} + \boldsymbol{d}(\boldsymbol{k}) \cdot \boldsymbol{\sigma} \,, \tag{2.28}$$

where $d_0(\boldsymbol{k}) = \mathbb{1}_{2\times 2}$ and $\boldsymbol{d}(\boldsymbol{k})$ is a function mapping a 2D vector from the BZ into a 3D vector. Since the BZ is a torus, the endpoints of the vectors $\boldsymbol{d}(\boldsymbol{k})$ map out a deformed torus in $\mathbb{R}^3$ [22]. Hence, the $\boldsymbol{d}(\boldsymbol{k})$ vector can be expressed as

$$\boldsymbol{d}(\boldsymbol{k}) = \begin{pmatrix} \sin k_x \\ \sin k_y \\ 2 - u - \cos k_x - \cos k_y \end{pmatrix} . \tag{2.29}$$

Thus, the 2D bulk QWZ model has two bands and the energies are given by $E_\pm = E_0 \pm |\boldsymbol{d}(\boldsymbol{k})|$ [22]. The closure of the energy gap can be readily observed when any of the following conditions is met:

- $u = 0 \rightarrow \boldsymbol{k} = (0,0)$;
- $u = 2 \rightarrow \boldsymbol{k} = (0,\pm\pi)$, $(\pm\pi,0)$;
- $u = 4 \rightarrow \boldsymbol{k} = (\pm\pi,\pm\pi)$;

The energy dispersion near each point within above conditions has the shape of *Dirac cone* (linear dispersion). For example the Dirac point appears at Γ point as is shown in Fig. (2.4) (b), for the value of $u = 0$. Since the gap is zero for $u = 0$ (also in case of $u = 2$ and $u = 4$), we cannot investigate the topological properties for such systems. It is worth to recall that for calculating Chern number particularly for Hall conductivity discussed in previous section it is crucial to have a gap between valence and conduction bands. Therefore, for the values of $u \neq 0,2,4$ we can look for the topology of the Bloch states since the spectra are gapped.

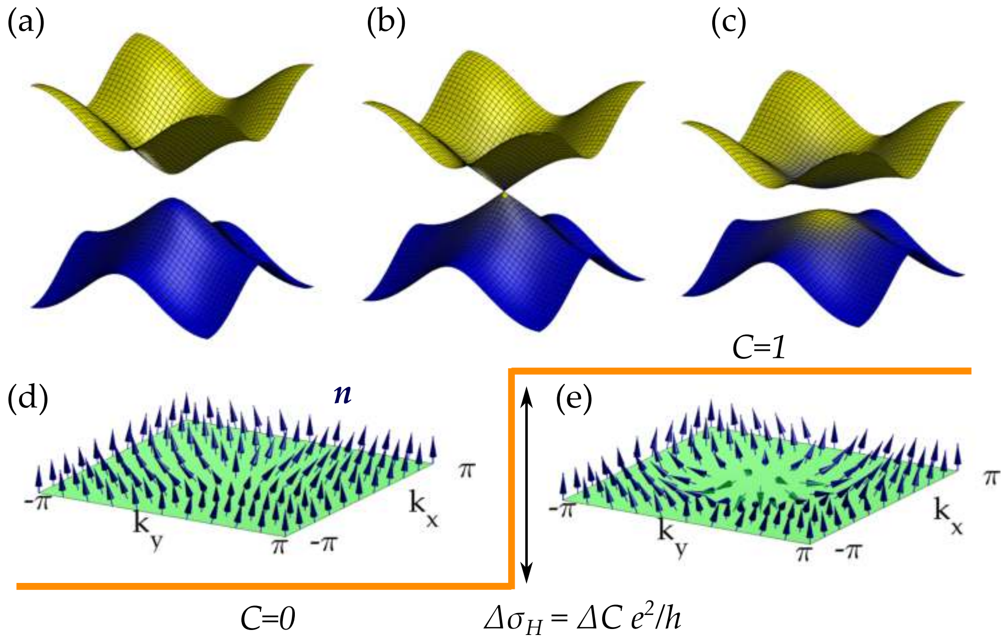

Figure 2.4: Energy spectra and the unit vector $\boldsymbol{n}$ as a function of $\boldsymbol{k}$. (a) and (d) correspond to the value $u = -0.5$ (trivial insulator: C=0). (c) and (e) are calculated for the value $u = 0.5$, corresponding to the Chern number $C = 1$ (topological). Panel (b) shows the spectrum for the phase transition point at $u = 0$. The flip of the arrows $\boldsymbol{n}$ (pseudo spin) at $\boldsymbol{k} = 0$ is consistent with the color exchange of valence and conduction bands.

The Hamiltonian described in Eq. (2.29) is reminiscent to the spin-1/2 in magnetic field where the vector $\boldsymbol{d}(\boldsymbol{k})$ acts as a magnetic field on the quasi-spin. We can define a unit vector

$$\boldsymbol{n}(\boldsymbol{k}) = \frac{\boldsymbol{d}(\boldsymbol{k})}{|\boldsymbol{d}(\boldsymbol{k})|}, \tag{2.30}$$

which maps a point on a torus T^2 to a two-dimensional sphere S^2 known as the Bloch sphere. Figure 2.4 represents how the unit vector $\boldsymbol{n}(\boldsymbol{k})$ behaves in comparison with their energy dispersions as $\boldsymbol{k}$ span over the BZ. The blue and yellow colors in Fig. 2.4 (a)-(c) denote the weight of pseudo-spin defined by valence and conduction band components, respectively. It can be seen that in Figs. 2.4 (c),(e) the composition of wave functions are exchanged near Γ point for the valence and conduction bands consistent with the unit vector $\boldsymbol{n}(\boldsymbol{k})$ behavior.

To illustrate the corresponding topological invariant for this two-level system, the resulting Berry curvature after Jacobian transformation in $\boldsymbol{k}$-space reads

$$\Omega^{\pm}_{xy} = \mp\frac{1}{2d^3}\boldsymbol{d}\cdot\left(\frac{\partial \boldsymbol{d}}{\partial k_x}\times\frac{\partial \boldsymbol{d}}{\partial k_y}\right) = \mp\frac{1}{2}\boldsymbol{n}\cdot\left(\frac{\partial \boldsymbol{n}}{\partial k_x}\times\frac{\partial \boldsymbol{n}}{\partial k_y}\right), \tag{2.31}$$

in which the Chern number for the occupied band (using Eq. (2.22)) can be written as:

$$C = \frac{1}{4\pi} \int_{BZ} \boldsymbol{n} \cdot \left(\frac{\partial \boldsymbol{n}}{\partial k_x} \times \frac{\partial \boldsymbol{n}}{\partial k_y}\right) d^2k \,. \tag{2.32}$$

From such analysis, it can be seen that $\boldsymbol{d}$ plays the role of magnetization which is dependent on the magnitude of u parameter. The Hall conductivity σ_H for the lower band can be then calculated as

$$\sigma_H = \frac{e^2}{h} C = \frac{e^2}{h} \frac{1}{4\pi} \int_{BZ} \boldsymbol{n} \cdot \left(\frac{\partial \boldsymbol{n}}{\partial k_x} \times \frac{\partial \boldsymbol{n}}{\partial k_y}\right) d^2k \tag{2.33}$$

where C is the number of times the $\boldsymbol{n}$-surface wraps over a unit sphere S^2 [5]. The integral in Eq. (2.32) gives the total solid angle subtended by $\boldsymbol{d}$-surface.

In particular, Figs. 2.5 and 2.6 are the examples of QWZ model corresponding to different topological phases. $\boldsymbol{d}$ vector as a function of $\boldsymbol{k}$ is visualized in the 3D $\boldsymbol{d}$ space. Each point of the unit vector $\boldsymbol{n}(\boldsymbol{k})$ on the closed torus T^2 is projected onto the Bloch sphere S^2 with a spinor parameterized by angles θ and ϕ. [6] In this regards, we simply count how many times the torus in the space of $\boldsymbol{d}$ captures the origin (topological charge as magnetic monopole). It is instructive to follow the gradual change of the surface of $\boldsymbol{d}$ with respect to the $\boldsymbol{k}$ point in the BZ. If the origin locates inside of the torus, the Chern number $|C| = 1$. Depending on which side of the torus surface (red or blue) contains the origin, the sign of the Chern number will change[7]. For the range of $0 < u < 2$ and $2 < u < 4$, we cannot define a single gauge $\mathcal{A}$ [Fig. 2.5 (f)]. Because of changing the sign of d_z due to sweeping $\boldsymbol{d}$ vector through the whole sphere, there must exist two gauges, $\mathcal{A}^N$ and $\mathcal{A}^S$ to avoid the singularity [50] (N and S denote "north" and "south" hemispheres, respectively). Therefore the topology is non-trivial and $C \neq 0$. In range of $u < 0$ the 3D vector $\boldsymbol{d}(\boldsymbol{k})$ only sweeps over the northern hemisphere when $\boldsymbol{k}$ scans over the BZ. We

---

[5] Chern number is sometimes called as wraping number

[6] The Chern number of Bloch band to expression for Chern number in the two-level system case can be related as [21]

$$C = \frac{1}{2\pi} \int_{BZ} \left(\frac{\sin\theta_k}{\partial k_x} \frac{\sin\phi_k}{\partial k_y} - \frac{\sin\phi_k}{\partial k_x} \frac{\sin\theta_k}{\partial k_y}\right) dk = \frac{1}{2\pi} \int_{BZ'} d\theta d\phi \frac{\sin\theta}{2} \tag{2.34}$$

where BZ' is the image of the BZ on the Bloch sphere, or equivalently the central projection of the closed between manifold $\mathcal{M}$ onto the unit sphere. The $\boldsymbol{k}$-dependent quantities θ_k and ϕ_k are the spherical coordinate angles of the unit vector:

$$\boldsymbol{n} = \frac{\boldsymbol{d}(\boldsymbol{k})}{|\boldsymbol{d}(\boldsymbol{k})|} = \begin{pmatrix} \cos\phi_k \sin\theta_k \\ \sin\phi_k \sin\theta_k \\ \cos\theta_k \end{pmatrix} \tag{2.35}$$

[7] If the red (blue) color surface of torus captures the origin, the corresponding Chern number would be $+1(-1)$.

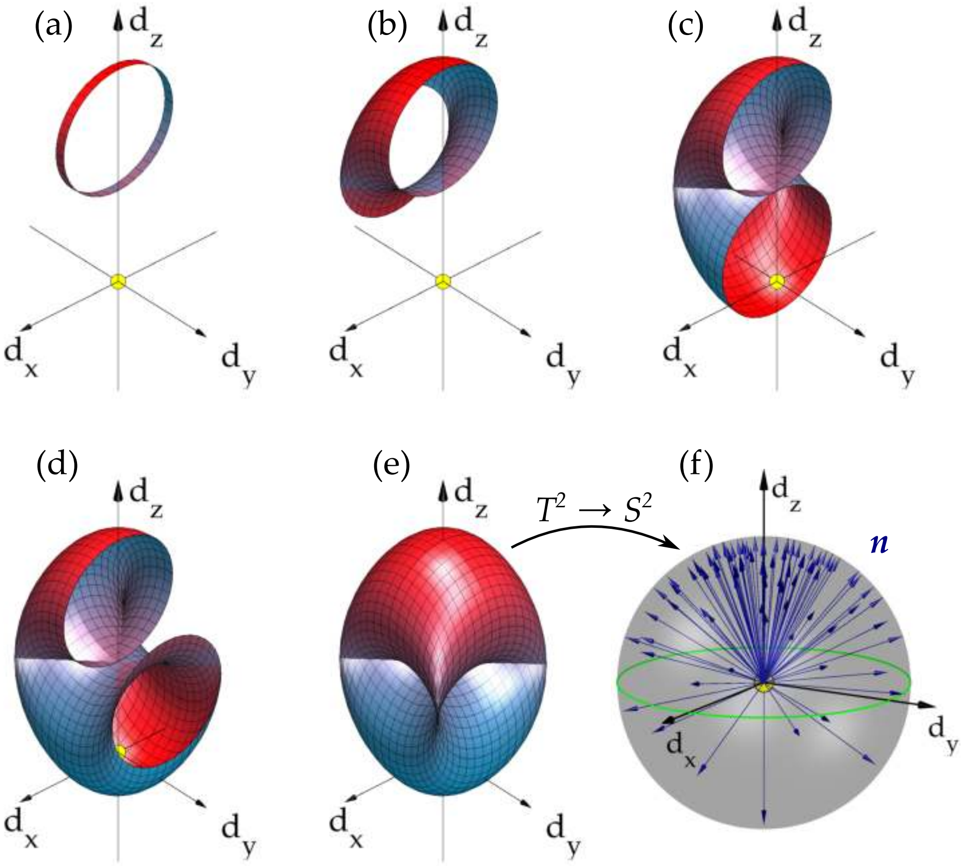

Figure 2.5: The gradual evolution of the vector $\boldsymbol{d}(\boldsymbol{k})$ for the QWZ model with the parameter value $u = 0.5$ $(C = 1)$ as vector $\boldsymbol{k}$ span the BZ. The $\boldsymbol{d}$ snapshots are displayed in (a) $k_y = -\pi$; in (b) $k_y = -\pi, \ldots, -\pi/2$; in (c) $k_y = -\pi, \ldots, 0$; in (d) $k_y = -\pi, \ldots, \pi/2$ and in (e) $k_y = -\pi, \ldots, \pi$ (closed surface). In panel (f), each point of the unit vector $\boldsymbol{n}(\boldsymbol{k})$ on the closed torus T^2 is projected onto the sphere S^2. [The figures in panels (a)-(e) show the results of calculations effectively similar to the model used in Ref. [22]].

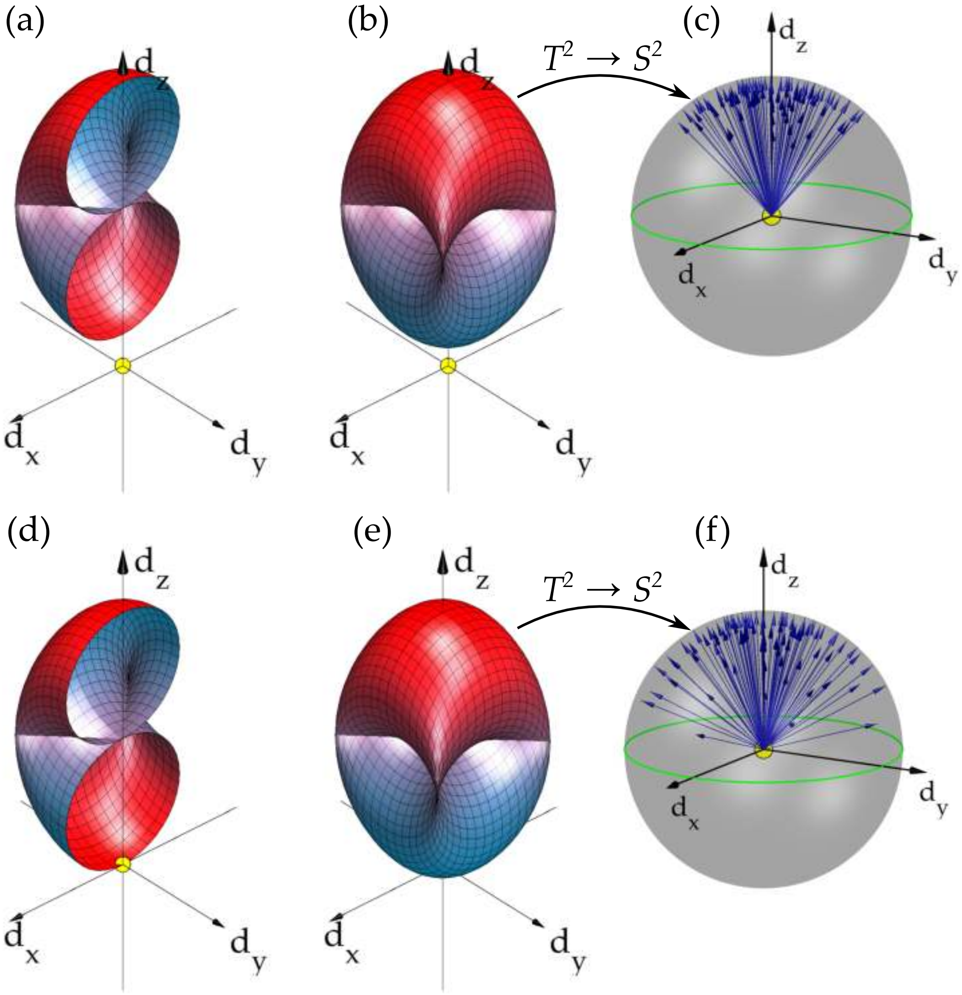

Figure 2.6: The torus $\boldsymbol{d}(\boldsymbol{k})$ images corresponding to the values $u = -0.5$ [panels (a),(b)] and $u = 0$ [panels (d),(e)]. The half torus surfaces are depicted on (a) and (d) whereas (b) and (c) represent the full images of the torus. The corresponding projection unit vector $\boldsymbol{n}$ on the sphere is shown in (c) and (f). If the origin resides on the outside (inside) of the torus the Chern number $C = 0$ $(C = 1)$. If the surface touches the origin the corresponding Chern number is not well-defined. [The figures in panels (a)-(e) show the results of calculations effectively similar to the model used in Ref. [22]].

need only one gauge $\mathcal{A}^N(\boldsymbol{k})$ for the whole BZ. Therefore, the topology is expected to be trivial and the the Chern number $C = 0$. In the range of $u > 4$ the situation is very similar to $u < 0$, but $\boldsymbol{d}$ sweeps over the southern hemisphere only. The topology is again trivial and $C = 0$ [50].

Edge state in QWZ model

TIs exhibit an intriguing property in the form of zero-energy modes localized at their boundaries. In 1D systems, these bound states are confined to the ends of the system, while in 2D topological materials, the edge states manifest as one-dimensional propagating modes along the edges. Remarkably, these edge states are robust against perturbations and can only be eliminated if the energy gap of the bulk bands closes. The underlying reason for this behavior lies in the concept of bulk-boundary correspondence, where the existence of boundary states is a consequence of the non-trivial topology of electronic states in the bulk [22]. A heuristic explanation for this phenomenon is that when transitioning between two materials, the spatially-dependent energy gap must close near the interface for the topology to change. Without this gap closure, the topology remains unchanged [50].

Let us consider a strip of a clean 2D insulator defined in QWZ model with a Chern number C. The strip extends infinitely along the x direction, while along the y direction it consists of N_y sites and is terminated by open boundary condition. Translation invariance is preserved along the x direction, allowing us to perform a partial Fourier transform solely along that direction. After the Fourier transformation, the original Hamiltonian has the form of a 1D lattice Hamiltonians with a continuous parameter k_x, which is the wavenumber along x. For a concrete example, the k_x-dependent Hamiltonian reads

$$\begin{aligned} H(k_x) = &\sum_{m_y=1}^{N_y-1} \left(|m_y+1\rangle\langle m_y| \otimes \frac{-\sigma_z - i\sigma_y}{2} + h.c. \right) \\ &+ \sum_{m_y=1}^{N_y} |m_y\rangle\langle m_y| \otimes \Big(\sin k_x \sigma_x + (2-u)\sigma_z - \cos k_x \sigma_z \Big) \end{aligned} \tag{2.36}$$

The semi-infinite energy spectra for two different values of $u = -0.5$ and $u = 0.5$ are calculated along y direction and shown in Fig. 2.7 (a),(b). All states along x are delocalized because of periodic boundary conditions. However, along y direction, states are exponentially confined to the edge termination. The energy eigenstates within the bulk gap must be edge modes and can be assigned to edge boundary. The edge mode, however, is one-way propagating (i.e., chiral) and its slope can be indicated by the group velocity $\frac{dE}{dk_x}$.

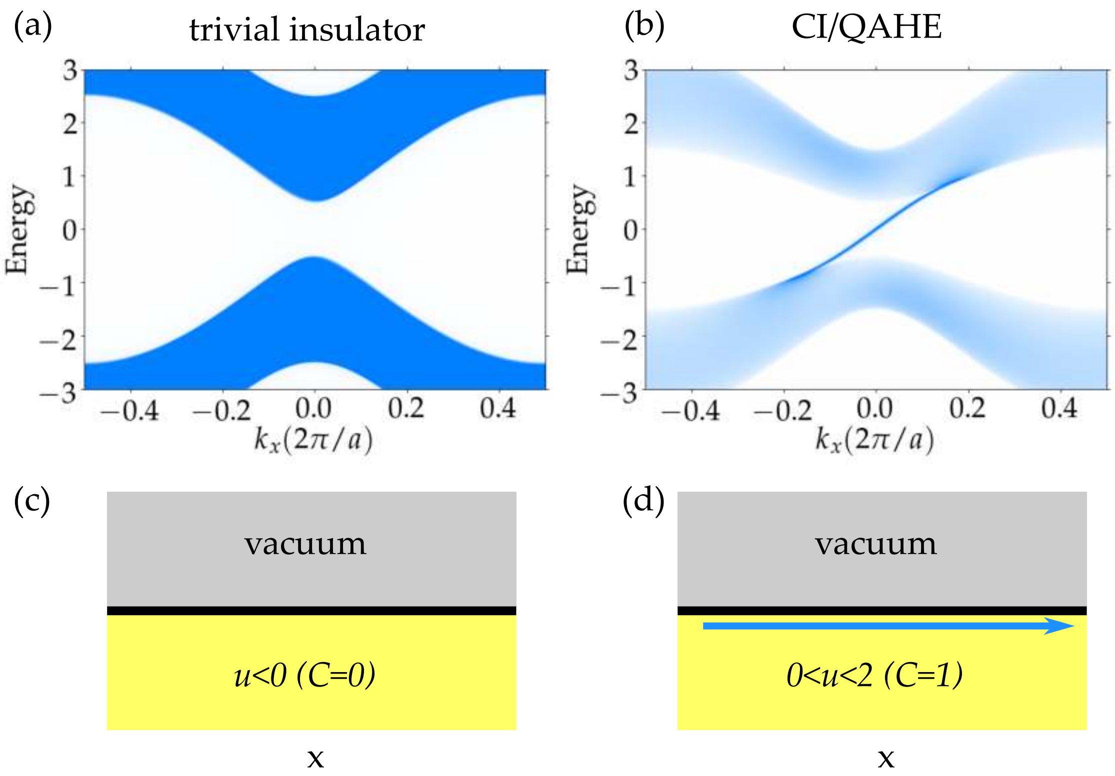

Figure 2.7: The calculated spectral functions for a semi-infinite 2D sample in QWZ model for values (a) $u = -0.5$ (trivial) and (b) $u = 0.5$ (topological). (c) and (d) a schematic figures with their corresponding Chern number and chiral edge mode.

2.6.3 2D time-reversal invariant topological insulators

2.6.3.1 Quantum spin Hall effect

As discussed in the preceding section, in QWZ model (QAH system), there exist robust dissipationless edge state propagating unidirectionally (i.e., chiral) along the boundary without applying magnetic field. The quantized Hall conductance σ_{xy} and nonzero Chern number C arises due to the Berry flux present in each plaquette within the square lattice. As suggested by Haldane [3] in the absence of the external magnetic field the time-reversal symmetry (TRS) can also be broken in QAH system. It is worth noting that the TRS breaking is an essential ingredient for realizing a topological phase and subsequently nonzero Hall conductance. This behavior can be stem by calculating the Berry curvature in the 2D BZ and simply understood by following condition:

$$\Theta\Omega(\boldsymbol{k})\Theta^{-1} = -\Omega(-\boldsymbol{k}) \tag{2.37}$$

which shows the Berry curvature is an odd function with respect to the TRS operator Θ. This anti-unitary operator Θ can be defined generally as $\Theta = \tau\mathcal{K}$ where τ represents the unitary part and $\mathcal{K}$ denotes complex conjugation. Since the Ω is an odd function, the system can reveal non-trivial topology only if the TRS is broken. However, the family of quantum Hall systems can be expanded to include a new class of phases in which the low-energy modes are protected by TRS. These systems, referred to as *quantum spin Hall* (QSH) systems.

The quantum spin Hall effect (QSHE) is a fascinating phenomenon in condensed matter physics, exhibits spin-polarized counter-propagating (*helical*) edge states that are topologically protected against backscattering. The QSHE, also known as the 2D TI, was initially proposed to exist in graphene in the presence of spin-orbit coupling (SOC) [51, 52]. Shortly after, the study of 2D semiconductor systems with uniform strain further advanced the understanding of this effect [53]. It was subsequently predicted to exist [54] and observed in mercury telluride (HgTe/CdTe) quantum wells [55, 56] which has stronger SOC. The discovery of the QSHE has stimulated extensive research on TIs, leading to the identification of many new materials and the exploration of their unique electronic and optical properties. The robustness of QSH systems is attributed to the TRS of type $\Theta^2 = -1$, which prohibits backscattering between states in Kramers pairs. This is due to the fact that two states within a helical pair are time-reversal conjugates of one another. TRS maps one spin momentum locked edge state $|\psi(\boldsymbol{k}), \uparrow\rangle$ to its Kramers' partner $|\psi(-\boldsymbol{k}), \downarrow\rangle$, and they are robust to any TRS preserving perturbation [57].

2.6.3.2 Time-reversal symmetry

There are two types of time-reversal symmetry, and only one type can exist within a system. It can either be characterized by $\Theta^2 = +1$ (symmetric) or $\Theta^2 = -1$ (anti-symmetric), but not both simultaneously. The former Θ can be defined just by complex conjugation $\mathcal{K}$ whereas the latter for half-spin particle. The generic example of TRS operation under condition of $\Theta^2 = -1$ would be defined by $\Theta = -i\sigma_y\mathcal{K}$ on the basis of the eigenstates of σ_z. [8] Using Bloch bulk Hamiltonian in k-space and the operation of Θ, the requisite condition for time-reversal symmetric system can be given as

$$\tau H(-\boldsymbol{k})^* \tau^\dagger = H(\boldsymbol{k})\,. \tag{2.38}$$

At the time-reversal invariant momenta (TRIM), this condition becomes

$$\tau H(\boldsymbol{k}_{\mathrm{TRIM}})^* \tau^\dagger = H(\boldsymbol{k}_{\mathrm{TRIM}})\,, \tag{2.39}$$

where it results in Kramers degeneracy, which satisfies $\Theta^2 = -1$ [22]. A notable outcome is that for every eigenstate $|u(\boldsymbol{k})\rangle$ of Hamiltonian $H(\boldsymbol{k})$, there exists a time-reversed partner eigenstate $\tau^T|u(\boldsymbol{k})\rangle^*$ of the Hamiltonian $H(-\boldsymbol{k})$ with the same energy.

The aforementioned properties are particularly crucial for our study presented in Chapter 5, where we investigate a spin-$\frac{1}{2}$ system in the presence of TRS. Therefore, it is informative to begin by examining the simple four-band Bernevig-Hughes-Zhang (BHZ) model as a representative example of time-reversal-invariant insulators.

2.6.3.3 Bernevig-Hughes-Zhang model

BHZ model, is a simple model which advances our understanding to the electronic properties of 2D TIs [54]. This model was proposed originally for investigating of the QSHE in HgTe quantum wells [55]. The BHZ model is based on a simple lattice model of a 2D semiconductor, where the electrons are confined to move in a plane. BHZ considered four band model with the following basis in each atom

$$|s\uparrow\rangle, |s\downarrow\rangle, |p_x + ip_y \uparrow\rangle, |p_x - ip_y \uparrow\rangle\,, \tag{2.40}$$

where s, p are atomic orbitals. The model takes into account the effects of SOC and band inversion, which are two key features that characterize the topological properties of the

---

[8] This can be checked by $\Theta\sigma_j\Theta^{-1} = -\sigma_j$ for $j = x, y, z$.

system. The resulting band structure of the BHZ model exhibits a band gap with non-trivial topological properties, which gives rise to the presence of robust edge states in the system which will be discussed later.

However, in this section we start with more generic four band toy model with inclusion of SOC, preserving all the properties in the original paper. Our starting point is to extend two copies of Chern insulator model see [Eq. (2.27)] with opposite chiralities to the new 2D TI model with four states per unit cell. These states are a combination of two orbital states and two spin states. With this more general basis, the Bloch bulk Hamiltonian in the momentum space is given by [22] [9]

$$H_{\mathrm{BHZ}}(\boldsymbol{k}) = s_0 \otimes \left[(2 - u - \cos k_x - \cos k_y)\sigma_z + \sin k_y \sigma_y\right] + s_z \otimes \sin k_x \sigma_x + s_x \otimes \mathcal{C} \quad (2.41)$$

where $s_i, (i = 1,2,3)$ and $\sigma_j, (j = x,y,z)$ are Pauli matrices acting on external (orbital) and internal (spin) degrees of freedom. The operator $\mathcal{C}$ is a Hermitian coupling matrix acting on the internal degree of freedom. Here u as in the previous QWZ model has the interpretation of an on-site potential. In case of $\mathcal{C} = 0$, the Hamiltonian H_{BHZ} reduces to the 4-band toy model for HgTe, introduced by BHZ [54]. Two different systems can be described by the model proposed in Eq. (2.41). However, from now on, we will focus on the system that satisfies $\Theta^2 = -1$ for spin-$\frac{1}{2}$ systems.

In particular, the Fig. 2.8 exhibits the band structure of the BHZ model for the anti-symmetric TR operator $\Theta^2 = -1$. The selected coupling operator is $\mathcal{C} = 0.3\sigma_y$, while the on-site potentials have been assigned values of $u = -0.8$ [Fig. 2.8(a)] and $u = 0.8$ [Fig. 2.8(b)] for the trivial gap and inverted gap, respectively. The blue-to-yellow color coding in the figure indicates the contributions of each orbital to the wave functions.

To distinguish two phases shown in Fig. 2.8, in the following section, the corresponding topological classification for 2D TR-invariant insulators will be demonstrated. Furthermore, the extension of these concepts to 3D TIs will also be discussed.

2.6.3.4 $\mathbb{Z}_2$ invariant

During the past few years, a multitude of mathematical expressions of the $\mathbb{Z}_2$ topological invariant ν have been devised [52, 58–63]. The invariant ν is assigned to be either 0 or 1. If $\nu = 0$, it means the system is topologically trivial and it is non-trivial when $\nu = 1$. Originally, the first formulation was given by Kane and Mele for the 2D TIs of

---

[9] The model presented in Eq. (2.41) is slightly different to the one addressed in Ref. [22], however, it captures the same features.

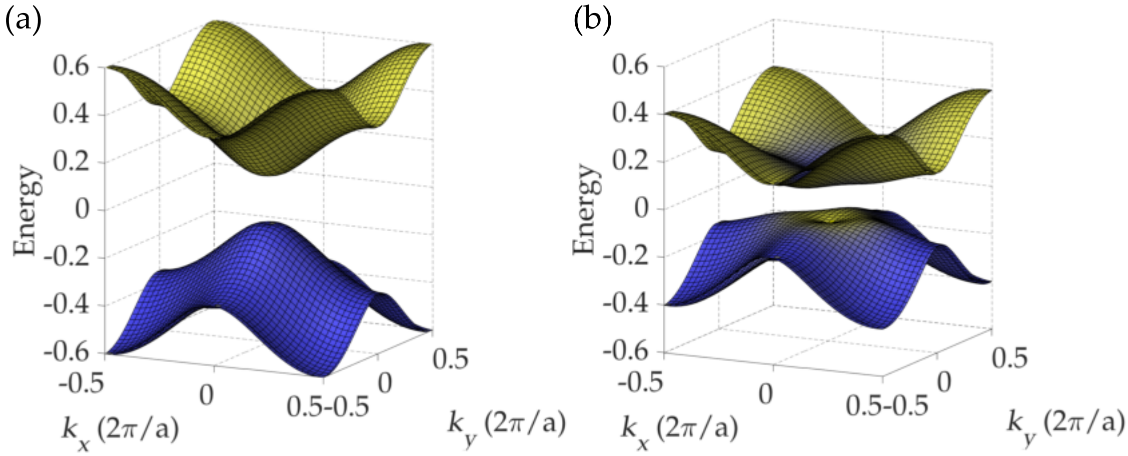

Figure 2.8: Bulk electronic band structures of BHZ model, with (a) $u = -0.8$ (trivial gap) and (b) $u = 0.8$ (inverted gap). The valence and conduction components to the wavefunctions are indicated with blue and yellow, respectively.

the QSHE type [52]. Next, Fu and Kane developed it in reference to the occupied Bloch states [58]. They introduced the concept of time-reversal polarization, which is connected to the Berry phase of every occupied state. This technique is relevant to any Bloch insulator that preserves time-reversal symmetry.

In this section, to understand how one can define such $\mathbb{Z}_2$ invariant we will briefly review the concept of time-reversal polarization established by Fu, Kane [58, 59] for both 2D and 3D cases.

Fu-Kane method:

Kramers' theorem, which applies to spinful fermions in the presence of TRS, guarantees an even number ($2N$) of bands, where N is the number of non-Kramers pair eigenstates. Time reversal transforms eigenstates at $\boldsymbol{k}$ of bands "I" into eigenstates at $-\boldsymbol{k}$ of bands "II", and vice versa, but only up to a phase factor [49, 58]

$$|u^{I}_{-\boldsymbol{k},\alpha}\rangle = -\exp(i\chi_{\boldsymbol{k},\alpha})\Theta|u^{II}_{\boldsymbol{k},\alpha}\rangle\,, \tag{2.42}$$

$$|u^{II}_{-\boldsymbol{k},\alpha}\rangle = \exp(i\chi_{-\boldsymbol{k},\alpha})\Theta|u^{I}_{\boldsymbol{k},\alpha}\rangle\,, \tag{2.43}$$

where α runs from 1 to N, χ is a smooth function and I, II denote the two sets of eigenstate connected by Kramers' theorem. With this, the partial polarization corresponding to one of the sets $s = I$ or II can be written as

$$P^{s} = \frac{1}{2\pi}\int_{-\pi}^{\pi} d\boldsymbol{k}\mathcal{A}(\boldsymbol{k})\,, \tag{2.44}$$

where the quantity

$$\mathcal{A}^s(\boldsymbol{k}) = i\sum_{\alpha}\langle u^s_{\boldsymbol{k},\alpha}|\nabla_{\boldsymbol{k}}|u^s_{\boldsymbol{k},\alpha}\rangle \tag{2.45}$$

is Berry connection. The partial polarization given by Eq. (2.44) for each set s is not gauge invariant and varies by an integer multiple of lattice constants under a general $U(2N)$ gauge transformation. Nonetheless, the difference in partial polarization between two sets defines a physical quantity, known as time-reversal polarization, only relevant in the presence of TRS

$$P_\theta = P^I - P^{II}\,. \tag{2.46}$$

The above quantity P_θ is defined modulo an integer. If we skip some of the algebraic steps mentioned in [58], Fu-Kane obtained the following relation

$$(-1)^{P_\theta} = \frac{\sqrt{\det[w(0)]}}{\mathrm{Pf}[w(0)]}\,\frac{\sqrt{\det[w(\pi)]}}{\mathrm{Pf}[w(\pi)]}\,. \tag{2.47}$$

where Pf$[w]$ is called Pfaffian. Pfaffian of an anti-symmetric matrix w has the property $\det[w] = \mathrm{Pf}[w]^2$. w is a $U(2N)$ matrix and is called sewing matrix, which in presence of TRS reads

$$w_{\alpha,\beta}(\boldsymbol{k}) = \langle u_{-\boldsymbol{k},\alpha}|\Theta|u_{\boldsymbol{k},\beta}\rangle\,. \tag{2.48}$$

Proceeding further, Fu-Kane defined the $\mathbb{Z}_2$ invariant ν as

$$(-1)^{\nu} = \prod_{i=1}^{4}\frac{\sqrt{\det[w(\Gamma_i)]}}{\mathrm{Pf}[w(\Gamma_i)]}\,. \tag{2.49}$$

Γ_i denotes TRIM in the 2D BZ sketched in Fig. 2.9. In particular, the value $\nu = 1$ describe a system with QSHI phase.

In addition, Fu and Kane demonstrated that the computation of $\mathbb{Z}_2$ invariants is simplified when the system features *inversion symmetry* [59]. They showed that the parity of occupied Bloch wave functions at TRIMs in the BZ can be used to determine the invariants. The correponding index in 2D reads

$$(-1)^{\nu} = \prod_{i=1}^{4}\delta_i\,, \qquad \delta_i = \prod_{m=1}^{N}\xi_{2m}(\Gamma_i)\,, \tag{2.50}$$

where $\xi_{2m}(\Gamma_i) = \pm 1$ is the parity eigenvalue of the $2m^{\text{th}}$ occupied energy band at Γ_i which exhibits the same eigenvalue $\xi_{2m} = \xi_{2m-1}$ as its Kramers-degenerate counterpart.

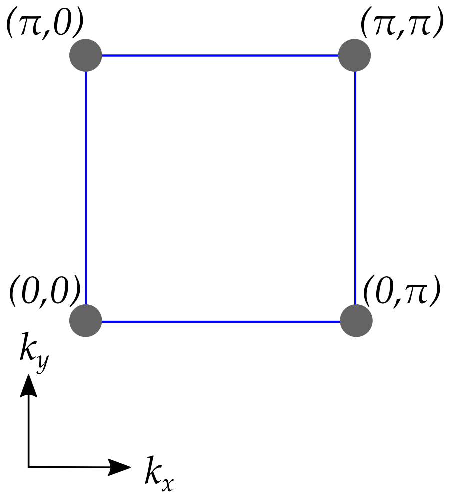

Figure 2.9: Time-reversal invariant momenta in two-dimensional BZ for a square lattice.

$\mathbb{Z}_2$ invariant as an obstruction

As it was mentioned earlier, a nonzero value of the Chern number is an obstruction to finding a smooth gauge for the Bloch wavefunctions to the whole BZ. Hence, a nonzero Chern number signifies an obstruction to the application of Stokes theorem over the whole BZ. If a smooth gauge could be defined, then Stokes' theorem would be valid and one can calculate the Chern number with the integral of the Berry potential over the full BZ boundary. However, this integral would evaluate to zero because the BZ has torus shape and does not have a boundary. Thus, the nonzero Chern number can be expressed as an obstruction to Stokes' theorem [49, 58].

As it was explained in details by Fu and Kane in Ref. [58], just as the Chern number in a Chern insulator can also be defined as an obstruction to Stokes' theorem over the whole BZ, the $\mathbb{Z}_2$ invariant in a TI is defined as an obstruction to Stokes' theorem over *half* of the BZ

$$\nu = \frac{1}{2\pi}\left[\oint_{\partial\,\text{half BZ}} d\boldsymbol{k}\cdot\boldsymbol{A}(\boldsymbol{k}) - \int_{\text{half BZ}} d^2k\,\Omega(\boldsymbol{k})\right] (\text{mod}\,2)\,. \tag{2.51}$$

The two integrals in the equation above are equal to each other only when it is possible to find a smooth gauge in half of the BZ. Therefore, the nontrivial insulator $\mathbb{Z}_2$ index ($\nu = 1$) must be an obstruction to this possibility. If $\nu = 0$, it is obvious that there is really no obstruction to Stokes' theorem and the insulator is thus trivial.

Following Fu-Kane approach [58], based on lattice gauge theories, Fukui and Hatsugai implemented the $\mathbb{Z}_2$ invariant formula for the purpose of discretized BZ in numerical calculations [60]. In practical numerical calculations, diagonalizing Hamiltonians is typically done at a discrete set of points selected appropriately in the BZ. We have restricted data on the wave functions, provided only at such discrete points. A phase ambiguity in the wave function results in a gauge ambiguity for the Berry connection. However, from above definition, $\mathbb{Z}_2$ invariant can be computed using wave functions in any gauge. Within each patch in the lattice BZ, one can define a gauge such that the gauge potential is a smooth and well defined function. The local field or curvature in the unit patch leads to a zero value. The nonzero integer values are only allowed in the boundary between two patches. The sum of these integer values contributes to the determination of the $\mathbb{Z}_2$ invariant. This procedure is particularly useful and has been employed in our study, as outlined in Chapter 5. When the system exhibits inversion symmetry (parity), we rely on the Fu-Kane formula to determine the parity of the occupied bands. However, in the absence of inversion symmetry, we resort to using the Fukui and Hatsugai formula. It should be noted that this approach was also utilized in the calculation of the Chern number, as proposed by Fukui [64].

2.6.3.5 Edge states in BHZ model

In Section 2.6.3.4, we discussed practical methods for calculating topological invariants in 2D time-reversal symmetric systems. In this section, the semi-infinite edge spectra will be presented for various cases using iterative Green's function scheme [65].

We consider a semi-infinite square lattice with edge parallel to x-axis. Unlike k_y, k_x is translationally invariant, thus, the Bloch Hamiltonian for k_x can be written as

$$\begin{aligned} H_{\mathrm{BHZ}}(k_x) = & \sum_{m_y=1}^{N_y-1} \left(|m_y+1\rangle\langle m_y| \otimes s_0 \otimes [\frac{-\sigma_z - i\sigma_y}{2}] + h.c. \right) \\ & + \sum_{m_y=1}^{N_y} |m_y\rangle\langle m_y| \otimes \left(s_z \otimes \sin k_x \sigma_x + s_0 \otimes (2-u-\cos k_x)\sigma_z + s_x \otimes \mathcal{C} \right). \end{aligned} \tag{2.52}$$

The edge spectral functions are computed for a fixed coupling $\mathcal{C}$ and two types of parameters u. The coupling is set to $\mathcal{C} = 0.3\sigma_y$ for the parameters $u = -0.8$ and $u = 0.8$, both of which satisfy the condition $\Theta^2 = -1$. Both cases break inversion symmetry, rendering the parity method for calculating the $\mathbb{Z}_2$ invariant invalid. Therefore, we employ the Fukui method to obtain the $\mathbb{Z}_2$ invariant. The calculated index yields $\nu = 0$ for $u = -0.8$, indicating the absence of gapless edge states at the boundary, as depicted by the edge density of states calculations along k_x [see Fig.2.10(a)]. In the case of $u = 0.8$, the calculated $\mathbb{Z}_2$ invariant evaluates to $\nu = 1$. The edge spectral function along k_x is also computed and shown in Fig.2.10(b). The crossings at $k_x = 0$ are protected by TRS as long as the coupling is not strong enough to close the bulk gap. The spin-up and spin-down densities presented in Fig.2.10(a) correspond to the counter-propagating edge modes, showing the emergence of QSH phase. The schematic view of spin-polarized edge modes is illustrated in Fig.2.10(d).

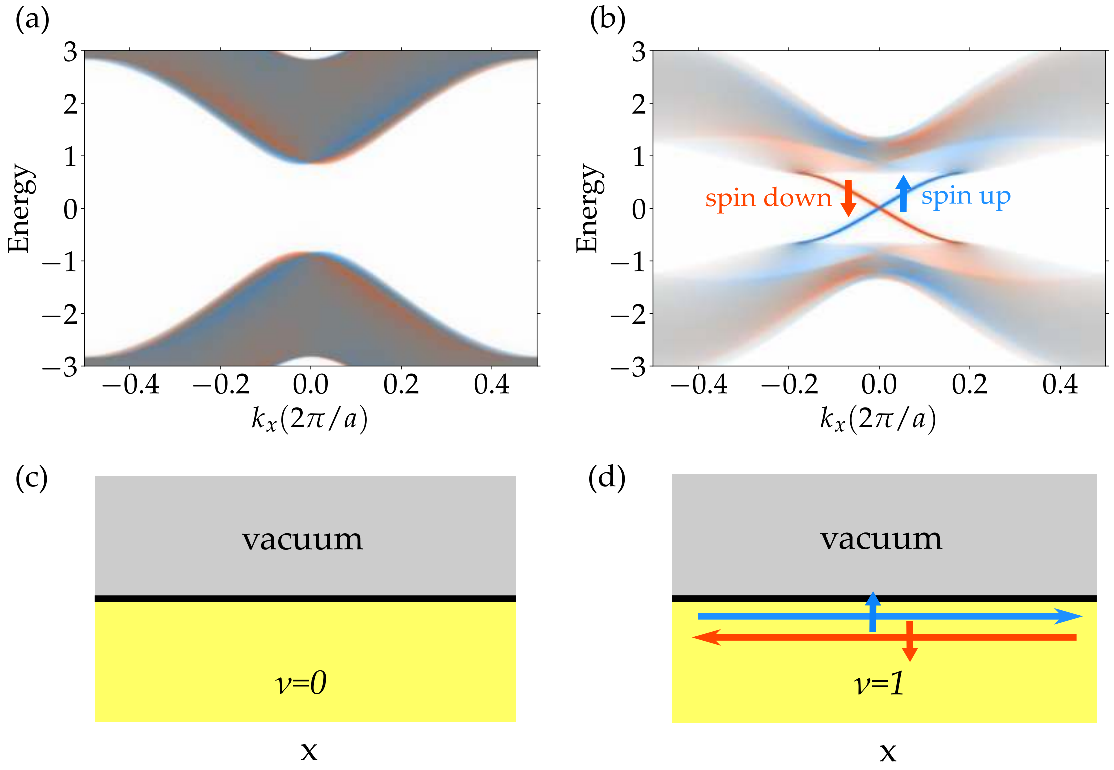

Figure 2.10: The edge spectral function in the BHZ model is shown for two different parameters: (a) $u = -0.8$ corresponding to $\nu = 0$, and (b) $u = 0.8$ corresponding to $\nu = 1$. The coupling is fixed at $\mathcal{C} = 0.3\sigma_y$ for both cases. The spin-resolved edge modes along x are indicated by blue (up) and red (down).

2.6.4 3D time-reversal invariant topological insulators

Advancing in the discovery of 2D TI materials, the pioneering theoretical topological characterization soon extended to the three dimensional systems [66–68]. Since than , a series of materials have been discovered to be TIs. In 3D, similar to 2D-QSHIs, the existence of the TRS is essential. In 2007, the first proposed 3D TI material, e.g., $Bi_{1-x}Sb_x$ was predicted [59] and soon after it was experimentally observed by angle-resolved photoemission spectroscopy (ARPES) in 2008 [4]. Later, a new family of stoichiometric crystals, Bi_2Se_3, Bi_2Te_3, and Sb_2Te_3, was identified as three-dimensional topological insulators [5, 6].

The generalization of QSHI to three dimensions results in the emergence of strong and weak topological phases. In 3D, a total of four $\mathbb{Z}_2$ indices $(\nu_0;\nu_1,\nu_2,\nu_3)$ are used to categorize the topological phases [66]. Nonzero values of ν_0 indicate a strong topological insulator (STI), while nonzero values of ν_1,ν_2,ν_3 represent a weak topological insulator (WTI).

In 3D we have eight TRIM points which can be denoted by the reciprocal lattice vectors $\boldsymbol{b}_i$,

$$\Gamma_{i=(n_1,n_2,n_3)} = \frac{1}{2}(n_1\boldsymbol{b}_1 + n_2\boldsymbol{b}_2 + n_3\boldsymbol{b}_3) \tag{2.53}$$

with $n_j = 0,1$.

Here $\mathbb{Z}_2$ index is defined separately for each of the 2D surfaces of the 3D BZ. Thus, we require four TRIM points to write down the $\mathbb{Z}_2$ index ν as

$$(-1)^{\nu} = \prod_{i=1}^{4}\delta_i\,, \qquad \delta_i = \frac{\sqrt{\det[w(\Gamma_i)]}}{\mathrm{Pf}[w(\Gamma_i)]}\,. \tag{2.54}$$

Now, with this Fu-Kane-Mele [66] strong and weak topological invariants read

$$(-1)^{\nu_0} = \prod_{n_j=0,1}\delta_{n_1,n_2,n_3} \tag{2.55}$$

$$(-1)^{\nu_{i=1,2,3}} = \prod_{n_i=1,n_{j\neq i}=0,1}\delta_{n_1,n_2,n_3} \tag{2.56}$$

where there could only be four independent $\mathbb{Z}_2$ invariants. Note that, δ_{n_1,n_2,n_3} is a topological number quantized to -1 or 1.

In the case of strong $\mathbb{Z}_2$ index being nontrivial ($\nu_0 = 1$), one expects to see odd number of gapless counterpropagating surface states which connect the valence and conduction bands. They are topologically protected against impurities and defects and occurrence of these states is independent of the choice of the surface termination. On the other hand, if the strong invariant equals to $\nu_0 = 0$, but the weak indices are nonzero ($\nu_i \neq 0$), one can expect to see odd pairs of gapless states in the bulk gap. These WTI states have protected states only on specific surfaces and not robust against perturbation.

In addition, in the presence of *inversion symmetry* in 3D systems, the Fu and Kane formula [59] for the computation of $\mathbb{Z}_2$ invariants leads to the four independent $\mathbb{Z}_2$ indices, which are read as: (see Fig. 2.11)

$$(-1)^{\nu} = \prod_{i=1}^{8} \delta_i \,, \qquad \delta_i = \prod_{m=1}^{N} \xi_{2m}(\Gamma_i) \,, \tag{2.57}$$

$$(-1)^{\nu_k} = \prod_{n_k=1; n_{j\neq k}=0,1} \delta_{i=(n_1 n_2 n_3)} \,, \qquad \delta_i = \prod_{m=1}^{N} \xi_{2m}(\Gamma_i) \,. \tag{2.58}$$

where $\xi_{2m}(\Gamma_i) = \pm 1$ is the parity eigenvalue of the $2m^{\text{th}}$ occupied energy band at Γ_i.

The topological classification is generically defined by the above four $\mathbb{Z}_2$ indices $(\nu_0; \nu_1, \nu_2, \nu_3)$. They can be most easily understood by appealing to the bulk boundary correspondence. Moreover, it is generally not possible to decompose the Hamiltonian into eigenstates of the TR operator in TRS systems. However, in the specific scenario of well-defined spin subspaces (SOC=0), such decomposition becomes possible. Hence, in each subspace, the Chern number can be calculated. It is worth noting that the total Chern number is always zero in TRS system, while the difference of two subspaces, $(C_I - C_{II})/2$, can be nonzero and leads to $\mathbb{Z}_2$ invariant. This quantity is called *spin Chern number* [69].

In the 2D BZ of the surface of 3D TIs, there are four TR invariant points where gapless surface states, if present, must be Kramers degenerate and form Dirac point at the Kramers points (see Fig. 2.11). The spin-orbit interaction breaks the degeneracy outside of these points. At low energy, the expectation values of the in-plane spin components exhibit a chiral spin texture. This means that at each k point on the constant energy cut of the cone, the spin has direction determined by k, resulting in a phenomenon known as spin-momentum locking [70]. TR-invariant-single-particle perturbations cannot introduce a gap for the surface states. The gap can be open when a TR breaking perturbation is introduced on the surface. The system becomes fully insulating, both in the bulk and on the surface.

In a STI, on each surface of crystal, there exist robust conducting surface states protected by nontrivial bulk topological invariant. They are robust against disorder and impurities as long as TRS is preserved. However, WTI exhibits protected conducting states on specific surfaces characterized by weak $\mathbb{Z}_2$ indices. These states are robust against disorder and local perturbations, as long as the protecting symmetries remain intact. However, they can be sensitive to strong interactions even without breaking symmetry.

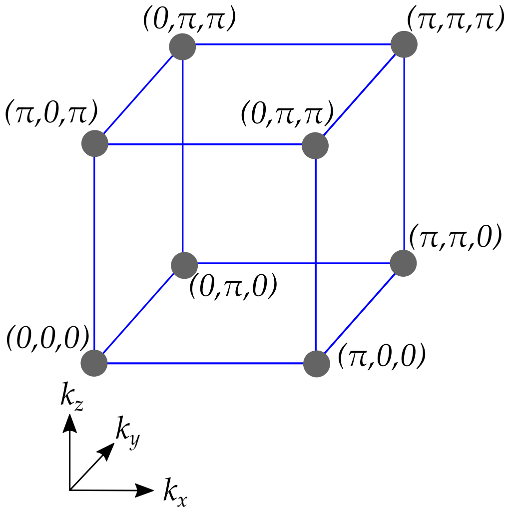

Figure 2.11: Time-reversal invariant momenta in three-dimensional BZ for a cubic lattice.

Chapter 3

Topological crystalline insulators

After the discovery of topological insulators and subsequent advancements in both theoretical and experimental research on real materials, the importance of crystal symmetry became evident and played a key role in realizing topological phases. As a result, space group symmetries became relevant to this field and simplified the calculation of topological invariants. For example, Fu and Kane introduced a formula for calculating $\mathbb{Z}_2$ invariants in the presence of inversion symmetry for class AII topological insulators [59]. Notably, this approach does not require a continuous global gauge for Bloch wave functions; it solely concerns to the parity of filled bands at TRIM points in the Brillouin zone.

In 2011, Liang Fu introduced another phase of topological material known as *topological crystalline insulators* (TCIs). In this class, the topological classification of the band structure is crucially dependent on a certain crystal point group symmetry [71]. Initially, this extension was proposed for a simple tight-binding model in a tetragonal crystal with C_4 symmetry. Later on, the TCI phase was generalized into mirror symmetry or a combination of mirror and rotation symmetries. Typically, The TCIs are usually identified with two notions: i) their bulk ground state is not adiabatically transformed to an atomic limit without breaking the protecting symmetry. ii) they have gapless boundary modes which can only be gapped out by breaking the respective symmetry [72]. In other words, the gapless symmetry-protected boundary modes also necessitate the boundary on which they are localized to maintain the corresponding symmetry. To conduct a thorough exploration for TCIs, it is necessary to categorize the different band structures that exist within each crystal class. Due to the intricate and multifaceted nature of crystallography, a comprehensive classification of TCIs has yet to be achieved and remains an active area of current research [18].

In this Chapter, we present various pedagogical examples based on SnTe class of topological crystalline phases, which has been experimentally and theoretically realized [7, 9, 10, 73]. This class of phases primarily comprises materials constructed from IV-VI semiconductors, wherein the topological character is protected by mirror symmetry.

3.1 TCIs protected by mirror symmetry

The mirror reflection operator M is the combination of inversion symmetry (parity) P and rotation symmetry C_2 around the axis that is perpendicular to the mirror plane, $M = PC_2$. For a spinful system, $M^2 = -1$, and the eigenvalues of the operator M are $+i$ or $-i$. Suppose there is a system that has reflection symmetry perpendicular to the z axis. In this case, we can break down all the Bloch states $|\psi(\boldsymbol{k})\rangle$ of the Hamiltonian H into an eigenbasis of mirror eigenvalues $\eta = \pm i$ at each k point lying on the 2D mirror plane in the BZ. The Chern number can be calculated in each subsystem as C_η, and the total Chern number can be given by $C = C_{+i} + C_{-i}$, which determines the quantized Hall conductance. In the case of a system with TRS where $C_i = -C_{-i}$, a new invariant can be derived known as the *mirror Chern number* denoted by $C_m = (C_{+i} - C_{-i})/2$ [18, 71, 74, 75].

3.2 TCIs in IV-VI semiconductor

IV-VI compounds are classified as a narrow bandgap semiconductors. They have been long attracted attention due to its unique properties in optoelectronic applications such as infrared detectors [76], solar cells [77, 78] and thermoelectric devices.

The topological properties of IV-VI binary compound $\mathrm{Pb_{1-x}Sn_xTe}$ make it a promising candidate for a wide range of applications, including spintronics, and quantum computing devices. In 2012, the first realization of TCIs was predicted in SnTe material class by Timothy H. Hsieh et al. [7]. These materials have a rock-salt structure and the band gap is located at four non-equivalent L point in the face-centered cubic (fcc) BZ. The theoretical analysis has shown that the $\mathbb{Z}_2$ invariant in this class is zero, indicating the irrelevance of TCI phase to TRS. The nontrivial topology is defined on the $\{110\}$ momentum mirror plane with mirror Chern number equal $|C_m| = 2$. This integer number determines the number of surface states that disperse along each momentum mirror plane edge. The sign of mirror Chern number shows the chirality of spin texture [7, 74, 79].

3.2.1 Four band k.p model

In low energy limit near the given L point, the electronic band structure is doubly degenerate. The low energy k.p model that describes this system can be obtained purely from the symmetry properties of the energy bands. The little group that keeps each L point invariant is D_{3d}, a subgroup of the O_h point group of the rock-salt structure [18]. The group D_{3d} possesses three independent symmetry operations, including inversion (P), three mirror reflections M with respect to the $\{110\}$ plane, and rotation symmetry C_3 around the (111) axis. The conduction and valence bands at a given L point form two sets of Kramers douplets with opposite parity eigenvalues, denoted by $|\psi^{+}_{L,\alpha}\rangle$ and $|\psi^{-}_{L,\alpha}\rangle$, respectively. The Kramers douplets, denoted by $\alpha = 1, 2$, possess opposite angular momenta, $J_z = \pm\hbar/2$ about (111) axis, respectively. Since the axis of rotation is parallel to the planes of reflection, J_z changes sign under reflection. Thus, $M|\psi^{\pm}_{L,1}\rangle = i|\psi^{\pm}_{L,2}\rangle$ and $M|\psi^{\pm}_{L,2}\rangle = i|\psi^{\pm}_{L,1}\rangle$. Therefore, the effective k.p Hamiltonian can be expressed in the basis of $\{|\psi^{+}_{L,1}\rangle, |\psi^{+}_{L,2}\rangle, |\psi^{-}_{L,1}\rangle, |\psi^{-}_{L,2}\rangle\}$ and is given by [18]

$$H(\boldsymbol{k}) = \begin{pmatrix} m & 0 & -iv'k_z & -v(ik_x + k_y) \\ 0 & m & v(ik_x - k_y) & -iv'k_z \\ iv'k_z & -v(ik_x + k_y) & -m & 0 \\ v(ik_x - k_y) & iv'k_z & 0 & -m \end{pmatrix}. \tag{3.1}$$

The Hamiltonian $H(\boldsymbol{k})$ has terms up to first order in $\boldsymbol{k}$ obeying D_{3d} symmetry and reminiscent to the Dirac Hamiltonian in quantum electrodynamics. Thus, the low-energy electronic properties of SnTe and PbTe are governed by massive Dirac fermions with a gap $E_g = |2m|$ separating the conduction and valence bands. Their dispersions are particle-hole symmetric and equal to $E_{c,v}(k) = \pm\sqrt{m^2 + v^2k^2}$ [18].

The conduction and valence bands of SnTe and PbTe exhibit inverted band ordering, and the band gap of $Pb_{1-x}Sn_xTe$ closes and reopens at a critical Sn composition of $x = 0.35$ [80], showing a topological phase transition. This is due to a sign change in the Dirac mass described in Eq. (3.1), suggesting that either SnTe or PbTe is topologically nontrivial. The mirror Chern number C_m associated with the $k_x = 0$ plane passing through Γ and two L points is affected by this sign change, and the simultaneous band inversions at the two L points on the $k_x = 0$ plane add up to an integer value of the mirror Chern number equals 2. Accordingly, one of the two materials must have a nonzero mirror Chern number $C_m = 2$ and feature a TCI phase protected by mirror symmetry.

To determine if SnTe or PbTe is topologically nontrivial, realistic band structure calculations are necessary. First principle calculations (see Fig. 3.1) shows that PbTe has a

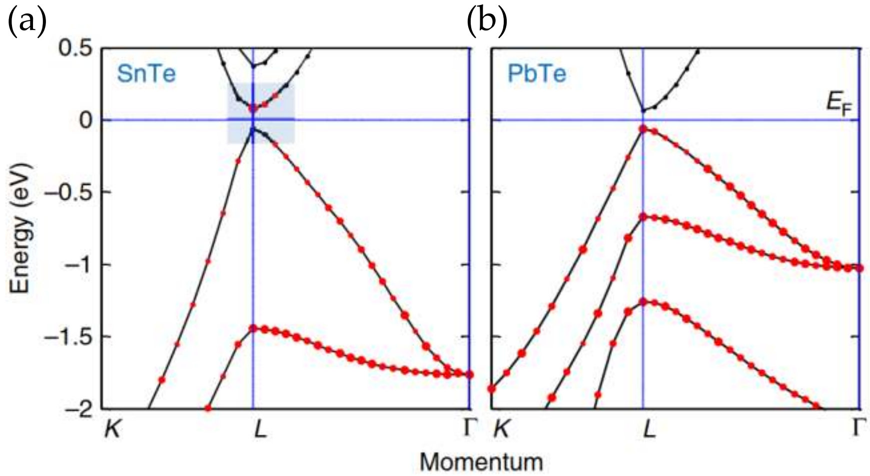

Figure 3.1: The electronic band structures of SnTe and PbTe are displayed in (a) and (b), respectively. The band inversion, highlighted in grey color, takes place at the gap edge near the L point for SnTe. The figure is taken from Ref. [7].

normal band ordering and SnTe has inverted band gap. This can be understood by inspecting wavefunctions near the band gap area. It was shown that the valence bands in PbTe are originated from the p orbitals of Te atoms (red dots) and conduction bands are originated from Pb p orbitals (black dots), which can be smoothly connected to the atomic limit. In contrast, SnTe exhibits a reversal of orbital contributions around the L points, indicating that the top valence bands are contributed by p orbitals of Sn atoms (black), whereas the bottom of the conduction bands originates from p orbitals of Te atoms (red) (the region highlighted in gray). The other states deep within the valence or conduction bands, however, have similar orbital contributions to PbTe. Therefore, the adiabatic deformation of SnTe band structures to the atomic limit is not a continuous process and leads to a band inversion. Based on low-energy theory, topological band theory, and ab initio calculations, Hsieh et al. [7] predicted that SnTe is a TCI while PbTe is not.

3.2.2 TCI surface states

Three-dimensional TCIs with non-zero mirror Chern number lead to gapless surface states. Depending on the surface orientations, the four L point in the bulk BZ can give rise to two qualitatively different types of topological surface states as illustrated in Fig. 3.2 [8, 81, 82]. In this section we will provide a brief discussion on two commonly studied surfaces of SnTe-type TCIs, namely the (001) and (111) surfaces.

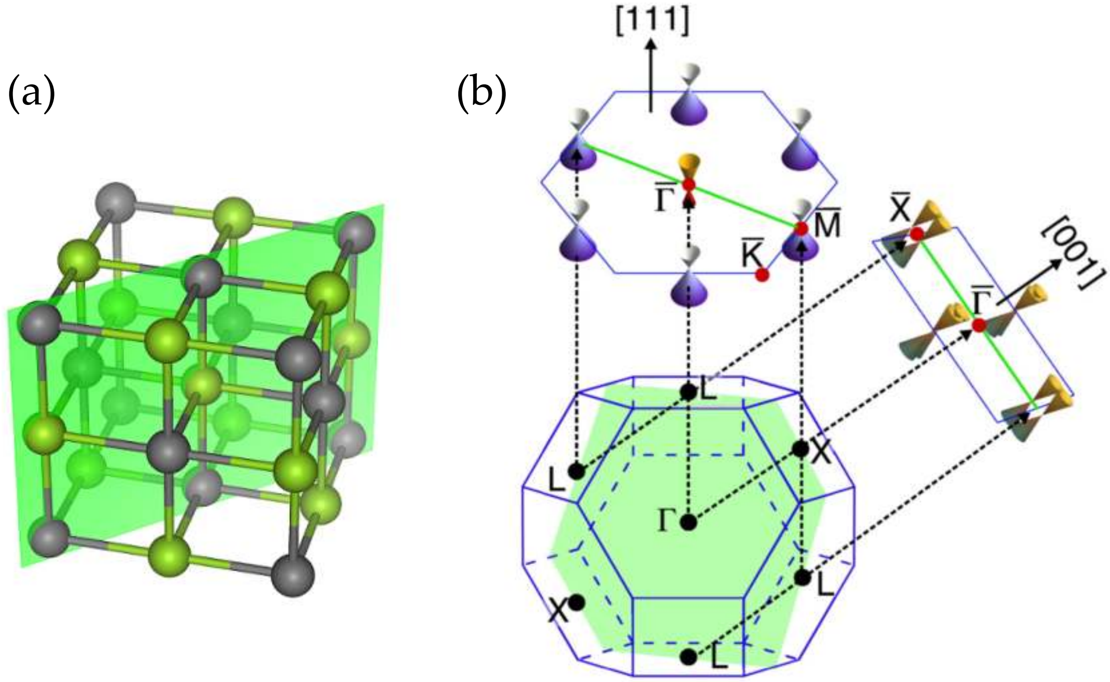

Figure 3.2: (a) IV-VI rocksalt crystal structure and fcc BZ (b) with its projection along [001] and [111] directions [8]. The Dirac cones come in pairs in (001) surface while they are separated in (111) surface. Copyright (2013) by the American Physical Society.

(111) surface

In the fcc BZ of the 3D rocksalt bulk crystal, there are six $\{110\}$ mirror planes. However, when considering the surface of the crystal, some of these mirror symmetries are broken. For example, in the (111) surface, three $\{110\}$ mirror symmetries are preserved, while the remaining mirror symmetries are broken by the surface. The projection of four L points in the fcc BZ disperses into four distinct points within a 2D hexagonal BZ, with one located at $\overline{\Gamma}$ and the remaining three at $\overline{M}$ points [Fig. 3.2(b)]. The $\{110\}$ mirror symmetries are linked by C_3 rotation symmetry along [111] axis. However, in Fig. 3.2(b) only one of three $\{110\}$ mirror planes is shown. The surface termination of the crystal can be exclusively composed of either cations or anions. Figure 3.3(a) displays the electronic band structure for $Pb_{0.4}Sn_{0.6}Te$ on this surface, with a 451 atomic layer thickness along $\overline{K} - \overline{\Gamma} - \overline{M} - \overline{K}$. The calculated band structure is cation-terminated and exhibits massless Dirac fermions clearly at $\overline{\Gamma}$ and $\overline{M}$ points [83]. The line color changes from yellow to blue depending on whether the cation (yellow) or anion (blue) p-type orbitals give the dominant contribution to the wave function. These theoretical predictions have been confirmed in various ARPES experiments [8, 84, 85].

(001) surface

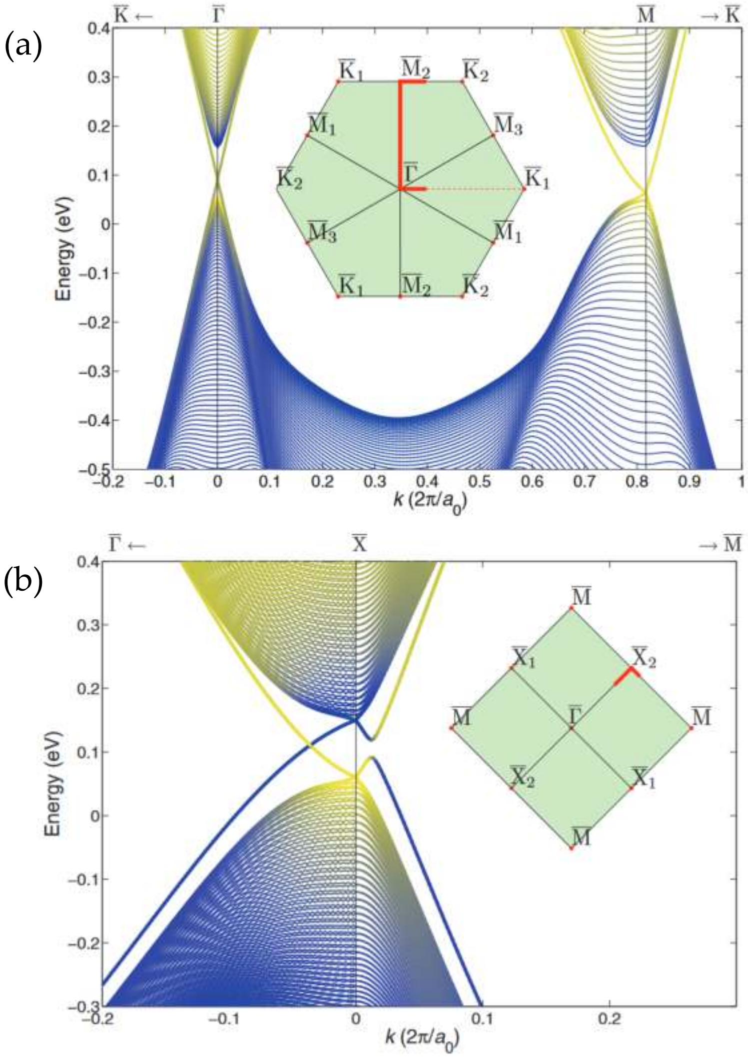

Figure 3.3: The calculated band structures of (a) the (111) surface with a 451-monolayer-thick cationic termination slab and (b) the (001) surface with a 280-atomic-layer slab for Pb$_{0.4}$Sn$_{0.6}$Te are presented, with each 2DBZ shown in the insets. The blue-to-yellow color coding indicates the contributions of the anion (blue) and cation (yellow) p orbitals to the wave functions. The figure is taken from Ref. [83]. Copyright (2013) by the American Physical Society.

In contrast to the previous case, the (001) surface states are more complex and fascinating. Figure.3.2(b) demonstrates that two distinct L points are projected to the same surface momenta for the (001) surface, resulting in four protected topological surface states (TSSs) within one surface BZ, consistent with the number of band inversions in the bulk BZ. In this surface, two $\{110\}$ mirror planes are survived and the rests are broken [only one of them is demonstrated in Fig. 3.2(b) in the fcc BZ]. In particular, Fig.3.3(b) shows the calculated band structure for the (001) surface of Pb$_{0.6}$Sn$_{0.4}$Te, with a thickness of 280 atomic layers [83]. Each $\overline{\Gamma} - \overline{X} - \overline{\Gamma}$ mirror line contains two TSSs, consistent with the mirror Chern number result of $|C_m| = 2$. It is also noteworthy that due to the interaction between the L valleys, the dispersion features two separated Dirac points at $\overline{X}$ and two secondary Dirac points Λ in the middle of the gap, which are moved away from $\overline{X}$ along mirror-symmetric $\overline{\Gamma} - \overline{X}$ line [83].

In 2012, several ARPES experiments confirmed all the aforementioned features. Tanaka et al. confirmed these features in SnTe [73], Xu et al. observed them in Pb-rich $Pb_{0.6}Sn_{0.4}Te$[9], and Dziawa et al. reported them in $Pb_{0.77}Sn_{0.23}Se$. Xu et al. performed spin-resolved ARPES measurement to experimentally determine the topological mirror Chern number of $C_m = -2$ in $Pb_{1-x}Sn_xTe$. This experimental result confirmed the topological mirror nontriviality of the TCI phase in the $Pb_{1-x}Sn_xTe(Se)$ system, as discussed in Ref. [9, 86].

The discovery of TCI phase in the $Pb_{1-x}Sn_xTe(Se)$ semiconducting system has led to numerous groundbreaking advancements and has attracted a significant amount of research attention. Subsequent developments in this field have encouraged further exploration and investigation of various aspects of the TCI phase [8, 81, 83, 84, 87–94]. These studies have contributed significantly to our understanding of the TCI phase and its potential applications.

3.2.3 Topological phase in SnTe TCI thin films

Large slabs or semi-infinite systems have similar band inversion to ordinary 3D bulk. But reducing slab thickness strengthens confinement, potentially lifting or enhancing band inversion and nontrivial topology. Surface states from top and bottom start hybridizing significantly affecting thin film band structures and topological phases. Hybridization also depends on intrinsic bulk gap, film growth direction and other details, varying for different materials [75].

Here, we will consider SnTe as an example to demonstrate how topological phases vary with film thickness, focusing on (001) and (111) oriented films and their symmetry protections.

(001) TCI films

The (001) surface of SnTe exhibits Dirac cones at four $\overline{X}$ points within its 2D BZ. Interestingly, these Dirac points occur at non-TRIM points, located away from the $\overline{X}$ point in the 2D BZ [refer to Fig.3.3(b)]. As the thickness of the (001) slab is reduced, approaching the penetration depth of surface Dirac cones, the Dirac fermions on the top and bottom surfaces will hybridize with each other and form additional band structures which are not normally existed in the bulk gap. This results in gapping out the primarily protect crossings (secondary Dirac points) at Λ, as depicted in the inset of Fig.3.4(a). For odd numbers of atomic layers, the (001) thin films of SnTe have a mirror symmetry with respect to the $z = 0$ plane. The Hamiltonian is invariant under mirror symmetry about the 2D plane and commutes with it, i.e.,

$$MH(\boldsymbol{k})M^{-1} = H(\boldsymbol{k})\,. \tag{3.2}$$

Hence, the mirror Chern number N_m can be defined for odd (001) film thicknesses. An orbital analysis reveals that within a specific range of film thicknesses, the bands undergo inversion, resulting in a two-dimensional TCI with a mirror Chern number of $|N_m| = 2$. [Fig. 3.4(b)]. The even mirror Chern number implies that the band inversion occurs simultaneously at two $\overline{X}$ points, inevitably leading to 2D TCI phases protected by the (001) mirror plane. The band gap at the $\overline{X}$ point exhibits oscillatory behavior as the thickness of the (001) film increases. Using the recursive Green's function method, it was shown that for 11 atomic layers, there are two pairs of counter-propagating edge states in the band gap that correspond to a mirror Chern number of $N_m = 2$ [Fig. 3.4(c)]. It should be mentioned that edge modes moving in the same (opposite) direction have identical (opposite) mirror eigenvalues. The introduction of a small out-of-plane electric field disrupts this mirror symmetry, causing the spin-filtered edge states to become gapped out, as shown in Figure 3.4(d) [13]. This is because the low-energy states are not protected by time-reversal symmetry and can be lifted even by non-magnetic perturbations. However, in the case of an even number of layers, no such mirror plane exists, but gapless/gapful mirror-helical edge states are present. The films consisting of an even number of layers lack (001) reflection symmetry but possess glide symmetry instead. Nevertheless, it is still feasible to decompose the Hamiltonian into mirror sectors. In the case of films with an odd number of layers, TRS is broken within each mirror eigenspace. In contrast, for even-layer films, TRS is preserved within each mirror eigenspace. As a result, the mirror Chern number becomes zero, and the nontrivial topology for even-layer films can be described by glide-winding number ζ_M, as indicated in a study by Ozawa et al. [95].

Symmetry analysis can provide further validation of the aforementioned results. Liu et al. [13] introduced an effective model that describes the band inversion and mirror Chern number obtained. In addition, for different Sn contents in $\mathrm{Pb_{1-x}Sn_xTe}$, similar research has been conducted, which reports energy gap damped oscillation over a broader range of thicknesses [95]. The presence of an electrically tunable edge channel in (001) films can be considered a significant finding in the field of TCIs. This edge channel can be thought of as a topological transistor which can be controlled by an electrically induced gap in the topological edge channel. The results shed light on the electronic states and transport properties of the film, may have immense potential for use in new TCI devices.

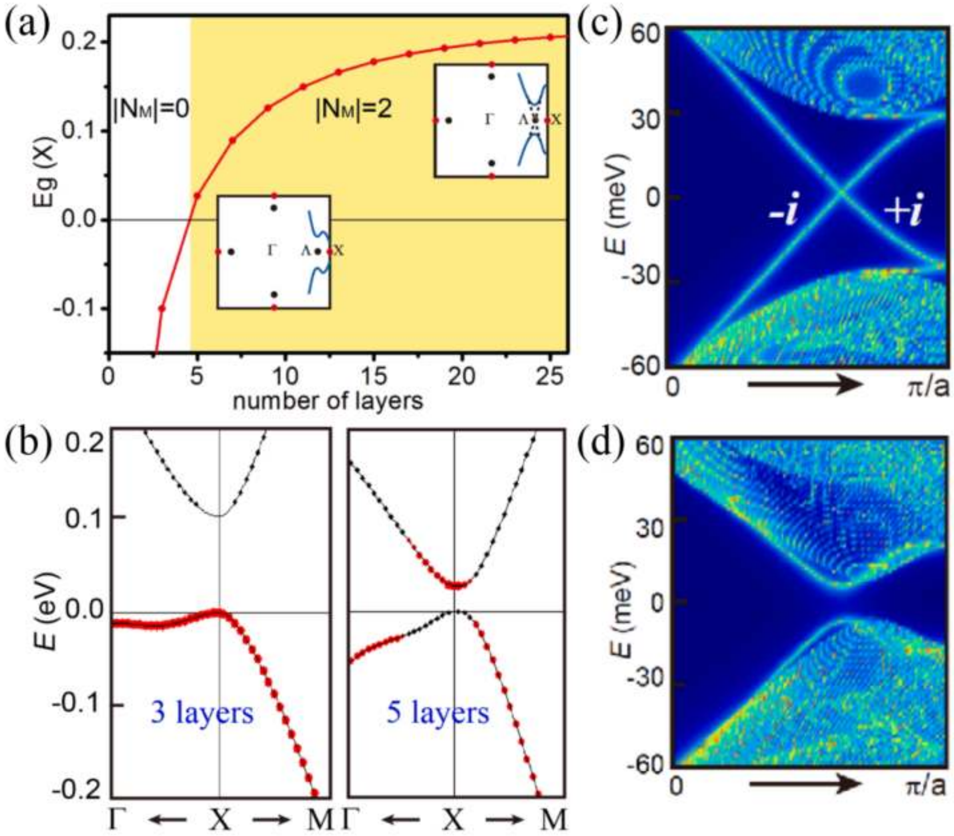

Figure 3.4: 2D TCIs in (001) thin films of SnTe. (a) Dependence of gap at $\overline{X}$ point $E_g(\overline{X})$ on SnTe thin film thickness, with schematic band structure insets for very thin and thick films; (b) Band structures of 3- and 5-layer SnTe thin films, highlighting Te atom contributions in red; (c) Topological edge states of 11-layer SnTe thin films. The figure adapted from Ref. [75], however, original data reported on Ref. [13].

Evidence of QSH phase in (111) TCI films

Moving forward to SnTe-type films, theoretical research has demonstrated that (111)-oriented films can experience a topological phase transition when their thickness is varied. Pioneering studies by Liu et al. [12] and Safaei et al. [11] have predicted the existence of a quantum spin Hall phase across a wide range of film thicknesses. This is due to the non-equivalence of the projections of the four L points onto the 2D BZ of a (111)-oriented thin film. The energy band structures at the $\overline{\Gamma}$ and $\overline{M}$ points are different whereas the three $\overline{M}$ projections are the same by symmetry [11].

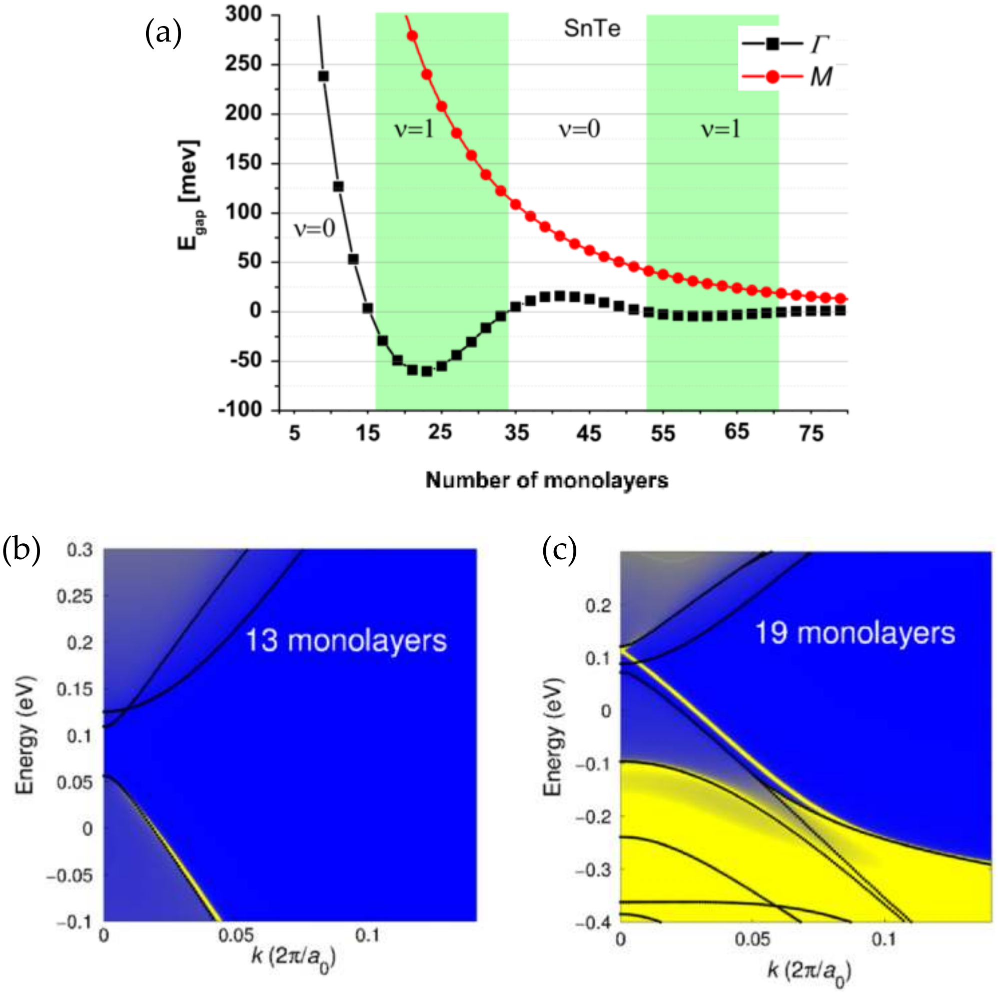

Figure 3.5: Energy gaps in (111) films with odd atomic layer numbers and their $\mathbb{Z}_2$ invariant dependence on thickness for SnTe. (b) and (c) display the $[1\bar{1}0]$ edge spectral functions at $\bar{\Gamma}$ point in cation-terminated (111)-SnTe film for 13 and 19 atomic layers, respectively. The black dotted lines indicate the local extrema of the 2D bands projected onto the edge. The figure is taken from [11].

Within these 2D systems, two structures with slightly differing symmetries exist. As the (111) plane is polar, the film termination can either be made up of cation or anion atoms. When there are an even number of monolayers in (111)-oriented slabs, one surface is cation-terminated while the other is anion-terminated. However, in slabs with an odd number of layers, both surfaces are identical, which preserves inversion symmetry. Liu et al. [12] suggested that the effective k.p Hamiltonian can be defined at the $\overline{\Gamma}$ point, as follows:

$$H(\boldsymbol{k}) = v(k_x s_y - k_y s_x)\tau_z + \delta\tau_z + m\tau_x \,, \tag{3.3}$$

where v represents velocity and δ is the energy difference of the Dirac points of the top and bottom surfaces, denoted by Pauli matrix τ_z. The hybridization between the two surfaces is given by $m\tau_x$ and s is the Pauli matrices act in the space of Kramers doublet. The $\delta = 0$ causes the two degenerate Dirac cones corresponding to an inversion-symmetric film, in which both surfaces consist of the same type of atom.

More realistic tight-binding model was used for further calculations [11, 12]. Unlike in (001) films, the mirror Chern number cannot be calculated in (111) films due to the absence of (111) mirror symmetry. Using the methods described in Ref. [58, 59, 61], the topological phases were defined by $\mathbb{Z}_2$ invariant. The topological invariant exhibits oscillatory behavior as the number of layers increases. Oscillations were predicted for both odd- and even-monolayer films [11, 12]. Specifically, Fig.3.5(a) illustrates the energy gap oscillation, also represented by $\mathbb{Z}_2$, for odd (111) films. Figure 3.5(b) displays the trivial edge spectral function for 13 atomic-layer thickness, which agrees with $\nu = 0$. However, the calculated edge spectrum in Fig. 3.5(c) confirms the presence of a helical edge mode at the $\overline{\Gamma}$ point, indicating the QSH phase.

3.3 Perturbations in TCIs

Compared to TIs, TCI surface states possess a wider range of modifiable electronic properties due to their susceptibility to various perturbations. One such example is the nonzero mass generation of massless Dirac fermions in the TCI (001) surface through ferroelectric structural distortion, which breaks a specific mirror symmetry [87]. Additionally, magnetic doping can create Zeeman gaps, providing a promising pathway towards quantum anomalous Hall states [96]. Furthermore, mechanical strain can cause a shift in the positions of Dirac points in k-space and produce a nonzero pseudomagnetic field [97, 98].

The presence of disorder inevitably breaks spatial symmetries [99], leading to concerns about the stability of TCIs against disorder. However, it has been demonstrated that the topological surface states in the SnTe class of TCIs remain delocalized even under strong disorder in ternary crystalline solid solutions as long as time-reversal symmetry is present. This is because of the restored mirror symmetry (average mirror symmetry) [7, 100], which ensures that the conducting domain wall permeates the entire surface, thereby preventing localization. This phenomenon is not limited to TCIs but also occurs in other topological phases, such as statistical topological insulators, which are protected by different symmetries. The precise formulation of this delocalization due to topology and average symmetry has been achieved through a field-theoretic approach to Anderson localization [100].

The previous section demonstrated that the topological properties of (001) and (111) films can be significantly altered by manipulating their thickness. This is due to the hybridization of top and bottom surface states. In the case of (001) films in the intermediate thickness range, a two-dimensional TCI phase is observed, while a QSH phase is predicted for (111) films. These phases can be electrically tuned, as reported in [12, 13].

3.4 Higher order topological insulators

Thus far, we have considered d-dimensional topological systems possessing $(d-1)$ dimensional boundaries that are capable of accommodating gapless states, commonly referred to as first-order topological insulators. In contrast, higher-order topological insulators (HOTIs) constitute a recently identified category of topological phases of matter characterized by lower-dimensional boundary states, such as zero-dimensional corner states or one-dimensional hinge states. These intriguing materials may be synthesized through the mechanism of symmetry breaking or higher-order polarizations, and have emerged as a vibrant field of investigation since their inception in 2018 [33, 101].

Benalcazar et al. investigated topological corner excitations in 2D and 3D electric multipole insulators [102, 103], while Schindler et al. proposed mirror symmetries in TCIs and bismuth crystals with three-fold rotational symmetry and inversion symmetry as additional categories of HOTIs [17, 104]. Tin telluride, an IV-VI semiconductor under strain, was predicted to be a helical HOTI featuring one-dimensional conducting modes at the intersection of two faces [17]. SnTe NWs with $\{001\}$ facet provide an intriguing avenue for exploring the interplay between topology and different types of symmetry breaking. Recent work by Nguyen et al. [105] has revealed that this interplay can result in the emergence of robust corner and hinge states, which may have significant implications for the observation of Majorana bound states in the presence of superconductivity. Additionally, the varying confinement strengths of the Dirac states on different facets of the NWs result in the presence or absence of novel Aharonov-Bohm oscillations, as reported in Ref. [106].

3.4.1 SnTe as a higher order topological insulators

As expounded upon in this chapter, the bulk topology of SnTe is characterized by the $\{110\}$ family of mirror symmetries, with a mirror Chern number of $C_m = 2$ [7]. Given that the (110) surface features two Dirac cones on its surface BZ, one can manipulate the surface by tilting it out in two opposite directions—one along $(1+\alpha, 1-\alpha, 0)$ and the other along $(1-\alpha, 1+\alpha, 0)$, as shown in Fig. 3.6. The gapless surface states on each side will be gapped out, except for the intersection line of the two surface sides which is protected by $(1\bar{1}0)$ mirror plane. The relationship between the bulk topological invariant C_m and the presence of Kramers paired hinge modes, was further explained by Schindler et al. in Ref. [33].

They designed a 3D structure with a square (or rhombic) cross-section that is periodic along the z direction and has an open geometry along the x and y directions [see Fig. 3.6]. The square cross-section possesses C_4 symmetry, which preserves the two mirror symmetries, M_{xy} and $M_{x\bar{y}}$. To induce hinge modes, uniaxial strain was applied along the (110) direction of SnTe, breaking the symmetries M_{xz}, $M_{x\bar{z}}$, M_{yz}, and $M_{y\bar{z}}$, while keeping the two mirror planes M_{xy} and $M_{x\bar{y}}$ unchanged. As a result, the (100) and (010) surfaces in the geometry depicted in Fig. 3.6(d) became completely gapped. Figure 3.7 illustrates the electronic band structures obtained from a TB calculations (model from Ref. [7]) with (110) strain. The results demonstrate the existence of one Kramers pair of gapless hinge modes on all four hinges near $k_z = \pi$. It should be noted that, in order to minimize the hybridization in both the x and y directions, 111 atomic layers were considered. Furthermore, hinge states were also observed in the undistorted case, where a flat band disperses within the surface gap [33, 72].

3.5 Other TCI material candidates

Symmetry-based indicators provide direct information about the topological nature of materials, including whether they are topological insulators, topological crystalline insulators, or topological semimetals. These indicators also provide possible sets of topological invariants [107–109].

Recent advancements in the field of TCIs have identified several material candidates with unique topological properties. For example, zirconium titanium hydride $(\mathrm{Zr(TiH_2)_2})$

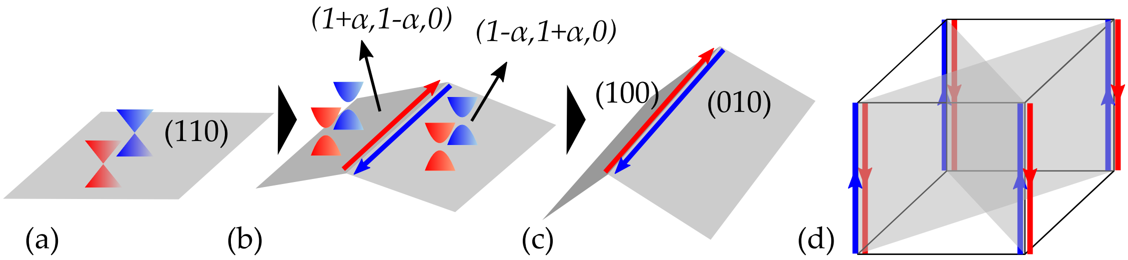

Figure 3.6: Constructing a 3D second-order TI. Ordinary surface states on a (110) TCI surface (a) as it is tilted out of the mirror plane leads to the formation of Kramers pairs of domain wall states (panel (b)). The hinge modes' mirror eigenvalues are linked to the mirror Chern number C_m, a bulk topological invariant. Deformation to other orientations in a mirror symmetry–preserving manner does not change this correspondence. (d) Time-reversal antipropagating Kramers pairs of hinge modes protected by mirror symmetries (grey planes) . Reproduced from [33].

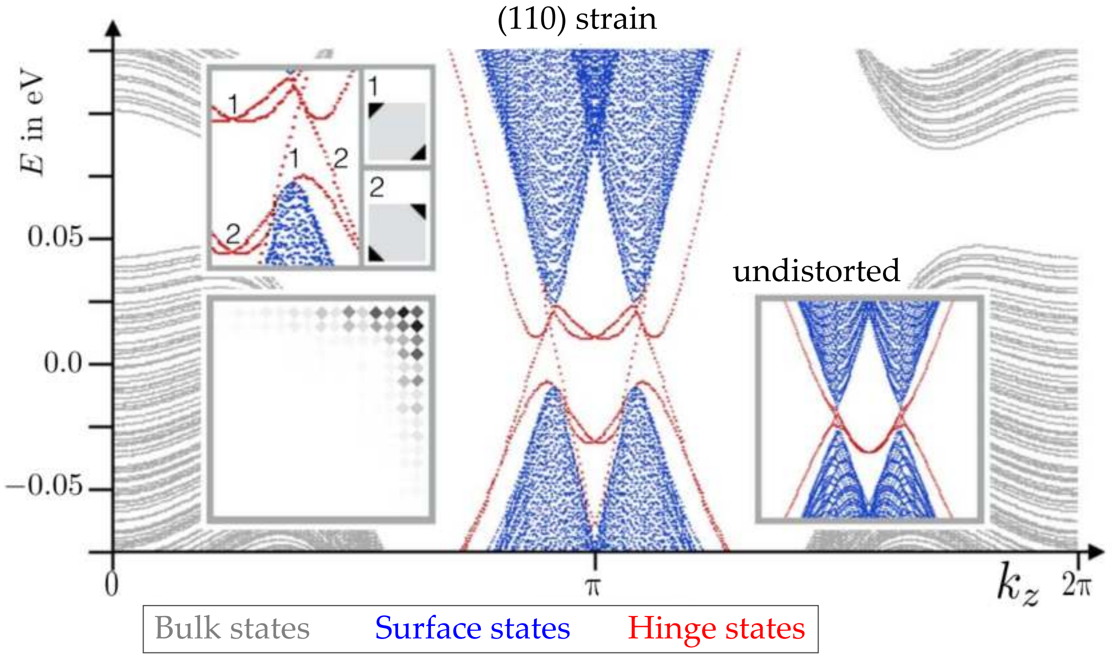

Figure 3.7: Emergence of hinge state in 3D SnTe. In a finite-sized (111 × 111) SnTe sample with a square cross-section periodic along the z axis, the second-order hinge states are accompanied by first-order surface states. Uniaxial (110) strain is added to the system to break symmetries, while keeping M_{xy} and $M_{x\bar{y}}$ unchanged. Four Kramers pairs of hinge modes, localized on each hinge, are found near $k_z = \pi$. The upper left inset shows the close-up view of gapless modes, while the lower left inset displays the localization of one such mode near a hinge. The right inset shows the electronic structure of undistorted SnTe in the same geometry, revealing two flat band hinge modes in addition to the gapless surface Dirac cones. The figure is taken from Ref. [33].

has been realized as a potential material with a screw-axis $\mathbb{Z}_2$ TCI with SOC. This material exhibits one-dimensional helical edge states, without the presence of 2D surface states, under specific sample configurations [110]. Theoretical calculations have also predicted that $ThTaN_3$, a rare cubic perovskite nitride semiconductor, can be realized as a TCI. In the presence of SOC, $ThTaN_3$ has a mirror Chern number of $|C_m| = 2$, protected by mirror and C_4 rotational symmetries [111]. Another class of TCIs has been discovered within the antiperovskite material family, particularly in compounds with the chemical formula A_3BX, such as Sr_3PbO and Ca_3PbO. These inverted antiperovskites belong to the same universality class as SnTe and are protected by mirror symmetry [112]. Ca_2As, a class of intermetallic materials that crystallize in the body-centered-tetragonal lattice system (with D_{4h} point group symmetry), emerges TCI phase which is protected independently by rotational and mirror symmetries [113].

There are numerous unexplored proposals concerning TCI material candidates. A comprehensive catalogue and tables of various topological classes, including TCIs based on their point group symmetry, can be found in Refs. [107–110, 114].

Chapter 4

Methodology

In condensed matter physics, the investigation of electronic properties in crystals is crucial due to its significant impact on a wide range of technological applications, including semiconductors and insulators. Several approaches are available for retrieving properties of solids with varying complexity, accuracy, and underlying physical approximations. Among these approaches, the tight-binding (TB) method, which utilizes Bloch's formalism and linear combination of atomic orbitals (LCAO), is widely used in solid-state physics. The TB method is developed using atomic orbitals of isolated atoms and was effectively implemented by Slater and Koster in two center approximation [115]. The resulting wavefunction derived from the TB method can be used to determine electronic properties of the crystal, such as its band structure, density of states, and transport properties.

The TB method is regarded as a valuable tool in various scenarios, particularly for studying different crystal geometries and incorporating strain or disorder into the system with relatively low computational effort. Moreover, the TB Hamiltonian can be readily employed to calculate Green functions, particularly for semi-infinite systems. The present study utilizes the TB method, employing the Slater-Koster (SK) approach to investigate the topological properties of IV-VI semiconductor nanostructures in cubic crystals.

4.1 Tight-binding method

In solid-state physics, the Bloch theorem is a fundamental principle that explains the behavior of electrons in a crystal lattice subjected to a periodic potential. The theorem posits that the single (also multiple) particle wavefunction of an electron moving in a spatially periodic potential has the form

$$\psi_{\boldsymbol{k}}(\boldsymbol{r}) = e^{i\boldsymbol{k}\cdot\boldsymbol{r}} u_{\boldsymbol{k}}(\boldsymbol{r})\,. \tag{4.1}$$

Here, $\boldsymbol{k}$ denotes a crystal wave vector and $u_{\boldsymbol{k}}(\boldsymbol{r})$ represents a periodic function with the same periodicity as the crystal. One can see that this is essentially a periodic function modulated by a plane wave described by a given wave vector. Furthermore, it is evident that the wavefunction acquires a phase upon translation by any Bravais lattice vector

$$\psi_{\boldsymbol{k}}(\boldsymbol{r}+\boldsymbol{R}) = e^{i\boldsymbol{k}\cdot\boldsymbol{R}}\psi_{\boldsymbol{k}}(\boldsymbol{r})\,. \tag{4.2}$$

As suggested by Bloch, electrons within crystals exhibit strong binding to their respective atoms and experience minimal interaction with the states and potentials of neighboring atoms in the solid. Consequently, the electron's wave function closely resembles its atomic orbital, allowing the total wave function to be effectively expressed using the LCAO [116]. Therefore, if $\phi_{\mu,s}(\boldsymbol{r}-\boldsymbol{t}_l-\boldsymbol{R})$ indicates atomic orbital function, where s denotes the spin state of the μth orbital and $\boldsymbol{t}_l$ is the position vector of the lth atom within the primitive unit cell at $\boldsymbol{R}$, the orbital and spin-resolved (Bloch) wave functions can be written as

$$\psi_{\boldsymbol{k},l\mu s}(\boldsymbol{r}) = \frac{1}{\sqrt{N}}\sum_{R} e^{i\boldsymbol{k}\cdot\boldsymbol{R}}\phi_{\mu,s}(\boldsymbol{r}-\boldsymbol{t}_l-\boldsymbol{R})\,. \tag{4.3}$$

The index $j = l\mu s$ simplifies the notation and the corresponding atomic orbitals $\phi_j(\boldsymbol{r}) = \phi_{\mu,s}(\boldsymbol{r}-\boldsymbol{t}_l)$ can be further simplified,

$$\psi_{\boldsymbol{k},j}(\boldsymbol{r}) = \frac{1}{\sqrt{N}}\sum_{R} e^{i\boldsymbol{k}\cdot\boldsymbol{R}}\phi_j(\boldsymbol{r}-\boldsymbol{R})\,. \tag{4.4}$$

The Schrödinger equation governs the behavior of electrons in a crystal. Applying the variational principle, the crystal wave function $\psi_{\boldsymbol{k}}(\boldsymbol{r})$ can be expanded in the basis of the on-site (Bloch) wave functions,

$$\begin{aligned} |\psi_{\boldsymbol{k}}\rangle &= \sum_j |\psi_{\boldsymbol{k}j}\rangle\langle\psi_{\boldsymbol{k}j}|\psi_{\boldsymbol{k}}\rangle && (4.5)\\ &= \sum_j |\psi_{\boldsymbol{k}j}\rangle C_j(\boldsymbol{k}) && (4.6) \end{aligned}$$

where $C_j(\boldsymbol{k})$ are yet to be determined coefficients. Eventually, the Schrödinger equation for a solid leads to the secular equation, which can be expressed as follows:

$$\sum_j \Big[H_{ij}(\boldsymbol{k}) - E(\boldsymbol{k})S_{ij}(\boldsymbol{k})\Big]C_j(\boldsymbol{k}) = 0\,. \tag{4.7}$$

Casting this equation into matrix form, we arrive at a generalized eigenvalue equation. Hence, a solution is formed by

$$\det\left[\tilde{H}(\boldsymbol{k}) - E(\boldsymbol{k})\tilde{S}(\boldsymbol{k})\right] = 0\,, \tag{4.8}$$

which gives us the energies for a given wave vector $\boldsymbol{k}$.

There are various challenges involved in numerically solving equation (4.7). Primarily, the computation of the Hamiltonian matrix and overlap matrix is essential. Additionally, the huge number of atoms in a given system poses a significant obstacle as it is impractical to consider all possible interactions. To address this issue, we utilize the methodology proposed by Löwdin to establish an orthogonal basis of atomic wave functions that still retain the symmetry properties of the initial orbitals [117]. Consequently, the overlap matrix $S_{ij}(\boldsymbol{k})$ in Eq.(4.7) is now a unitary matrix $\langle\varphi_i|\varphi_j\rangle = \delta_{ij}$, and $H_{ij}(\boldsymbol{k})$ can be expressed as

$$H_{ij}(\boldsymbol{k}) = \frac{1}{N}\sum_{\boldsymbol{R}_m,\boldsymbol{R}_n} e^{i\boldsymbol{k}\cdot(\boldsymbol{R}_n-\boldsymbol{R}_m)}\langle\varphi_i(\boldsymbol{r}-\boldsymbol{R}_m)|H|\varphi_j(\boldsymbol{r}-\boldsymbol{R}_n)\rangle\,, \tag{4.9}$$

due to the translational invariance of H, the parameter $\boldsymbol{R}_m$ in the aforementioned equation can be arbitrarily set to zero. Thus, by eliminating the summation over $\boldsymbol{R}_m$ and the scaling factor of $1/N$, the expression can be reconfigured as follows:

$$H_{ij}(\boldsymbol{k}) = \sum_{\boldsymbol{R}_n} e^{i\boldsymbol{k}\cdot\boldsymbol{R}_n}\langle\varphi_i(\boldsymbol{r})|H|\varphi_j(\boldsymbol{r}-\boldsymbol{R}_n)\rangle\,. \tag{4.10}$$

It is noteworthy that each term in this expression corresponds to a pair of orbitals located on adjacent atoms, encompassing not only the nearest neighbor atoms but also those beyond.

Equation (4.10) involves numerous integrals that must be computed, many of which are equal due to symmetry. Restricting the number of neighboring atoms and orbitals at a single atom simplifies the problem, although considering more neighbors and orbitals leads to improved electronic property descriptions but higher computational complexity. Additionally, the integrals in Eq. (4.10) diminish with increasing interatomic distance, albeit not as quickly as the original atomic orbitals. Hence, it is common to include only nearest and next-nearest neighbor interactions and neglect those beyond a certain threshold. For the systems considered in this work, nearest and next-nearest neighbours including s, p, and d atomic orbitals in the energy range of interest are considered.

4.1.1 Slater-Koster formalism

The integrals in the Hamiltonian can be categorized into three types based on the positions of atomic orbitals and potential. On-site integrals correspond to when both atomic orbitals and the potential are located at the same atom. Two-center integrals occur when the orbitals are localized at different atoms but the potential is localized at the same atom as one of the orbitals. Three-center integrals, where both orbitals and the potential are localized at different atoms, are neglected in this method. Additionally, two-center integrals where the orbitals are localized at the same atom but the potential is at a different one are also neglected. These simplifications are based on the relative magnitudes of the integrals and the desired accuracy of the calculations [118].

SK approximation can significantly reduce the number of two-center parameters needed to calculate the integrals [115]. The approach involves expressing the orbital basis functions in terms of cubic harmonics oriented along Cartesian axes, and using direction cosines, l, m, n of the vector connecting the orbital centers to calculate the integrals. The resulting parameters are written as $(ij\alpha)$, where i, j denote the orbital angular momenta and α the bond type. In this work, three-center integrals are neglected and the basis function ordering in the matrix Hamiltonian is: $s, p_x, p_y, p_z, d_{xy}, d_{yz}, d_{zx}, d_{x^2-y^2}, d_{3z^2-r^2}$. By using this approach, the number of two-center integrals can be significantly reduced, making calculations more computationally efficient [119].

The SK reference bonds for systems involving s, p and d orbitals are shown in Fig. 4.1. Here, two examples of integrals between two orbitals localized at different atoms (one at position zero and the other at position $\boldsymbol{R}$), using direction cosines (l, m, n), are shown below:

$$\langle p_x(\boldsymbol{R})|H|p_x(0)\rangle = l^2(V_{pp\sigma}) + (1-l^2)(V_{pp\pi})\,. \tag{4.11}$$

$$\langle p_x(\boldsymbol{R})|H|d_{xy}(0)\rangle = \sqrt{3}l^2m(V_{pd\sigma}) + m(1-2l^2)(V_{pd\pi})\,. \tag{4.12}$$

and two on-site integrals which represent the energies of the orbitals:

$$\langle p_x(0)|H|p_x(0)\rangle = \epsilon_p\,, \qquad \langle d_{xy}(0)|H|d_{xy}(0)\rangle = \epsilon_d\,. \tag{4.13}$$

The SK paper [115] provides a complete table of two-center parameters for $i = s, p, d$ orbitals. A noteworthy observation is that if the sum of the parities of the two orbitals in an integral is odd, then interchanging the order of the orbitals changes the sign of the integral. However, if the sum of the parities is even, the integral remains unchanged. Additionally, cyclic permutation of the coordinates and direction cosines leaves the integral value unchanged.

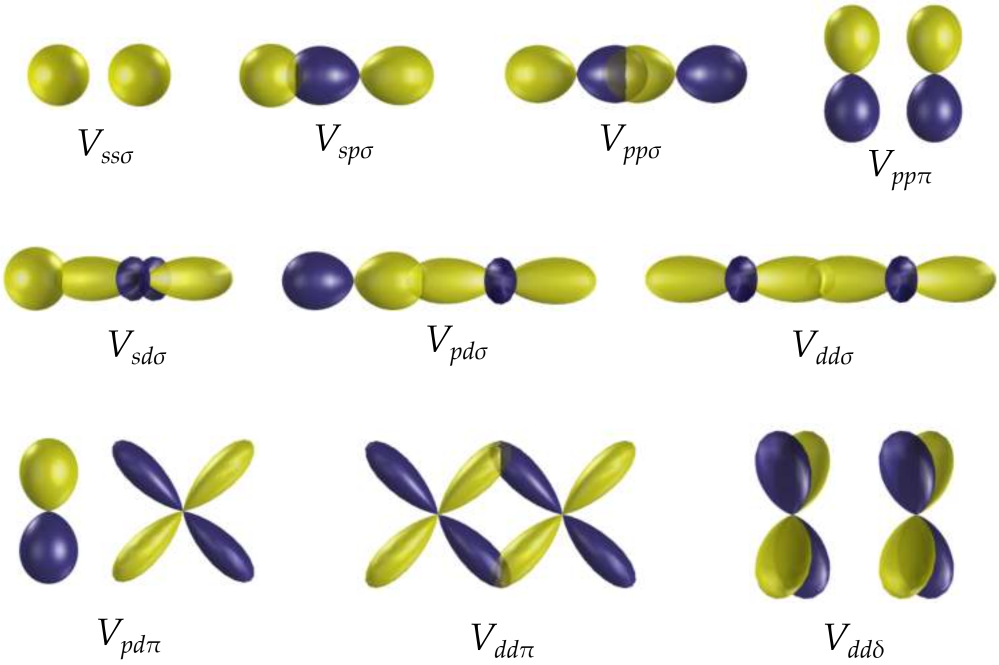

Figure 4.1: Schematic of the SK reference bonds for s, p and d orbitals. The labels correspond to the classic notation of Ref. [115].

4.1.2 Spin-orbit coupling

The Schrödinger equation must take into account the relativistic effect of spin-orbit coupling (SOC) [120], which connects the spin degree of freedom $\boldsymbol{S}$ with the electron's angular momentum $\boldsymbol{L}$. To account for this, we have expanded the basis set to include the spin degree of freedom ($s = \uparrow\downarrow$). This doubling of the basis set allows us to label spin-orbital states as: $|i, \alpha, s\rangle = |i, \alpha\rangle \otimes |s\rangle$ where i indicates the atomic sites and α indicates the orbital. The new basis of the Hamiltonian with respect to s, p, d atomic orbitals and spin is:

$$\left(s^{\uparrow}, p_x^{\uparrow}, p_y^{\uparrow}, p_z^{\uparrow}, d_{xy}^{\uparrow}, d_{yz}^{\uparrow}, d_{zx}^{\uparrow}, d_{x^2-y^2}^{\uparrow}, d_{3z^2-r^2}^{\uparrow}; s^{\downarrow}, p_x^{\downarrow}, p_y^{\downarrow}, p_z^{\downarrow}, d_{xy}^{\downarrow}, d_{yz}^{\downarrow}, d_{zx}^{\downarrow}, d_{x^2-y^2}^{\downarrow}, d_{3z^2-r^2}^{\downarrow}\right)$$

where z-direction is chosen as a quantization axis. Thus, the Hamiltonian shall take the subsequent shape [119]:

$$H = H_{TB} + H_{SO}\,. \tag{4.14}$$

The SOC part of the Hamiltonian can be written as

$$H_{SO} = \lambda \boldsymbol{L} \cdot \boldsymbol{S}\,, \tag{4.15}$$

using the total angular momentum $\boldsymbol{J} = \boldsymbol{L} + \boldsymbol{S}$, it is evident from Eq. (4.15) that SOC for s orbitals is zero. By expressing p orbitals as a linear combination of spherical harmonics and skipping some algebraic operations, the final non-zero elements of SOC part of H matrix can be determined as

$$\begin{aligned}&\langle p_x^{\uparrow}|H_{SO}|p_y^{\uparrow}\rangle = \langle p_y^{\uparrow}|H_{SO}|p_z^{\downarrow}\rangle = -\langle p_x^{\downarrow}|H_{SO}|p_y^{\downarrow}\rangle = -\langle p_y^{\downarrow}|H_{SO}|p_z^{\uparrow}\rangle = -i\lambda/2\\ &\langle p_x^{\uparrow}|H_{SO}|p_z^{\downarrow}\rangle = -\langle p_x^{\downarrow}|H_{SO}|p_z^{\uparrow}\rangle = \lambda/2\,.\end{aligned} \tag{4.16}$$

Reference [121] contains the components necessary for a TB model that incorporates d and f orbitals. It is important to note that this approach solely includes on-site elements of the SOC, and does not account for SOC between localized orbitals at different sites.

TB models of this study

The focus of this investigation is on the crystal structures of rock-salt containing IV-VI semiconductors, such as PbTe, PbSe, and SnTe. In the subsequent chapter, two TB models are utilized. One model is based on nearest-neighbor interactions, within a two-center approximation introduced by Lent et al. [122]. This model considers s, p, and d orbitals, and its corresponding TB parameters are presented in Table 4.1 [116]. It should be noted that V_{ps}, V_{pd} and $V_{pd\pi}$ parameters given in C. Lent et al. paper [122] are defined with signs opposite to the signs of these parameters in Slater and Koster notation. In our TB code, we rather use original SK definitions. Similar model is presented in Table 4.2 for SnSe rock-salt crystal structure (adapted from supplemental material of Ref. [11]). The TB parameters of ternary alloys $\mathrm{Pb_{1-x}Sn_xTe}$ and $\mathrm{Pb_{1-x}Sn_xSe}$ are chosen using virtual crystal approximation (VCA). Moreover, similar calculations are performed for SnTe in which only p orbitals with σ bonds between nearest and next-nearest neighbors are considered. The Hamiltonian for such a model is proposed by Hsieh et al. [7], and appropriate parameters are published in [123]. In our calculations we use spin-orbit parameter $\lambda = 0.3$ instead of $\lambda = 0.7$ in order to reduce band gap to 0.33 eV, which is close to SnTe gap in the ambient conditions. Such model captures all essential qualitative aspects of the TCI bulk spectrum while allowing efficient large-scale calculations. The corresponding SnTe TB parameters are presented in Table 4.3.

4.2 Green's function

The TB Hamiltonian is typically diagonalized to compute the energy of the periodic or small finite system. However, for electronic structure of semi-infinite solids, Green's function is a preferable method. Sancho et al. [65] introduced an iterative approach to solve linear chains of equations for the matrix elements of the Green operator $G(z) = (z - H)^{-1}$

TB parameters							
	SnTe	PbTe	PbSe		SnTe	PbTe	PbSe
E_s^c	-6.578	-7.612	-7.010	$V_{ps\sigma}$	-0.198	0.633	0.159
E_s^a	-12.067	-11.002	-13.742	$V_{pp\sigma}$	2.218	2.066	1.920
E_p^c	1.659	3.195	4.201	$V_{pp\pi}$	-0.446	-0.430	-0.356
E_p^a	-0.167	-0.237	-1.478	$V_{pd\sigma}$	-1.11	-1.29	-1.590
E_d^c	8.38	7.73	8.72	$V_{pd\pi}$	0.624	0.835	1.45
E_d^a	7.73	7.73	11.95	$V_{dp\sigma}$	-1.67	-1.59	-1.09
λ^c	0.592	1.50	1.693	$V_{dp\pi}$	0.766	0.531	0.0497
λ^a	0.564	0.428	0.121	$V_{dd\sigma}$	-1.72	-1.35	-1.90
$V_{ss\sigma}$	-0.510	-0.474	-0.402	$V_{dd\delta}$	0.618	0.668	0.692
$V_{sp\sigma}$	0.949	0.705	0.929				

Table 4.1: The nearest neighbour tight binding parameters of SnTe, PbTe, PbSe in [eV], taken from Ref. [116].

TB parameters of SnSe			
E_s^c	-0.655548	$V_{ps\sigma}$	0.3205
E_s^a	-12.851739	$V_{pd\sigma}$	-0.4400
E_p^c	2.331741	$V_{pp\sigma}$	2.3362
E_p^a	0.019397	$V_{pd\pi}$	1.0980
E_d^c	10.251989	$V_{pp\pi}$	-0.4157
E_d^a	9.512448	$V_{ds\sigma}$	-0.4124
$\Delta^c/3$	0.387556	$V_{dp\sigma}$	-1.9083
$\Delta^a/3$	0.103260	$V_{dp\pi}$	0.5482
$V_{ss\sigma}$	0.3821	$V_{dd\sigma}$	1.1437
$V_{sp\sigma}$	0.9118	$V_{dd\pi}$	0.6398
$V_{sd\sigma}$	0.3351	$V_{dd\delta}$	-0.3800

Table 4.2: The nearest neighbour tight binding parameters of SnSe in [eV], found using DFT-LDA method, reported in supplemental material of Ref. [11]. Δ denotes the spin-orbit coupling parameter.

p-orbital TB parameters of SnTe									
E_p^c	E_p^a	λ^c	λ^a	$V_{pp\sigma}$	$V_{pp\pi}$	$V'_{pp\sigma,cc}$	$V'_{pp\pi,cc}$	$V'_{pp\sigma,aa}$	$V'_{pp\pi,aa}$
1.65	-1.65	0.3	0.3	0.9	0	0.5	0	-0.5	0

Table 4.3: The nearest- and next nearest-neighbour (denoted by prime) tight binding parameters of SnTe [eV], based on the simplified model in Ref. [123]

in a basis of localized functions. The method replaces a chain with a new chain twice its size, where each layer and its two closest neighbors are replaced with a new effective layer. This process can be repeated until residual interactions between layers are sufficiently small. With n iterations, the iterative procedure includes 2^n layers, enabling the determination of relevant quantities such as surface or bulk density of states (DOS). This technique can be readily incorporated into the TB model using SK formalism in both orthogonal and non-orthogonal bases.

A semi-infinite crystal is constructed from atomic layers arranged in parallel to the surface. At each layer, Bloch states are characterized by a multi-index that encompasses information about the layer, atom and orbitals. The atomic layers can be combined into principal layers, with interactions limited to adjacent principal layers, as proposed by Sancho et al. [65, 124].

The transfer matrix (integral) denoted as H_{ij} in Eq. (4.10) only exists between adjacent principle layers. The subscript i combines information about the layer, atom, and orbitals into a single block matrix. Therefore, the Hamiltonian can be expressed as:

$$H = \begin{pmatrix} H^s_{00} & H^s_{01} & 0 & 0 & \cdots \\ H^s_{10} & H_{11} & H_{12} & 0 & \cdots \\ 0 & H_{21} & H_{22} & H_{23} & \cdots \\ 0 & 0 & H_{32} & H_{33} & \cdots \\ \vdots & \vdots & \vdots & \vdots & \ddots \end{pmatrix} \tag{4.17}$$

Here, layer "0" refers to either an edge or surface. It's important to recognize that the atomic arrangement at the surface may differ from that of the bulk, which can result in reconstruction and relaxation. To differentiate the surface matrices from their bulk counterparts, we use the superscript "s". The formula for the Green function, $(z - H)G = 1$, can be represented as a block-matrix

$$H = \begin{pmatrix} A^s & H^s_{01} & 0 & 0 & \cdots \\ H^s_{10} & A & H_{12} & 0 & \cdots \\ 0 & H_{21} & A & H_{23} & \cdots \\ 0 & 0 & H_{32} & A & \cdots \\ \vdots & \vdots & \vdots & \vdots & \ddots \end{pmatrix} \cdot \begin{pmatrix} G_{00} & G_{01} & G_{02} & G_{03} & \cdots \\ G_{10} & G_{11} & G_{12} & G_{13} & \cdots \\ G_{20} & G_{21} & G_{22} & G_{23} & \cdots \\ G_{30} & G_{31} & G_{32} & G_{33} & \cdots \\ \vdots & \vdots & \vdots & \vdots & \ddots \end{pmatrix} = \begin{pmatrix} 1 & 0 & 0 & 0 & \cdots \\ 0 & 1 & 0 & 0 & \cdots \\ 0 & 0 & 1 & 0 & \cdots \\ 0 & 0 & 0 & 1 & \cdots \\ \vdots & \vdots & \vdots & \vdots & \ddots \end{pmatrix} \tag{4.18}$$

where $z = E + i\eta$ and the abbreviation introduced as

$$A^s = z - H^s_{00}\,, \tag{4.19}$$

$$A = z - H_{11}\,. \tag{4.20}$$

Due to the semi-infinite geometry, the matrices involved in Eq.(4.18) have an infinite dimension, making it impossible to solve by simple inversion. However, this equation can be used to derive numerous other equations that combine block matrices. The complete derivation of the highly convergent procedure can be found in Ref. [65], for both bulk and clean surface cases with their corresponding bulk matrix elements. By employing iterative instructions with sufficiently large number of steps, the block matrices of the Green's function can be determined in the limit of $i \to \infty$. In practice, achieving convergence typically requires only a few steps, which depend on the desired parameter η (for smaller values of η, larger number of steps are needed to achieve convergence). Once the entire Green's function has been constructed, the layer-resolved DOS can be defined as [124]

$$N_m(E, \boldsymbol{k}) = -\frac{1}{\pi} \lim_{\eta \to 0^+} \Im \operatorname{Tr} G(E + i\eta, \boldsymbol{k})|_m \qquad \text{(surface)} \tag{4.21}$$

where the trace is restricted to the specified principal layer m.

Chapter 5

Results

5.1 Twinning superlattices

In Chapter 3, some interesting new discoveries regarding IV-VI TCI materials over the past decade were discussed. It was demonstrated that within this class, the nontrivial topology of the electronic band structures in the bulk is protected by crystalline symmetry [18, 75]. Significant progress has been made in this field, with extensive research conducted on this class of materials, including thin films [11–13, 95], heterostructures, and quantum wells [125–129]. Apart from clean surfaces, the introduction of certain lattice defects or disclinations in topologically nontrivial materials has led to the emergence of gapless topological states [130, 131]. Moreover, experimental and theoretical investigations have revealed 1D gapless modes bound to atomic step edges on the (001) surface [14–16, 132].

In this study, we broaden the investigation of the impact of lattice defects on the electronic structure topology to twin planes (TPs). The TPs arise as planar defects during crystal growth, along a specific crystallographic direction. In cubic crystals, these faults tend to occur mainly along the $[111]$ direction, without disrupting any bonds. Remarkably, they possess zero stress and exhibit very low formation energies [133]. These distinct characteristics ensure a remarkable level of symmetry and coherence, compared to other types of grain boundaries. They have been detected in IV-VI rocksalt crystal structures such as galena, which is rocksalt-type PbS [134]. Moreover, the theoretical investigations into the electronic properties of twin boundaries in some rocksalt crystals was reported in Ref. [135, 136].

TPs have also been observed in $\mathrm{Pb_{1-x}Sn_xTe}$ nanowires grown along the $[011]$ direction. The wires possess a pentagonal cross-section with five $\{111\}$ twins extending radially from the wire's center [137]. Inspired by the observation of TPs in these nanowires, we investigate the influence of [111] lattice twin boundaries on the electronic topology of

IV-VI semiconductors. For this purpose we first study TPs that made up in the twinning superlattices (TSLs). Similar TSLs have been extensively studied as a novel crystal structure class in semiconductors and metals with cubic and zinc-blende binary compounds [135, 138].

We study topological properties using a simplified p-orbital TB parametrization of SnTe compound. It will be shown that the presence of a coherent TPs in the supercell can induce a new topological phases in SnTe material class.

5.1.1 Structure

We consider hypothetical 3D twin superlattices (TSLs) with rocksalt structure grown along [111] direction, containing TPs that break some crystal symmetry and create local (111) reflection symmetry. The TSLs have two TPs in the supercell and exhibit three different configurations depending on whether they are all cationic (cat-cat), all anionic (an-an), or mixed (cat-an). The TSLs are built symmetrically with respect to each TP, and the atomic height of the supercell along [111] can be adjusted by setting a given atomic distance between the TPs. The space group of cat-cat and an-an TSLs is $P6_3/mmc$, while cat-an TSLs have a different space group denoted as $P\bar{6}m2$. These space groups belong to the hexagonal lattice system, but we use Miller indices for a original bulk cubic lattice to refer crystal planes and directions. The height of the supercell (d) along [111] can be tuned by adjusting the atomic distance ($l = d/2$) between the twin boundaries, as shown in Fig. 5.1.

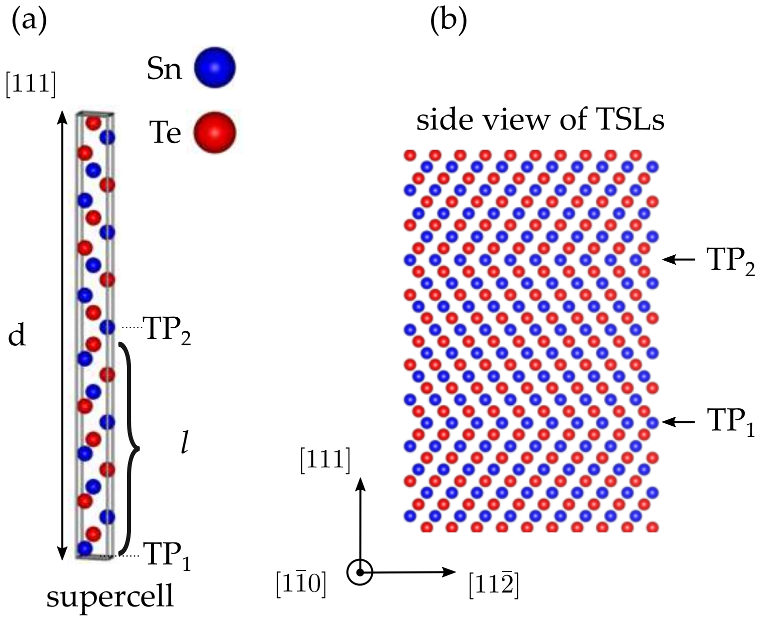

Figure 5.1: (a) A [111] primitive supercell with height consisting of $d = 28$ ($l = 14$) atomic layers. (b) A side view of a TSL 3D bulk in the (1$\bar{1}$0) direction.

Among many symmetries present in TSL systems, only a few of them are significant in this study. These notable symmetries include (111) reflection symmetry, {110} mirror symmetry, C_3 rotation symmetry, and inversion symmetry. They are all present in the TSLs with TPs of the same kind, whereas in the cat-an TSL the inversion symmetry is absent. Inversion, together with time-reversal symmetry, leads to at least a twofold degeneracy of the energy bands for cat-cat/an-an TSLs [133]. We note that {110} mirror symmetry is crucial for topological protection in defect-free SnTe materials.

The TSL structure has a simple hexagonal BZ, as presented in Fig. 5.2. The height of the TSL BZ along the [111] direction is inversely proportional to the height of the supercell. The yellow-shaded planes inside the BZ indicate {110} mirror planes where the nontrivial topology of the defect-free bulk crystal occurs. In an ordinary SnTe bulk, there are six such mirror planes, but due to the (111) TP, only three of them are left in the TSLs.

The cubic bulk crystal can be also represented by the hexagonal BZ instead of the fcc [1] BZ if the supercell along the [111] direction consists of a multiple of six layers. In this arrangement, the cubic and hexagonal BZs will be compatible, and the L^{fcc} points will fold at certain high symmetry points within the hexagonal BZ. However, if the number of layers is not a multiple of six, there is no compatibility between the cubic and hexagonal BZs. Consequently, finding the L^{fcc} points in the hexagonal BZ is not possible. Nonetheless, we expect that the bulk band gap region is situated for k vectors along the Γ-A and M-L lines.

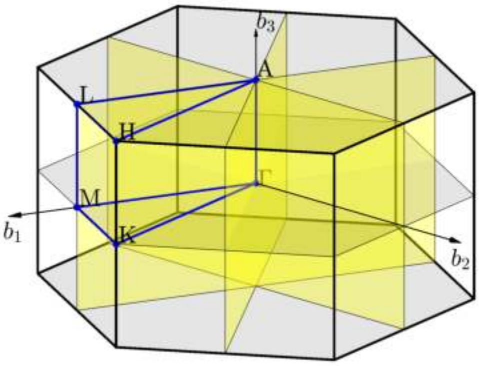

Figure 5.2: Three dimensional simple hexagonal BZ of a [111]-oriented TSLs. The yellow-shaded rectangles representing {110} mirror symmetry planes and light grey-shaded hexagons indicating (111) mirror planes.

5.1.2 Bulk properties of the TSLs

In this section we investigate the electronic band structures of TSLs with various TP settings in the supercell. Next, we will discuss the corresponding topological invariants and Berry curvatures.

---

[1] the superscript fcc is used to distinguish the point from the L points in the hexagonal BZ.

The electronic band structures are computed along high-symmetry lines indicated in Fig.5.2. In particular, Fig.5.3 displays the results of band structure calculations for a supercell with $d = 200$ atomic layers of cat-cat and an-an TSLs along the Γ-M-K-Γ path. The distance between twin planes is set to $l = 100$ monolayers in the supercell. To investigate the effect of TPs, the spectral lines are colored, with red indicating proximity to the TPs. The results show that states localized on the TPs are situated in the bulk band gap region near the M points. The hybridization between localized states at two TPs in the supercell is suppressed at a distance about $d = 200$, and increasing d further has no effect on the localized states. Since both cat-cat and an-an TSLs preserve time-reversal and inversion symmetries, all bands must have even degeneracy according to the Kramers theorem. The band edges are represented by red lines in Fig. 5.3 and are twofold degenerate in the Γ-M-K plane. The electronic band structures along the high symmetry lines in ALH plane can be found in Appendix A.1.

We use various methods to calculate the topological invariants depending on the studied cases. For TSLs with inversion symmetry, such as those with the same atomic type TP, the $\mathbb{Z}_2$ indices can be calculated using Fu and Kane's method [59, 66]. On the other hand, for TSLs without inversion symmetry, the Fukui method must be used [60].

In the case of calculating mirror Chern number (C_m) for TSLs, the Fukui method is used for all constructions [64]. This involves calculating C_m with respect to two different mirror planes, which are (111) and $(1\bar{1}0)$, with the former computed on two separate planes, i.e., ΓMK and ALH, and the latter on the plane ALΓM. It is important to note that the result for $(1\bar{1}0)$ is the same as $(01\bar{1})$ and $(\bar{1}01)$ due to the C_3 symmetry.

The calculations were performed for supercell heights $d \geq 8$ for cat-cat/an-an TSLs and $d \geq 10$ for cat-an TSLs. The resulting values of C_m and weak and strong indices $\nu_i, i = 0, 1, 2, 3$ are shown in Table 5.1 for three different TSL configurations. The weak indices ν_i characterize the topology of appropriate time-reversal invariant planes in the BZ, with ν_3 in particular describing the ALH plane.

The topological indices remain the same and do not vary with the increase of width d, except for the smallest possible width, which is four-layer height for cat-cat/an-an and six-layer height for cat-an. It is worth noting that the invariants converge at $d = 8$ or $d = 10$ in the specific simplified TB parametrization we use and this threshold value may differ for other parametrizations. However, the convergence of invariants at some d is expected to be universal. Consequently, the calculated mirror Chern number for cat-cat TPs in the supercell is $C_m^{(\Gamma\mathrm{MK})} = 4$, while for an-an TSLs, it is $C_m^{(\Gamma\mathrm{MK})} = 2$. In both cases,

TSLs	$\mathbb{Z}_2$	$C_m^{(\Gamma\mathrm{MK})}$	$C_m^{(\mathrm{ALH})}$	$C_m^{(\mathrm{AL}\Gamma M)}$
cat-cat ($d \geq 8, l \in$ even)	(0;0,0,0)	4	0	2
an-an ($d \geq 8, l \in$ even)	(0;0,0,0)	2	0	2
cat-an ($d \geq 10, l \in$ odd)	(0;0,0,1)	3	1	2

Table 5.1: The mirror Chern number C_m and $\mathbb{Z}_2$ invariants calculated for 3D TSLs grown along [111] crystallographic direction with various heights of supercells. The values of C_m are calculated at three high-symmetry planes in the Brillouin zone, as denoted by the superscripts [133]. Copyright (2023) by the American Physical Society.

the mirror Chern number for the ALH reciprocal plane is zero. On the other hand, the cat-an TSL exhibits an odd mirror Chern number on both planes: $C_m^{(\Gamma\mathrm{MK})} = 3$ and $C_m^{(\mathrm{ALH})} = 1$. Analyzing the ΓMK plane, we conclude that the mirror Chern numbers of the three TSL configurations differ, indicating that they belong to distinct topological classes.

Additionally, the $C_m^{(\mathrm{AL}\Gamma\mathrm{M})}$, corresponding to the $(1\bar{1}0)$ mirror plane is also nonzero. Consistent with the defect-free bulk crystal [7], the mirror Chern number on this plane is equal to $C_m^{(\mathrm{AL}\Gamma\mathrm{M})} = 2$. The calculated band structures on the path along high symmetry lines at ALΓM plane are provided in Figs 5.4 and 5.5 for both cat-cat and an-an, receptively. The chosen height of the supercell is $d = 200$. Again, the red-to-blue color coding indicate the localization of wavefunction near TPs. Close-up views of directions Γ-A and L-M, are presented in 5.4(b)-(c) and 5.5(b)-(c), respectively, for the case of a cat-cat and an-an supercells. The length of the BZ in [111] direction is much smaller because the corresponding reciprocal lattice vector is inversely proportional to the height of the supercell.

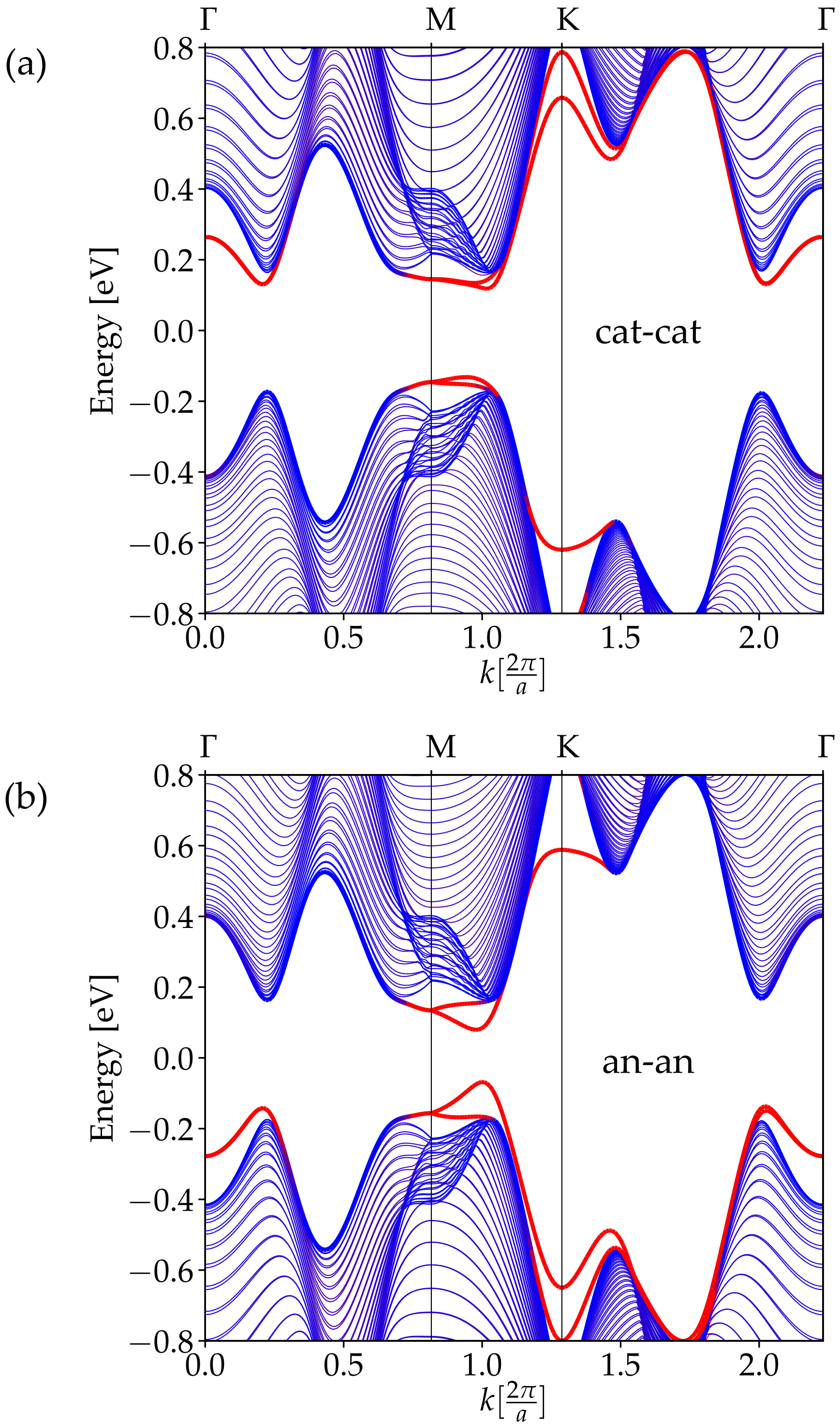

Figure 5.3: The electronic structures of SnTe TSLs with 200 atomic layers for the k wave vectors along Γ-M-K-Γ high symmetry lines of the BZ. The TSLs contain two types of TPs: (a) all-cationic TPs and (b) all-anionic TPs. The color scheme from red to blue highlights the positioning of the states at the TPs and those away from the TPs [133]. Copyright (2023) by the American Physical Society.

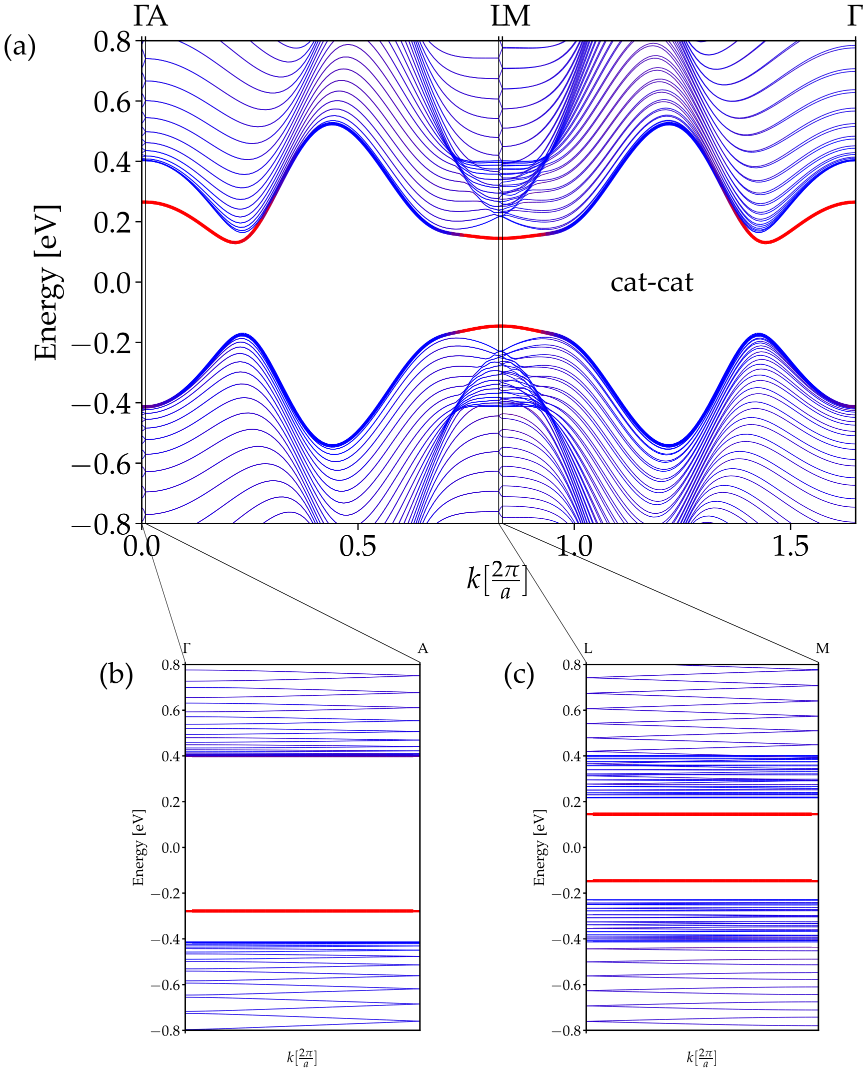

Figure 5.4: (Color online) The electronic structures of SnTe TSLs with 200 atomic layers for the k wave vectors along Γ-A-L-M-Γ high symmetry lines of the BZ. The 200 monolayer-height TSL supercell has all-cationic TPs. The red-to-blue color scheme emphasizes the localization of states in relation to the TP vicinities [133]. Copyright (2023) by the American Physical Society.

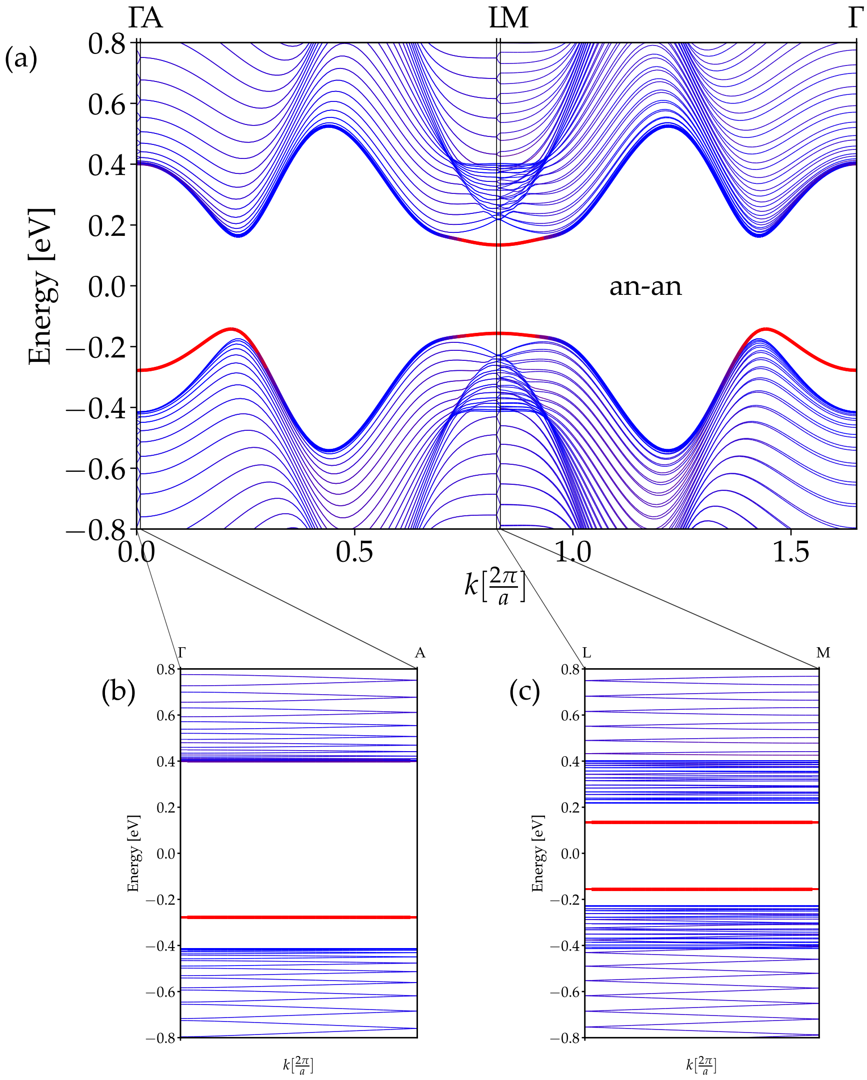

Figure 5.5: (Color online) The electronic structures of SnTe TSLs with 200 atomic layers for the k wave vectors along Γ-A-L-M-Γ high symmetry lines of the BZ. The 200 monolayer-height TSL supercell has all-anionic TPs. The red-to-blue color scheme emphasizes the localization of states in relation to the TP vicinities [133]. Copyright (2023) by the American Physical Society.

5.1.3 Berry curvature

The mirror Chern numbers have been obtained by integrating the Berry curvature over 2D cross-sections of the BZ within $+i$ mirror eigenstates. The analysis revealed that the Berry curvature in the ΓMK plane for various configurations differ from those obtained in the ALH plane. It turn out that the high intensity of the Berry curvature occurs in the vicinity of Γ, M, A, and L points in the BZ, where the band gap occurs. Consistent with our expectation the bulk band gap region is situated for k vectors along Γ-A and M-L lines. The Berry curvature for cat-cat/an-an and cat-an TSLs with $d = 16$ and $d = 18$ displayed distinct extrema near these points in the BZ.

In cat-cat TSLs, the curvature extrema were observed near both M and Γ points, as depicted in Fig.5.6(a). On the other hand, in an-an TSLs, the extrema of the Berry curvature were also observed, but their sign turned out to be negative near the Γ point, as shown in Fig.5.6(b). In the case of cat-an TSLs, the Berry curvature exhibited extrema of opposite signs around the Γ point. At the same time, uncompensated extrema were observed around the M points, as illustrated in Fig.5.6(c). Additionally, in the ALH plane, positive Berry curvature was primarily concentrated around A, while around each L point, two extrema of opposite signs were present. Notably, the high intensities of Berry curvature in Fig.5.6 were observed to be correlated with the band edges shown in Fig. 5.3 [133].

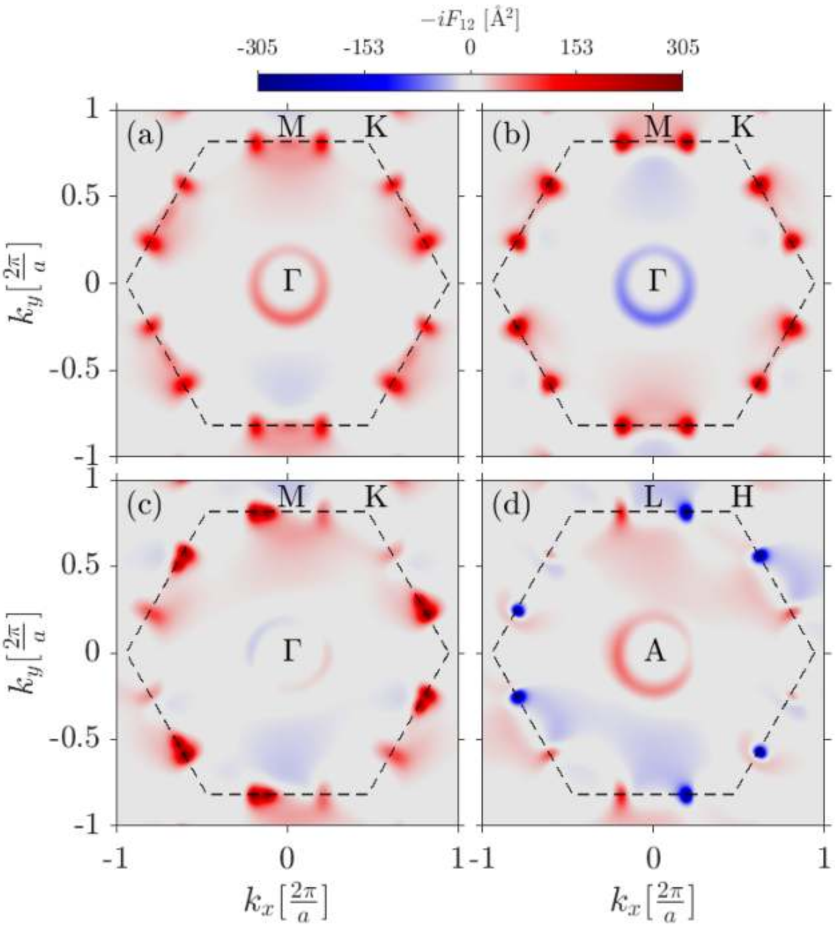

Figure 5.6: The calculation of Berry curvatures related to the $+i$ mirror subspace was performed in the ΓMK plane for two types of TSLs: (a) cat-cat and (b) an-an, both having a 16 monolayer-height supercell. Additionally, for cat-an TSLs with 18 monolayer-height supercells, the calculations were carried out in both (c) ΓMK and (d) ALH planes. The BZ boundaries are indicated by dashed lines [133]. Copyright (2023) by the American Physical Society.

In order to better understand the previously discussed phenomena, we performed a local integration of the Berry curvature in the vicinity of high-symmetry points. Specifically, we examined the Berry flux around each of the three M points and the Γ point for the various configurations. The results indicate that the calculated Berry flux around each of the three M points for all configurations is approximately 1. At the Γ point, however, the Berry flux varies depending on the TSL configuration. For cat-cat TSLs, the Berry flux is equal to 1, while for an-an TSLs, it is equal to -1. In the case of cat-an TSLs, the Berry flux at the Γ point is equal to zero.

By summing the Berry fluxes near the three M points and the Γ point, we obtain the mirror Chern numbers presented in Table 5.1. These numbers provide a quantitative measure of the topological properties of the TSLs. For example, they describe the amount of mirror symmetry protected gapless surface states that exist at the edges of the TSLs.

Intriguingly, in the ALH plane of the cat-an TSL, the Berry flux near the L points is compensated, while it amounts to 1 around the A point. To understand the difference in results between the ALH plane and the ΓMK plane, it is helpful to examine the mirror plane symmetry properties of the states in both planes. We can define the Bloch functions as Ψ_0 and Ψ_π on the $k_z = 0$ (ΓMK plane) and $k_z = \pi$ (ALH plane), respectively. Additionally, let $|\Psi_0\rangle$ and $|\Psi_\pi\rangle$ be the eigenstates of the (111) mirror plane operator. By checking the properties of these states, one can easily check that

$$\langle\Psi_0|\hat{M}_1|\Psi_0\rangle = \langle\Psi_0|\hat{M}_2|\Psi_0\rangle \tag{5.1}$$

$$\langle\Psi_\pi|\hat{M}_1|\Psi_\pi\rangle = -\langle\Psi_\pi|\hat{M}_2|\Psi_\pi\rangle, \tag{5.2}$$

where mirror plane operators $\hat{M}_1$ and $\hat{M}_2$ correspond to TP_1 and TP_2, respectively. By assuming the topological properties of TSL depend mainly on individual TPs in the unit cell, we can define independent mirror-resolved Berry curvatures $F_{12}^{\mathrm{TP}_n,\pm i}$ and Chern numbers $C_{\mathrm{TP}_n,\pm i}$ determined individually for each TP_n, where $\pm i$ denotes the eigenspace of the operator $\hat{M}_n$. The quantities defined in this way do not depend on the specific location of TP_n in the unit cell. The Chern numbers given in Table 5.1 and the curvatures shown in Fig. 5.6 are calculated with respect to the $\hat{M}_2$ operator. Thus, from equations (5.1) and (5.2) it follows that on the ΓMK plane the total Berry curvature is a sum of curvatures $F_{12}^{\mathrm{TP}_2,\pm i} + F_{12}^{\mathrm{TP}_1,\pm i}$ determined by TP_2 and TP_1. On the contrary, on the ALH plane, the total Berry curvature is given by a difference $F_{12}^{\mathrm{TP}_2,\pm i} - F_{12}^{\mathrm{TP}_1,\pm i}$. Consequently, the Chern numbers would also be the sum and difference of individual invariants: [133]

$$C_{\pm i}^{(\Gamma\mathrm{MK})} = C_{TP_1,\pm i} + C_{TP_2,\pm i}, \tag{5.3}$$

$$C_{\pm i}^{(\mathrm{ALH})} = C_{TP_2,\pm i} - C_{TP_1,\pm i}\,. \tag{5.4}$$

The underlying assumptions made for each of individual TP invariant are in a good agreement with the calculated mirror Chern numbers presented in Table 5.1. Hence, we expect that a cationic TP has mirrir Chern number $C_{cTP,m} = 2$ while an anionic TP has $C_{aTP,m} = 1$. We will confirm this by calculating the topological properties of slabs, as described in Section 5.2.

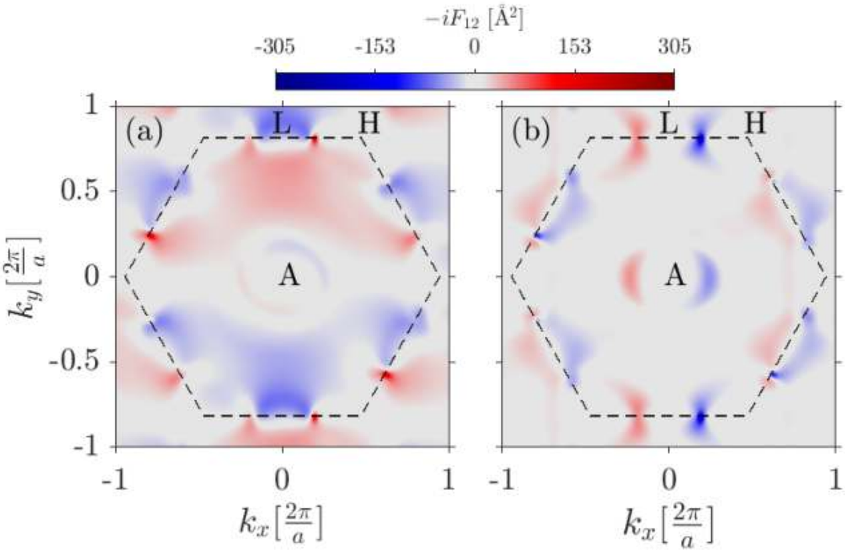

Figure 5.7: Figures (a) and (b) depict the Berry curvatures linked to the $+i$ mirror subspace in the ALH plane of the 2D BZ for cat-cat and an-an TSLs with 16 monolayer-height supercells, respectively [133]. Copyright (2023) by the American Physical Society.

5.1.4 Surface states in twinning superlattices

In this section, we present the semi-infinite surface spectral Green function of TSLs along $(1\bar{1}0)$ and $(11\bar{2})$ faces. The surface Brillouin zones (SBZ) corresponding to these orientations are depicted in light green in Fig. 5.8. In 3D BZ the L (M) points projected onto the 2D SBZ in pairs for both cases, e.g., $\mathrm{L}_1, \mathrm{L}_2 \rightarrow \overline{\mathrm{L}}$ $(\mathrm{M}_1, \mathrm{M}_2 \rightarrow \overline{\mathrm{M}})$. In addition, L_3 (M_3) is projected together with A (Γ) onto $\overline{\mathrm{A}}$ ($\overline{\Gamma}$). It is worth mentioning that $(11\bar{2})$ surface maintains one of the $\{110\}$ mirror planes, while the $(1\bar{1}0)$ surface breaks all of them. The (111) mirror plane is conserved by both surface terminations.

The surface spectral functions are computed along $(1\bar{1}0)$ for various types of TPs configurations in Fig. 5.9. For cat-cat and an-an TPs, the supercell height used is $d = 16$, while for TSLs with alternating TPs, it is $d = 18$. The number of surface states is determined by the (111) mirror Chern number C_m, and the location of the Dirac cone can be identified by examining the extrema in Berry curvature calculations. The results of the

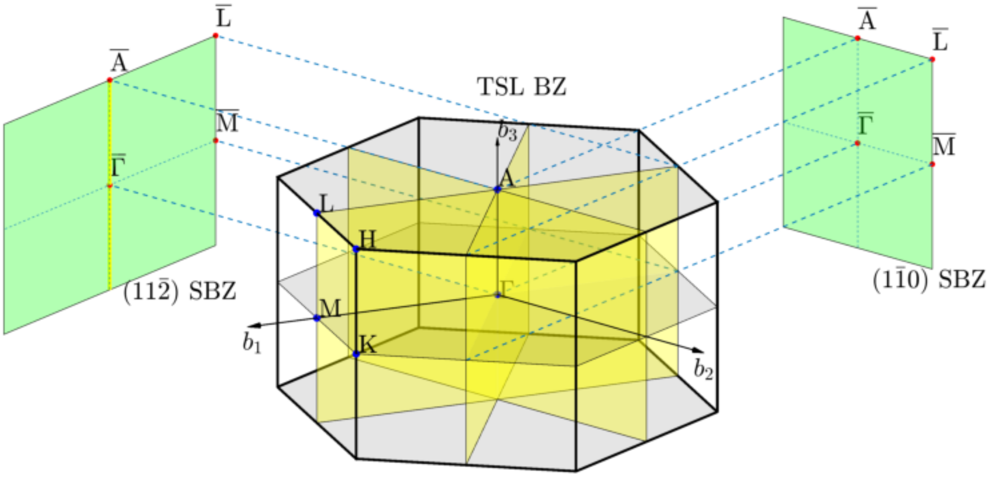

Figure 5.8: The Surface BZ of TSL along $(11\bar{2})$ and $(1\bar{1}0)$ directions. A one mirror symmetry belonging to the $\{110\}$ family is maintained within the $(11\bar{2})$ SBZ, while all corresponding planes are broken within the $(1\bar{1}0)$ SBZ.

analysis indicate the presence of two double Dirac cones, separated in energy at $\overline{\mathrm{M}}$ due to valley mixing[2] within the band gap. The spectral function for cat-cat TSL [Fig.5.9(a)] includes a similar structure near $\overline{\Gamma}$, with secondary Dirac points shifted towards $\overline{\mathrm{M}}$. On the other hand, the spectral function of an-an TSL [Fig.5.9(b)] shows a gap in the vicinity of $\overline{\Gamma}$. In the cat-an TSL [Fig. 5.9(c)], a single topologically protected Dirac point appears exactly at $\overline{\Gamma}$ and at $\overline{\mathrm{A}}$.

In a similar fashion, the spectral function was computed for a $(11\bar{2})$ surface, as illustrated in Fig. 5.10. The obtained results are qualitatively similar to those obtained for the $(1\bar{1}0)$ surface, except for the $\overline{\Gamma}$-$\overline{\mathrm{A}}$ line. This difference arises because the $(1\bar{1}0)$ mirror symmetry is not broken by the $(11\bar{2})$ surface termination. Consequently, a gapless surface state is also observed along this direction.It is noteworthy mentioning that the emergence of this surface state is protected by the TCI bulk and is not related to the presence of TP.

It is worth emphasizing that the occurrence or non-occurrence of Dirac crossings along $\overline{\Gamma}$-$\overline{\mathrm{M}}$ for both surface orientations can be elucidated by analyzing the Berry curvatures displayed in Fig. 5.6. Specifically, in an-an TSLs, the local extrema of Berry curvature at $\overline{\Gamma}$ and $\overline{\mathrm{M}}$ points possess opposite signs, thereby precluding the formation of a Dirac cone on the surface BZ. On the contrary, in cat-cat TSL, both the Γ and M valleys exhibit matching contributions (signs) with the appearance of two surface Dirac cones located at $\overline{\Gamma}$. Conversely, the vicinity of Γ in cat-an TSL is deemed topologically trivial, causing only one surface Dirac cone to be generated exclusively by the M valley.

---

[2] valley mixing is an interference between states coming from the two valleys projecting onto the same area in the surface BZ.

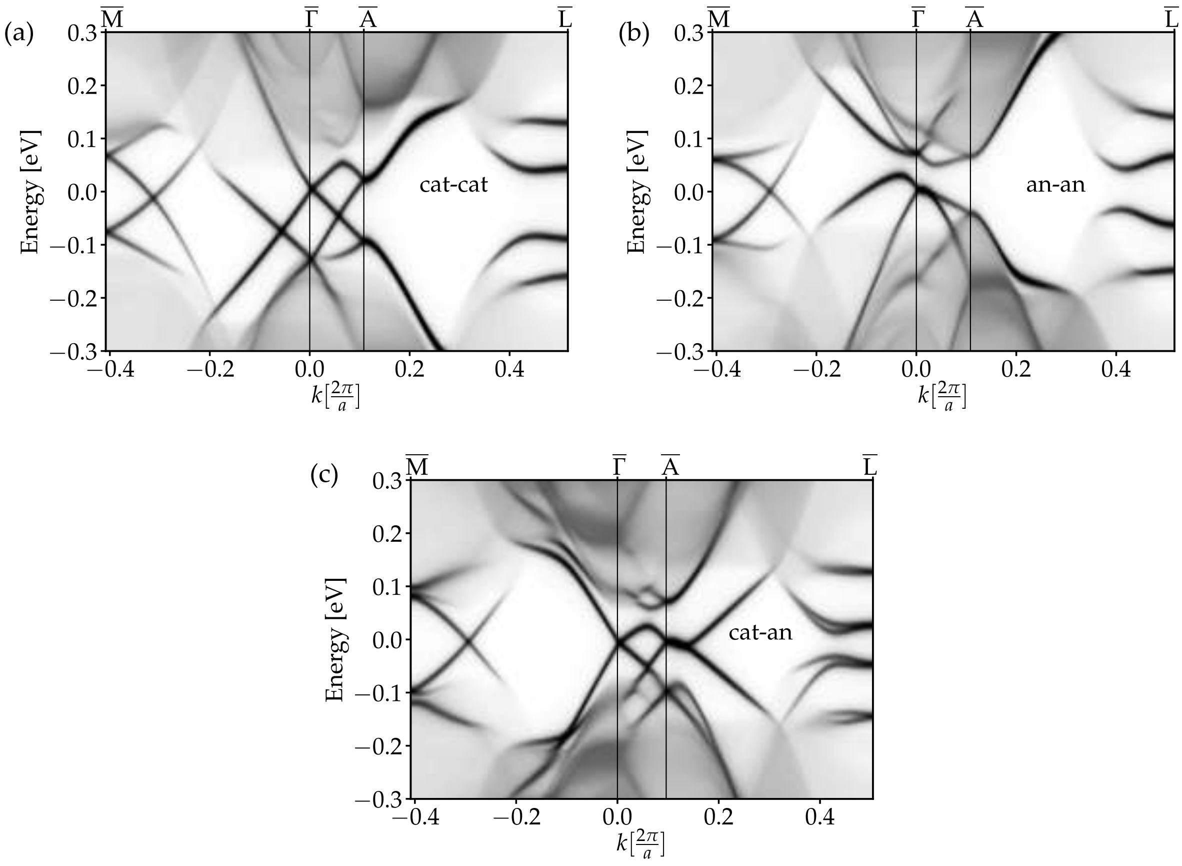

Figure 5.9: The surface spectral functions of SnTe TSL calculated for the $(1\bar{1}0)$ surface orientation. The spectra were obtained for both cationic TPs (a) and both anionic TPs (b) for a supercell height of $d = 16$. Additionally, panel (c) shows the spectra for the supercell with a height of $d = 18$, which includes one anionic and one cationic TP type [133]. Copyright (2023) by the American Physical Society.

Analogous observations can also be extended to the spectra along $\overline{\text{A}}$-$\overline{\text{L}}$, where the existence of a single Dirac point is only observed in the cat-an case. This Dirac point is found to be located at the $\overline{\text{A}}$ point, which is consistent with nontrivial curvature around A, and the weak $\mathbb{Z}_2$ and mirror Chern numbers for the ALH plane.

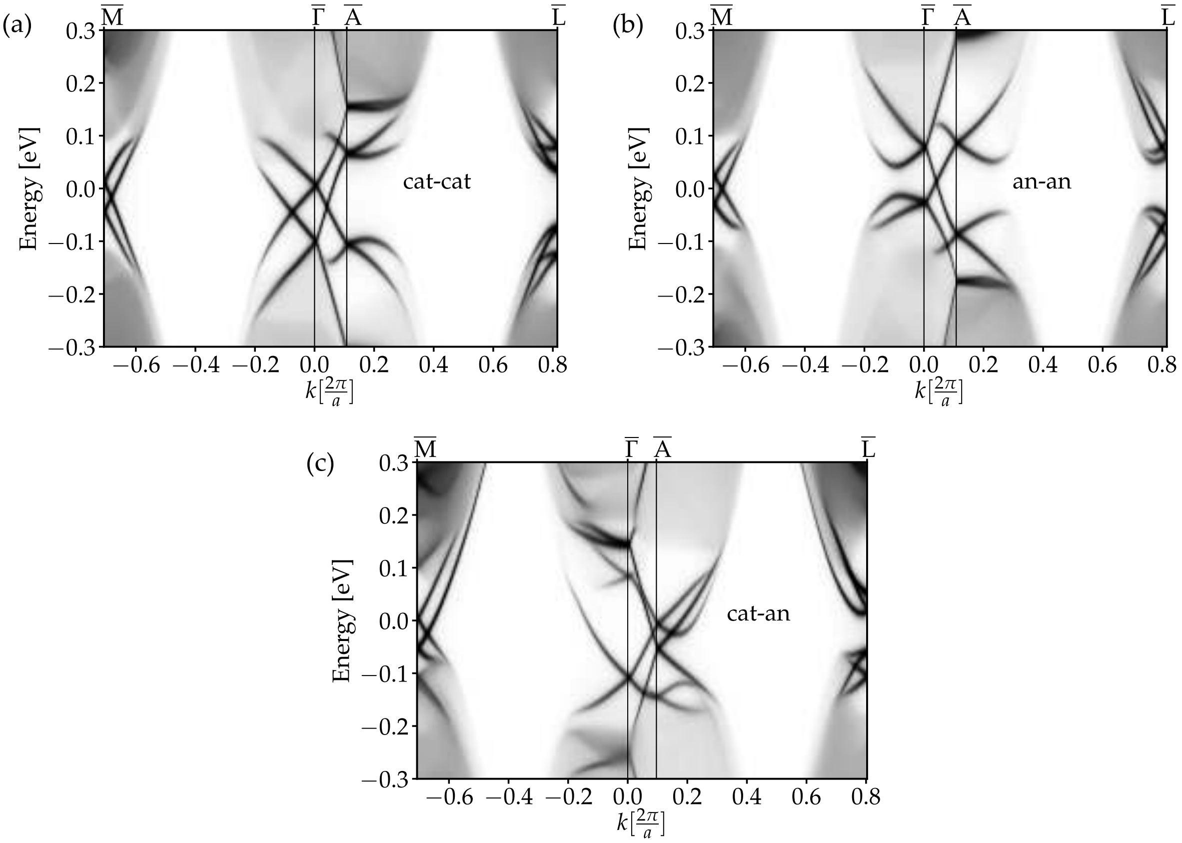

Figure 5.10: The surface spectral functions of SnTe TSL calculated for the $(11\bar{2})$ surface orientation. The spectra were obtained for both cationic TPs (a) and both anionic TPs (b) for a supercell height of $d = 16$. Additionally, panel (c) shows the spectra for the supercell with a height of $d = 18$, which includes one anionic and one cationic TP type. The protected Dirac crossing is also visible along $\overline{\Gamma}$-$\overline{\text{A}}$ direction for all cases [133]. Copyright (2023) by the American Physical Society.

5.2 (111)-oriented slab with a single twin plane

In the preceding section, the assumption made for the topological properties of an individual TP has been validated by the calculated mirror Chern numbers displayed in Table 5.1. However, in order to ascertain the specific role of each TP, we delve deeper into the matter by investigating a real system that possesses a single TP. To this end, we consider a twinned SnTe slab featuring a solitary (111) twin boundary in the middle of the structure. Given that the lattice exhibits local mirror symmetry with respect to the TP, we opt to study a finite system that exhibits global (111) mirror symmetry (as depicted in

Fig. 5.11). Our analysis is focused on the configuration of a (111)-oriented slab, wherein either a cationic or an anionic TP is positioned at the center. The pristine gapless surface states of the (111) slab are protected by a $\{110\}$ mirror symmetry. In order to investigate the topological properties of the system, it is necessary to introduce a gap into the system. This enables to study the distinct topological properties associated with each individual TP.

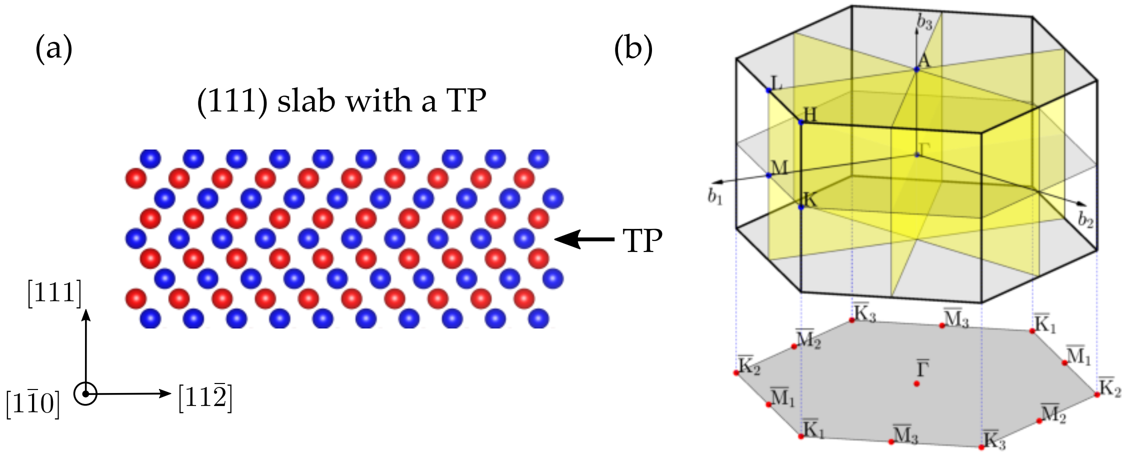

Figure 5.11: Panel (a) shows the (111) slab structure with a TP located in the middle. Panel (b) displays the corresponding 2D BZ of the (111) surface of TSL.

5.2.1 Slab with unperturbed surfaces

The band structures of the (111) slab exhibit four surface Dirac cones in the 2D BZ. One cone is situated at the $\overline{\Gamma}$ point, while the other three are found at the $\overline{\mathrm{M}}$ points. This characteristic (the appearance of Dirac cones) remains unaltered in the event of the existence of a TP, provided that (each) surface and TP are situated at a considerable distance. The computed spectra of the slabs for both types of TPs are depicted in Fig. 5.12. For the purpose of enhancing clarity, we applied a positive (negative) onsite potential shift to the outermost layers of the cationic (anionic) slab surfaces. This shift resulted in the relocation of the surface Dirac point to the center of the spectrum. However, This modification is inconsequential to the essence of our investigation.

The edge spectral functions, were computed for a slab with a thickness of 121 atomic layers, along the $[11\bar{2}]$ crystal direction with a $(1\bar{1}0)$ face of the TSL. The resulting spectral function map was color-coded to differentiate between the $+i$ (blue) and $-i$ (red) mirror reflection eigenspaces. When a cationic TP is located at the center of the slab, two (111) mirror protected edge modes are observable, one at $\overline{\overline{\mathrm{M}}}$ and the other at $\overline{\overline{\Gamma}}$ point, as depicted in Fig.5.13(a). However, in the case of an anionic TP, only a single pair of protected

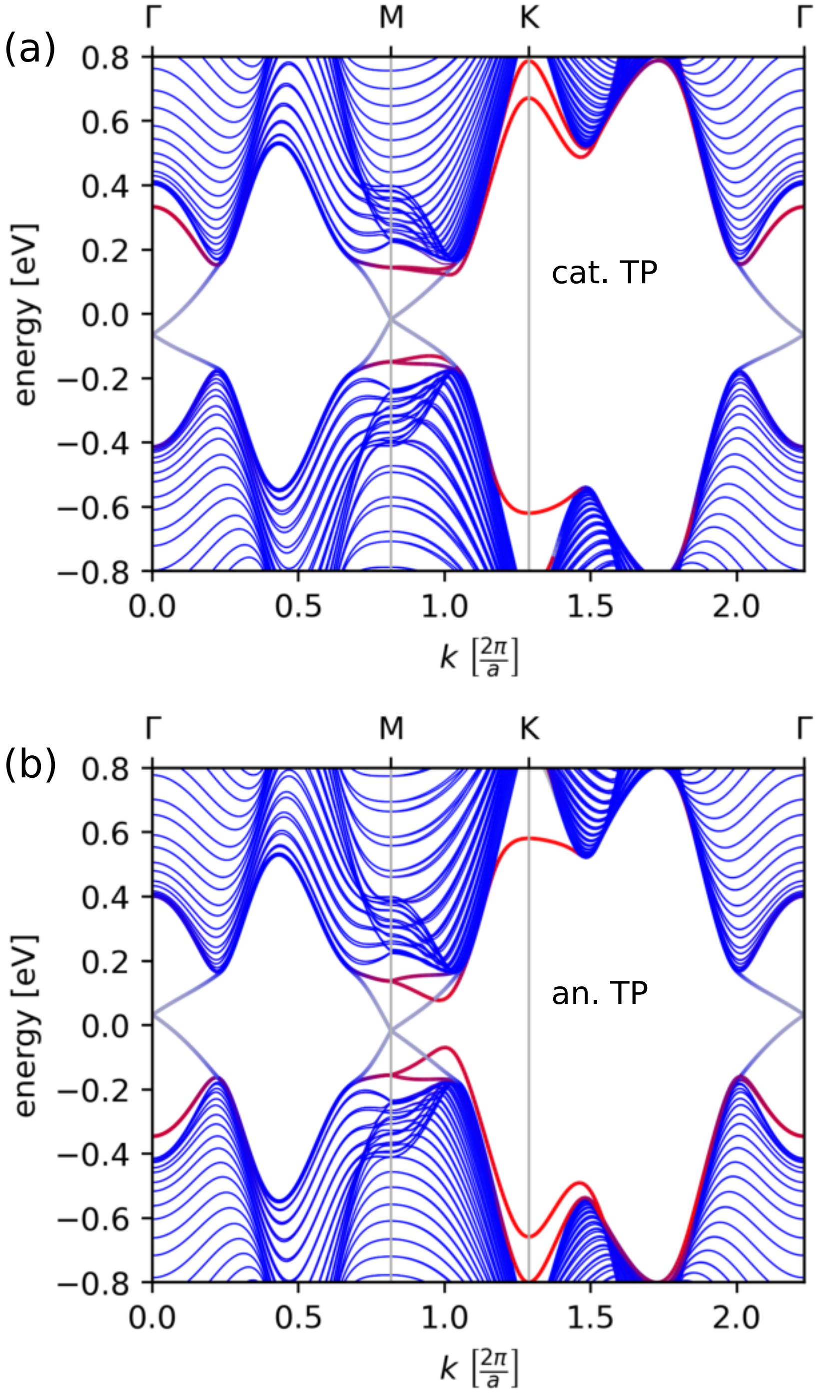

Figure 5.12: Displayed in panels are the band structures of SnTe slabs with a TP for 121 atomic layers (∼21.8 nm thick). Panel (a) contains a cationic TP in the middle, whereas panel (b) exhibits an anionic TP. The addition of positive (negative) onsite potential to the top and bottom layer surfaces is added for cationic (anionic) terminations in panel (a) [(b)]. The line color in the band structures represents the weight distribution of the wave function, where red signifies a predominant location near the TP, grey corresponds to proximity to the surfaces, and blue indicates the intermediate space [133]. Copyright (2023) by the American Physical Society.

edge mode is present at the $\overline{\overline{\Gamma}}$ point, as shown in Fig.5.13(d). Observations reveal that the wave functions, at the $\overline{\overline{\Gamma}}$ point, are predominantly confined in the [111] direction close to the cationic TP [as illustrated in Fig.5.13(b)], and are absent in the case of anionic TP [as depicted in Fig.5.13(e)]. In contrast, the crossing of edge modes near $\overline{\overline{M}}$ point occurs precisely at the same energy as the (111) surface Dirac point, which corresponds to the $\overline{\mathrm{M}}_1$ and $\overline{\mathrm{M}}_3$ points in the slab's BZ. This characteristic is observed in both types of TPs within (111) slabs. Simultaneously, there is a shift in the localization of the edge state wave functions, transitioning from tightly confined states at the TP to states in close proximity to the surfaces as k approaches the $\overline{\overline{\mathrm{M}}}$ point [compare with Figs.5.13(c),(f)].

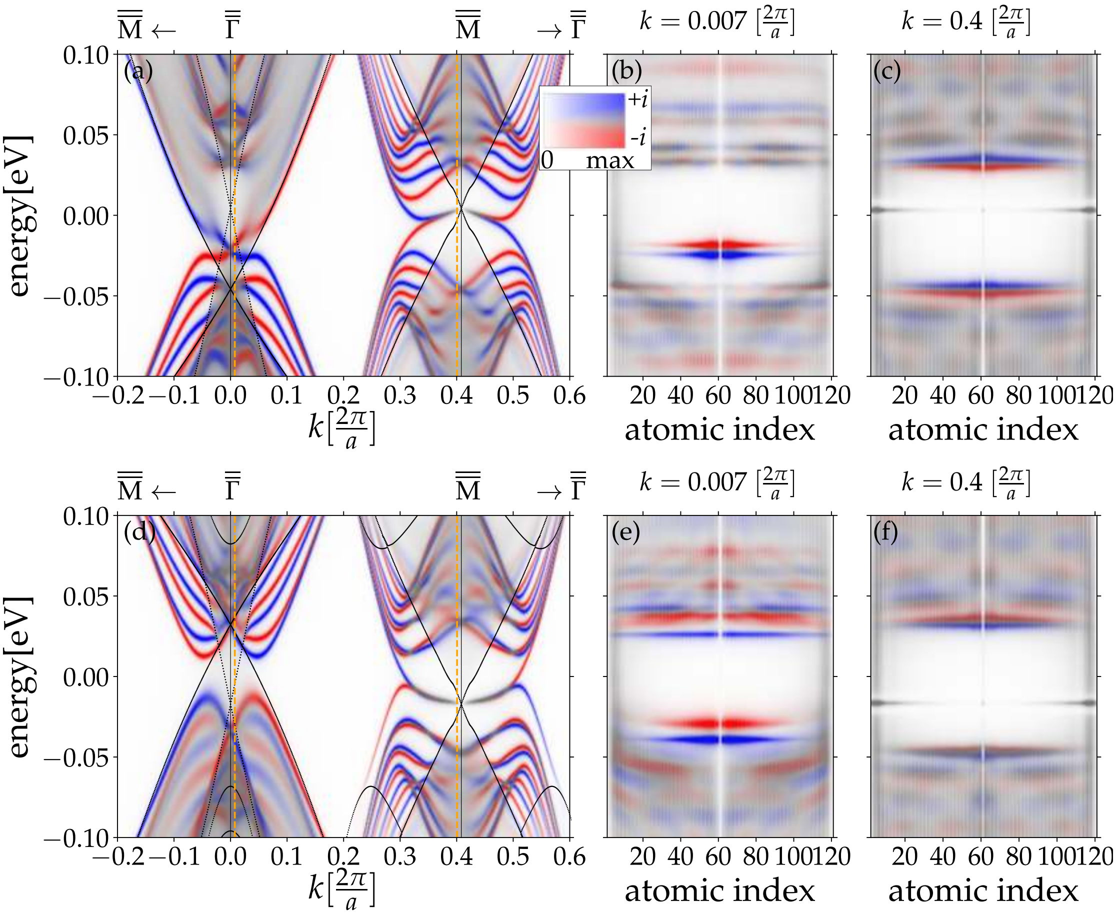

Figure 5.13: Edge spectral Green function analysis of a 121-layer-thick (111) SnTe slab with a TP, along [11$\bar{2}$] edge BZ. Panels (a) and (b) show cation- and anion-terminated slabs, respectively, with cationic and anionic TP. The spectral weight distribution across the edge is shown in panels (b)-(c) and (e)-(f) for different k values, marked by vertical orange dashed lines in panels (a) and (d) for cationic and anionic TP, respectively. The black dotted lines depict the outlines of the 2D slab bands projected to the edge, while the mirror-separated spectral functions of the subspaces $+i$ and $-i$ are represented in blue and red, respectively [133]. Copyright (2023) by the American Physical Society.

5.2.2 Slabs with gapped surface states

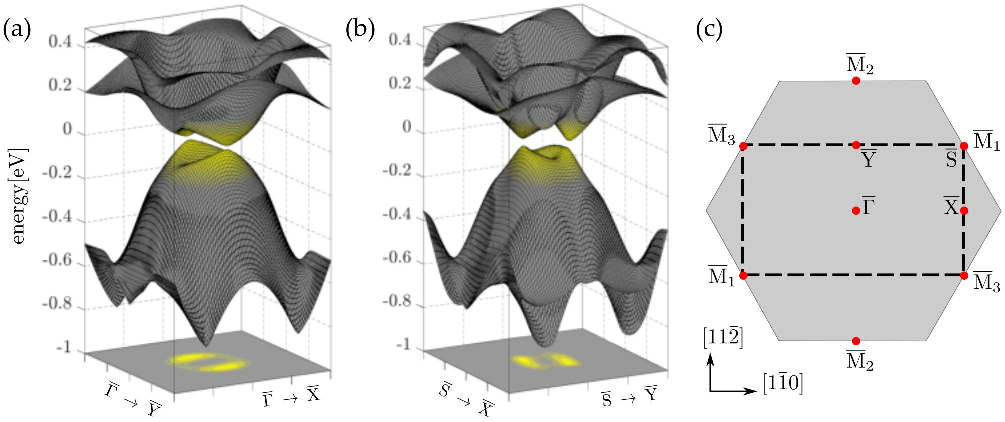

Figure 5.14: The 3D band structures of a SnTe slab with a TP and anionic terminations, showing a gap near the (a) $\overline{\Gamma}$ and (b) $\overline{S}$ points. The slab consists of 83 atomic layers, and the black dashed lines in (c) denote the folded BZ inside the primary hexagonal BZ.

Because we focus on the characteristics of the TP, it is deemed appropriate to induce a surface gap by adding perturbations to both surfaces of the slab. We choose non-magnetic perturbations which can be achieved by introducing valley-mixing in the supercell. Considering that the surface states are non-degenerate and located at four distinct points within the hexagonal 2D BZ, duplicating the primitive supercell in the $[01\bar{1}]$ direction is an acceptable approach. This results in the original valleys (in hexagonal BZ), consisting of three $\overline{\mathrm{M}}$ points and one $\overline{\Gamma}$ point, being folded into two distinct pairs in the new BZ, as depicted in Fig. 5.14(c). However, in order to allow them to interact, we need to break all three $(1\bar{1}0)$, $(0\bar{1}1)$ and $(10\bar{1})$ mirror symmetries on both surfaces (last layer at the bottom and top). This can be achieved by adjusting the TB parameters of the atomic surfaces, which reduces the translational symmetry of the lattice and facilitates valley coupling within each respective pair.

We show the 3D electronic structures of the slabs with a cationic TP in Fig. 5.14(a)-(b). The slabs possess gapped surface states ($E_g = 19$ meV) in the proximity of the $\overline{\Gamma}$ and $\overline{\mathrm{S}}$ points, respectively. The surface bands exhibit a comparable gap for an anionic TP slabs. Next, we proceed to determine the mirror Chern numbers for each cationic and anionic TP slabs. Our findings indicate a value of $C_m = 2$ for the cationic TP and $C_m = 1$ for the anionic TP, aligning with the values derived from the Chern numbers of TSLs.

Upon decoupling the impact of the surface Dirac modes of the slab from the TP, we proceed to calculate the edge spectral density of semi-infinite (111) slabs. Our analysis reveals that the gapless Dirac crossings disperse in a qualitatively comparable fashion for both gapped and gapless surface slabs at the $\overline{\overline{\Gamma}}$ point [compare Figs.5.13(a) and 5.15(a)].

However, the edge modes at the $\overline{\overline{\mathrm{M}}}$ point cross at a different energy compared to the previous case. For both types of slabs, the edge states' wave functions in close proximity to $\overline{\overline{\mathrm{M}}}$ extend further away from the TP [see Figs.5.15(c),(f)].

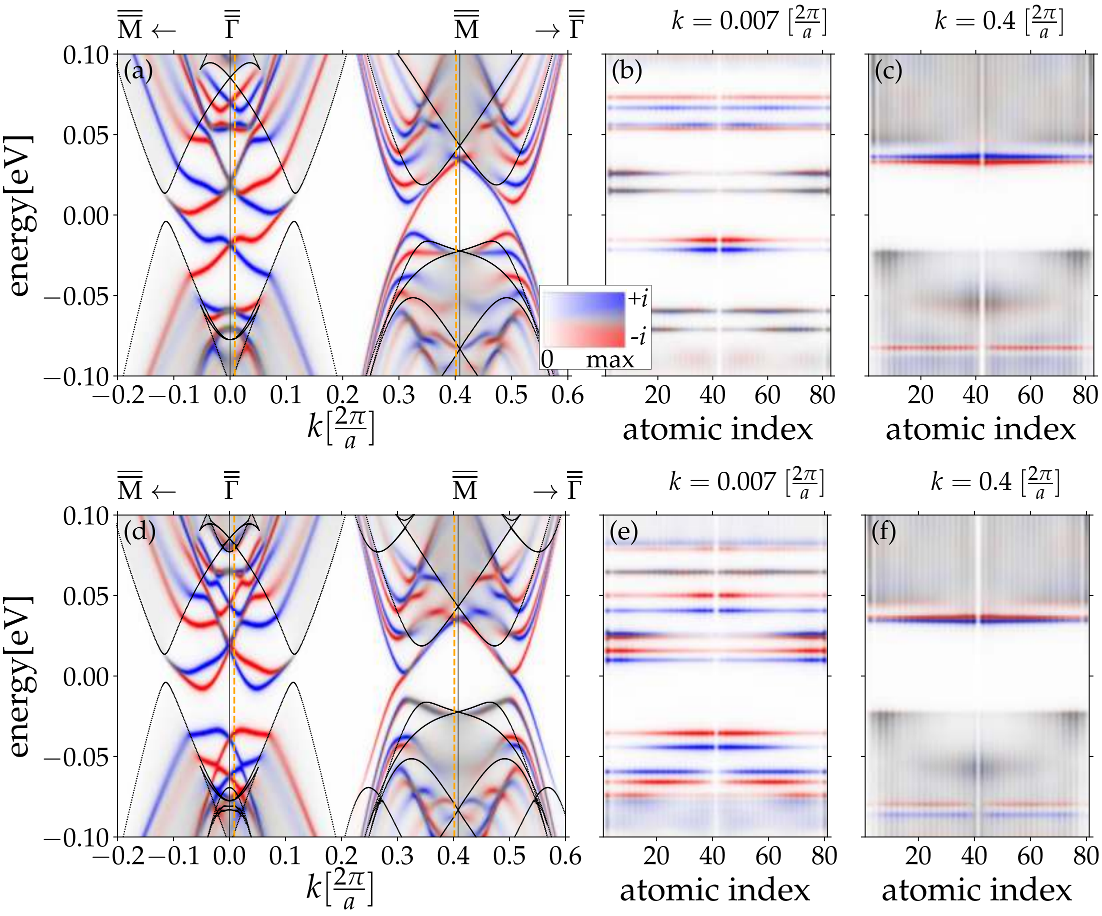

Figure 5.15: The edge spectral function of a SnTe slab with a TP, along its $[11\bar{2}]$ edge is shown with cationic and anionic TPs in panels (a) and (d), respectively. The slabs feature gap surfaces and have 83 and 81 atomic layer heights for cationic and anionic TPs, respectively, and both supercells are terminated with anionic-type atoms. The sizes are doubled along the $[01\bar{1}]$ direction for both cases. Panels (b)-(c) and (e)-(f) depict the spectral weight distribution across the edge for different k values that are indicated by vertical orange dashed lines in panels (a) and (d), respectively. Black dotted lines indicate outlines of 2D slab bands projected to the edge. Mirror-separated spectral functions of subspaces $+i$ and $-i$ are shown in blue and red, respectively.

5.2.3 Band topology of individual TPs

The objective of this section is to examine the impact of Berry curvature contributions onto the twin planes. Rafał Rechciński as a collaborator of this project, has explored and implemented two methodologies in this research [133]. The main outcome of this analysis is presented here, while further information can be found in Ref. [133].

It is possible to introduce a gap in the Dirac cones located at the surfaces of a slab material through the inclusion of a small Zeeman term $H_Z = m\sigma_z$ directed along the $[111]$ axis—the same Zeeman term acting on two surfaces only at last atomic layer. Here, m represents the strength of the term, and σ_z refers to the third Pauli matrix operating within the spin subspace. Adding a Zeeman term breaks time-reversal symmetry, but preserves the (111) mirror plane, simulating a weak magnetic field on both surfaces. This may result in new topological features and edge states. Nevertheless, we can still examine the Berry curvature and calculate the Chern number of the topological phase in the slab using this method.

We define mirror Berry curvature $F_{12}^{m} = (F_{12}^{+i} - F_{12}^{-i})/2$, where $\pm i$ denotes eigenspace of the (111) mirror reflection operator. Due to invariance of the Berry curvature to a k-independent unitary transformation, the Berry curvatures of the two surfaces are equal, $F_{12}^{\text{top surf.}} = F_{12}^{\text{bottom surf.}}$. It is noted that the Zeeman terms on the surfaces affect the total Chern number C through the total Berry curvature $F_{12} = F_{12}^{+i} + F_{12}^{-i}$, while the mirror Berry curvature F_{12}^{m} contains information only on the TP and the surrounding twin lattice. In Fig. 5.16 the mirror Berry curvature maps of a cationic and an anionic twin boundary are shown. The mirror Berry fluxes around $\overline{\text{M}}$ and $\overline{\Gamma}$ points are fractional ($\pm\frac{1}{2}$) and eventually lead to mirror Chern numbers $C_m = 2$ and $C_m = 1$, for cationic and anionic TP, respectively.

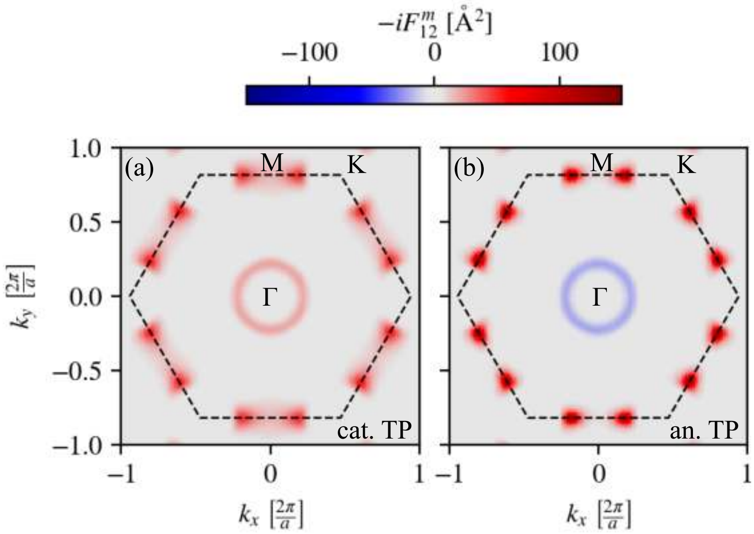

Figure 5.16: Mirror Berry curvatures of (111)-oriented SnTe slabs with (a) a cationic and (b) an anionic TP in the center. The dashed lines indicate the first BZ boundaries. To open the gap in the surface spectrum, a Zeeman term is applied to the outermost layers [133]. Copyright (2023) by the American Physical Society.

Next, we begin with investigating of topology of a single TP by introducing the projected Berry curvature as

$$F_{12}^{(A)}(k) = Tr[\mathcal{F}(k)P_A], \tag{5.5}$$

where $\mathcal{F}(k)$ is the Kubo formula for the Berry curvature [133] and P_A is a projection operator corresponding to a selected part (labeled A) of the slab unit cell. The Berry curvature of the slab can be split into three parts $F_{12} = F_{12}^{\text{TP}} + F_{12}^{\text{surf.}} + F_{12}^{\text{bulk}}$, where the subsequent addends arise from the presence of the TP, the surfaces, and the intermediate lattice, respectively.

We calculated $F_{12}^{\text{TP},\pm i}$ for two slabs with magnetic term $m = 0.5\,\text{eV}$ added on surfaces. By examining $F_{12}^{(A)}$ for various parts of the slab, we determined that the subsystem T shown in [Fig. 5.17(e)] should contain at least 41 layers in the middle of the slab, while B can be any two adjoining atomic layers (one cationic and one anionic), located more than 20 layers away from the TP and 24 layers away from the surface, along with two atomic layers being their mirror reflection on the other side of the TP. Figure 5.17 shows the calculated TP Berry curvatures for the cationic and anionic TP in the $\pm i$ subspace.

The Chern numbers of $\pm i$ subspace can be expressed as the sum of components obtained by integrating F_{12} over TP, bulk, and surface regions. Numerical evaluation yields $C_{\text{cat. TP}}^{\pm i} \approx \pm 2$ and $C_{\text{an. TP}}^{\pm i} \approx \pm 1$, with $C_{\text{bulk}}^{\pm i} \approx 0$. This enables us to confirm that mirror Chern number to the TPs: $C_{\text{cat. TP}}^{m} = 2$ for cationic TP and $C_{\text{an. TP}}^{m} = 1$ for anionic TP. Through local integration of the field surrounding each $\overline{\text{M}}$ point and the $\overline{\Gamma}$ point, it is evident that the Berry flux associated with these points is fractional. However, as detailed in Appendix A.2, the projected points of these valleys onto the edge BZ always occur in pairs. Consequently, the Berry fluxes corresponding to $\overline{\text{M}_\text{i}}$ and $\overline{\Gamma}$ points in the projection line are always integers.

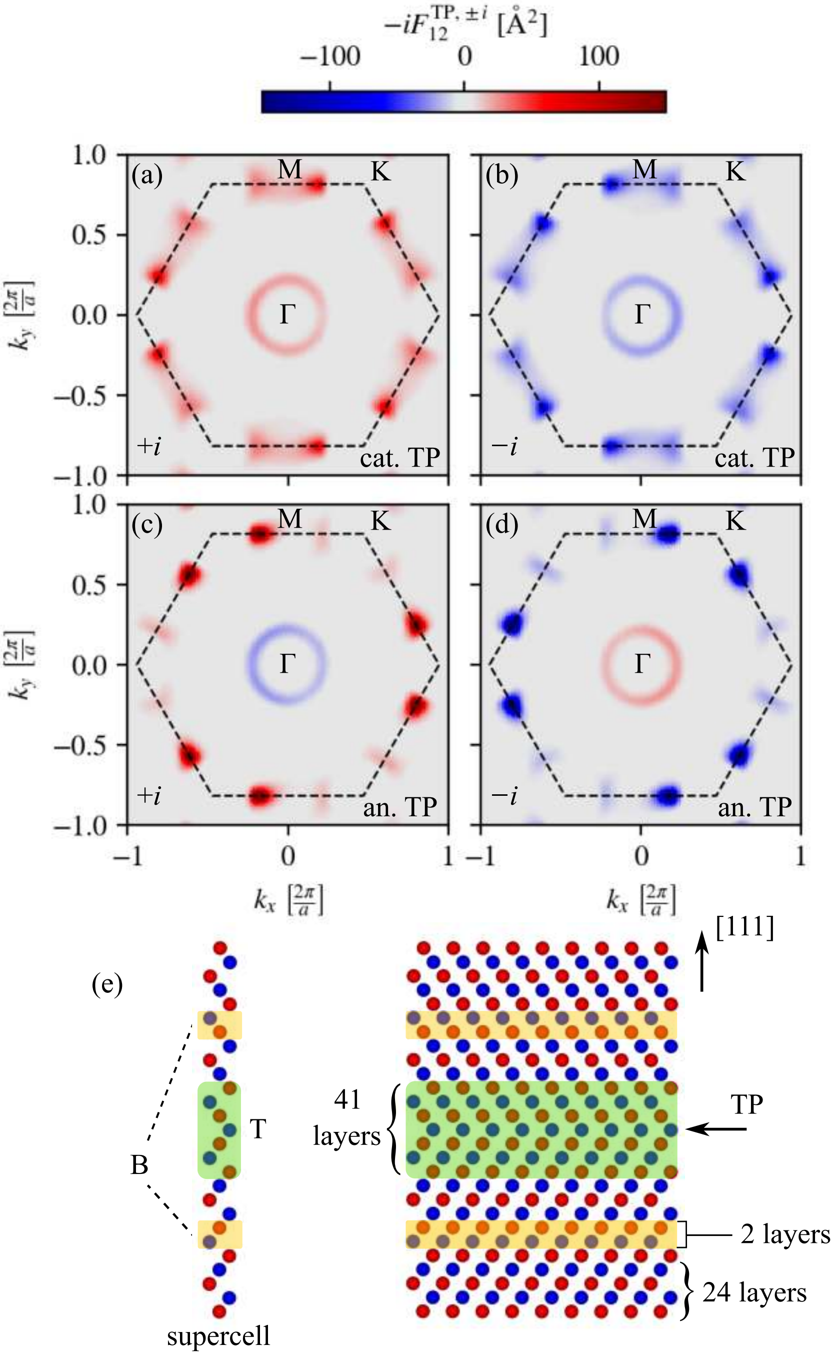

Figure 5.17: The Berry curvature projections of a 121-monolayer thick, (111)-oriented slab with cationic TP (a,b) and anionic TP (c,d) within $\pm i$ mirror subspaces. The sketch (e) illustrates the subsystems T and B used in the projected Berry curvature calculations for the (111)-oriented slab [133]. Copyright (2023) by the American Physical Society.

5.3 Quantum spin Hall effect in (111)-oriented film in the presence of a TP

The quantum spin Hall (QSH) insulator, known as a 2D TI, is characterized by metallic edge states that are protected by time-reversal symmetry. These edge states exist in Kramers doublets and exhibit a helical nature where two states with opposite spin-polarizations propagate in opposite directions at a given edge. Due to the protection provided by time-reversal symmetry, these spin-polarized channels are immune to backscattering and can flow without dissipation. This unique feature makes QSH state and TIs, in general, highly attractive for spintronic device applications that require low power consumption and enable reversible quantum computations [55].

Extensive research has been carried out to identify 2D systems that exhibit topologically non-trivial edge states. For instance, the HgTe/HgCdTe quantum well in certain thicknesses and hybridized InAs/GaSb quantum wells have been experimentally demonstrated to display QSH behavior [55, 139]. Moreover, theoretical studies suggest that 2D transition metal dichalcogenides of the form MX_2 (M=(W,Mo) and X=(Te,Se,S)) should constitute a new class of large-gap QSH insulators [140].

Finally, the QSH phase has been theoretically predicted to emerge in IV-VI semiconductor-based thin films grown along the [111] crystallographic direction within a certain range of thicknesses in the TCI regime. For instance, in SnTe, the energy gap changes sign and oscillates as the number of layers increases due to intersurface hybridization, leading to the formation of a 2D TI phase that is classified by a $\mathbb{Z}_2$ invariant and is protected by time-reversal symmetry [11, 12]. The reason behind this phenomenon is that the four L-point projections (in the face-centered cubic BZ) onto the 2D BZ of a (111)-oriented thin film are not equivalent. While the energy structures at the three $\overline{\mathrm{M}}$ projections are symmetric, the energy structure at the fourth projection at the $\overline{\Gamma}$ point is distinct, making it possible for band inversion to occur at an odd number (either one or three) of points in the 2D Brillouin zone [11].

In Sections 5.1 and 5.2, we have demonstrated that a 2D TCI can be defined by both cationic and anionic TPs, exhibiting mirror Chern numbers of $C_m = 2$ and $C_m = 1$, respectively. Here, we extend our topological exploration to (111)-oriented SnTe thin films with a TP located in the middle of the structure. Our objective is to broaden our investigation to the effect of TP topology in a system with a natural gapped surface states due to finite-size effects. We shall study the evolution of topological invariants with increasing film thickness and compare them with the previously studied films without TP. To achieve this, we consider a more realistic tight-binding model for the SnTe compound with *spd* orbitals.

5.3.1 Oscillation of the energy gap

QSH is observed in both even and odd atomic layer height of (111)-SnTe films in the absence of a TP. This is described by a $\mathbb{Z}_2$ invariant, denoted as ν, where $\nu = 0$ represents a trivial system and $\nu = 1$ represents a QSH phase. In odd-layer films possessing inversion symmetry, the $\mathbb{Z}_2$ invariant can be obtained through the parity of the occupied bands' eigenstates at four time-reversal momenta points in the BZ, as described by Fu and Kane [59]. On the other hand, for even-layer films without inversion symmetry, the Fukui method can be employed, as per Fukui's paper [60].

In the current study, we focus on the (111)-oriented thin films, which feature a single TP positioned in the middle of the structure. Our analysis is limited to the odd-layer configurations, and a comparison is made with those without TP. Thus, we begin by referring to the analysis of energy gap oscillation in odd-layer films without TP, as demonstrated in Ref. [11]. The corresponding results are illustrated in Fig. 5.18 for (a) cation terminated slabs and (b) for anion-terminated slabs. For the both (cation-terminated/anion-terminated) films, the obtained charts show that the energy gap at the $\overline{\mathrm{M}}$ point decreases consistently with an increase in film thickness. However, at $\overline{\Gamma}$, the energy gap changes sign and oscillates with increasing the number of layers due to intersurface hybridization, which subsequently causes oscillations in the $\mathbb{Z}_2$ invariant. When $\nu = 1$, it suggests the existence of a spin-polarized gapless edge state at $\overline{\overline{\Gamma}}$ point of the 1D edge, which is protected by time-reversal symmetry.[3]

In contrast to conventional (111)-oriented SnTe films, the presence of a TP allows for the calculation of the (111) mirror Chern number, in addition to the $\mathbb{Z}_2$ invariant. In our previous work [133], we demonstrated that both cationic and anionic TPs result in a 2D TCI with mirror Chern numbers of $C_m = 2$ and $C_m = 1$, respectively. As such, we will now show how TP topology, in conjunction with finite-size effects, can affect the oscillatory behavior of the topological phase in (111)-oriented SnTe films as the film thickness increases. Additionally, films with odd-layer thickness exhibit inversion symmetry, allowing us to employ the Fu-Kane [59] formula for the calculation of $\mathbb{Z}_2$ invariant.

---

[3] Here, we adopted the same notation as in the previous section for the (111) slab of the 1D edge., i.e., In the hexagonal BZ, the projection of the points $\overline{\Gamma}$ and $\overline{\mathrm{M}}_1$ onto the $[11\bar{2}]$ or $[1\bar{1}0]$ edge is represented as $\overline{\overline{\Gamma}}$, while the other two points, $\overline{\mathrm{M}}_2$ and $\overline{\mathrm{M}}_3$, are projected onto $\overline{\overline{\mathrm{M}}}$.

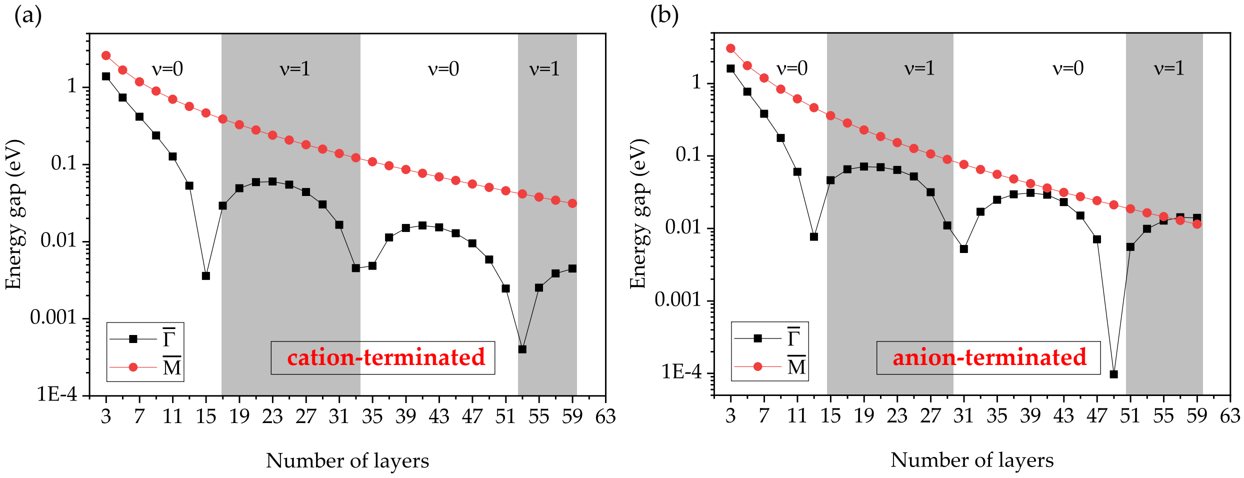

Figure 5.18: Energy gaps in (111)-oriented films with an odd number of monolayers. The gray shadowed zones show the thicknesses where the value $\nu = 1$ has been obtained. The figure recalculated form the same TB parameters given in Ref. [11].

Figure 5.19 illustrates the calculations of energy gaps of (111)-oriented SnTe thin films, with (a),(c) cationic TP and (b),(d) anionic TP. In every second odd number of layers, the films exhibit the same type of atom termination. Thus, the energy gap of (111)-SnTe films can be categorized separately for cation-terminated (anion-terminated) surfaces and cationic TP, as depicted in Fig. 5.19(a) [Fig. 5.19(c)], and for anion-terminated (cation-terminated) surfaces and anionic TP, as shown in Fig. 5.19(b) [Fig. 5.19(d)]. The findings reveal that for cationic TP films, band inversion is anticipated within $15-29$, 33, and $51-59$ monolayers. Meanwhile, for anionic TP, band inversion occurs within $21-27$, 31, and 57 monolayers. The topological phase is determined through calculations of both the $\mathbb{Z}_2$ invariant and the (111) mirror Chern number. The calculated values of $\nu = 1$ and $|C_m| = 1$ have been obtained for the thickness range indicated by the gray shading while the remaining thicknesses have $\nu = 0$ and $|C_m| = 0$.

In sections 5.1 and 5.2, we have demonstrated that the (111) Berry curvature maps in the ΓMK plane are qualitative similar between the cat-cat TSL and the (111) slab with a single cationic TP, as well as between the an-an TSL and the (111) slab with a single anionic TP. Therefore, each of these Berry curvature calculations can be used to approximate the corresponding map for a certain type of TP. For the sake of simplicity, we will focus on explaining the topology of TPs using the implementation of TSLs.

Of particular note is that the calculations in sections 5.1 and 5.2 utilized a simplified p-orbital TB parametrization. However, in this section, we employ a different parametrization (i.e., spd-orbital TB parameters), similar to the one used for the results depicted in Fig. 5.18. To enhance clarity, we begin by presenting the Berry curvature maps of cat-cat

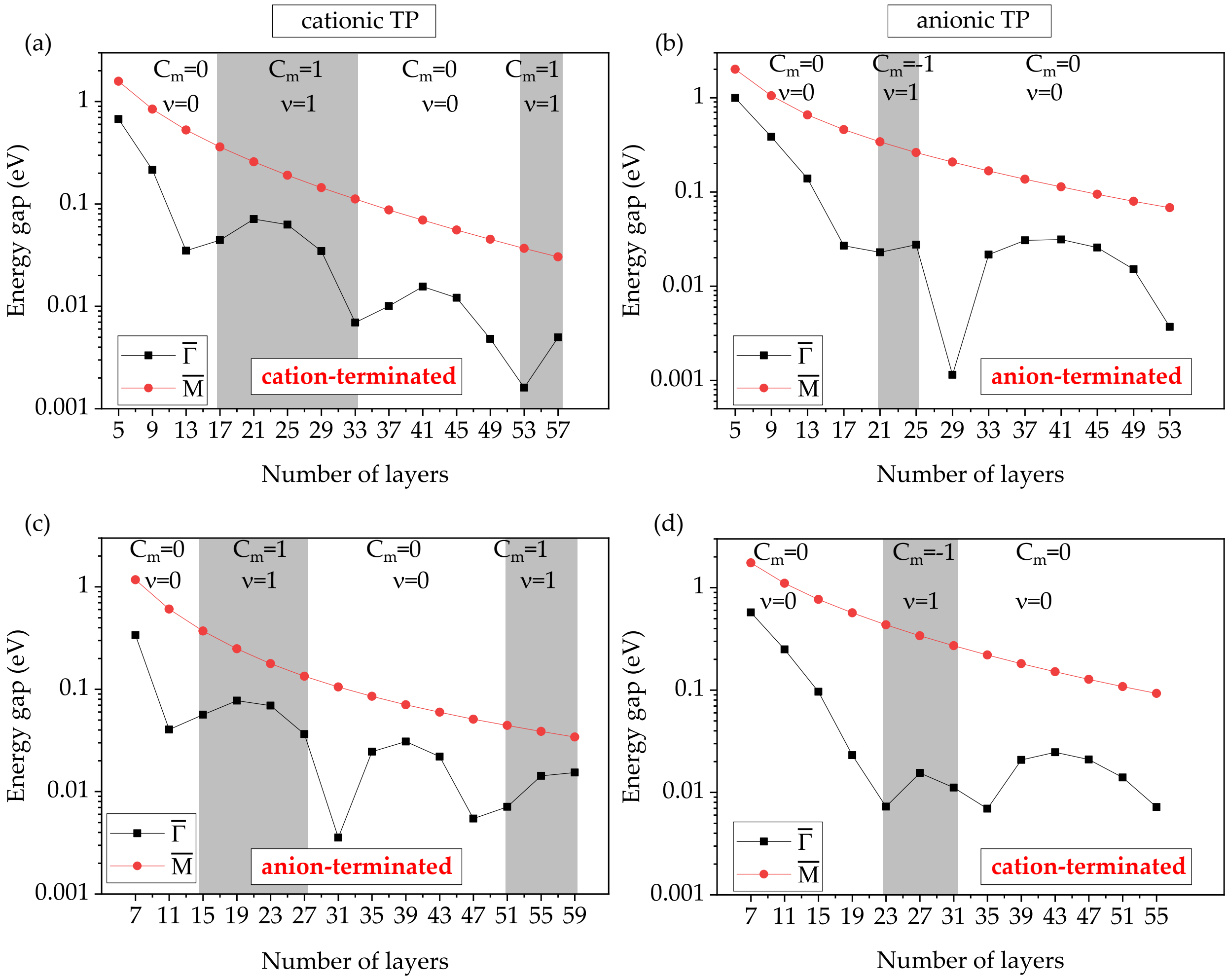

Figure 5.19: Energy gaps in (111)-oriented films with an odd number of monolayers in the presence of (a) a cationic TP and cation-terminated surfaces, (b) an anionic TP and anion-terminated surfaces, (c) a cationic TP and anion-terminated surfaces, and (d) an anionic TP and cation-terminated surfaces. The gray shadowed zones show the thicknesses where the value $\nu = 1$ and $|C_m| = 1$ has been obtained.

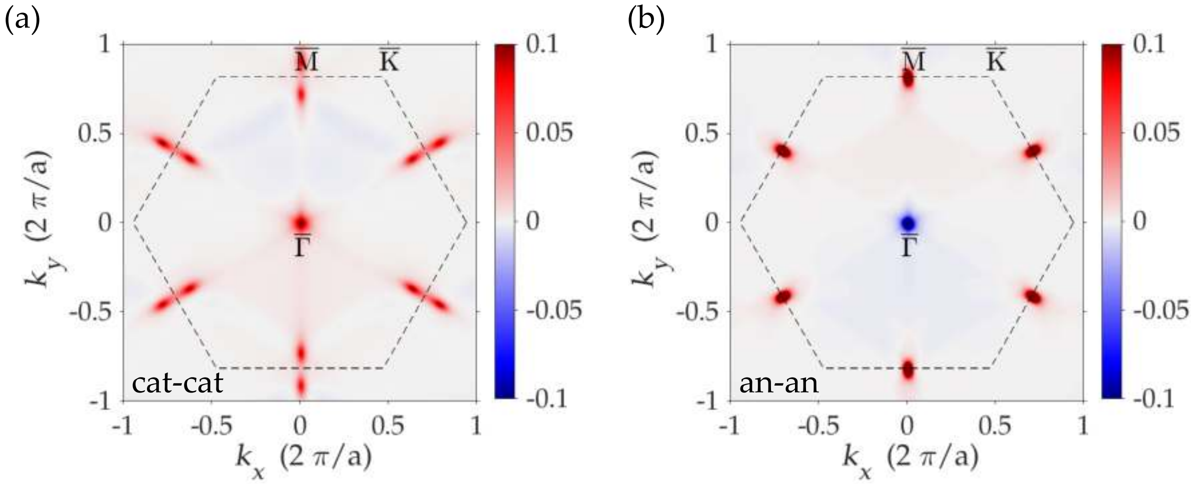

Figure 5.20: The Berry curvatures related to $+i$ (111) mirror subspace are determined for two types of TSLs: (a) cat-cat TSL and (b) an-an TSL with a height of 32 atomic layers. The maps are calculated using the SnTe TB parametrization based on the *spd* orbitals. The boundaries of the BZ are indicated by dashed lines.

and an-an SnTe TSLs. These maps were calculated using the *spd* TB parametrization, as depicted in Fig. 5.20. The calculated mirror Chern numbers are $C_m = 4$ for cat-cat TSL and $C_m = 2$ for an-an TSL. These calculations are particularly useful when computing the Berry curvature for (111)-SnTe films. In thin films, the strong interaction between the top and bottom surfaces results in dominant hybridization effects compared to the influence of TP. Here, we present the computed Berry curvature for films with varying heights for both cationic (Fig. 5.21) and anionic TPs (Fig. 5.22). In the case of films with cationic TPs, the Berry curvature is computed for films with thicknesses of 9, 21, 41, and 57 atomic layers. As the thickness increases, the contribution of the TP to the Berry curvature becomes more pronounced (compare Fig. 5.20 with Fig. 5.21). However, the TP effect is still fragile and is destroyed by the hybridization with (111) surface states.

The resulting maps of the film with cationic TP indicate the presence of a single band inversion at the $\overline{\Gamma}$ point [refer to Fig. 5.21(b) and (d)]. In this case, the calculated (111) mirror Chern number and $\mathbb{Z}_2$ invariant are equal to $C_m = -1$ and $\nu = 1$ respectively. This is evident from locally integrating the intensities of Berry curvature around the $\overline{\Gamma}$ point, which yields a value of -1, while being compensated elsewhere. Similar results are observed in the case of anionic TP films [see Figs. 5.22(b) and (d)]. However, the local intensity near the $\overline{\Gamma}$ point exhibits a value of $+1$.

The above findings provide compelling evidence of the fragility of the TP effect on the hybridization of TP wavefunctions with surface states. This observation helps explain why two topologically distinct TPs, namely cationic TP with $C_m = 2$ and anionic TP with $C_m = 1$, exhibit almost similar patterns of topological phase transition. In the larger

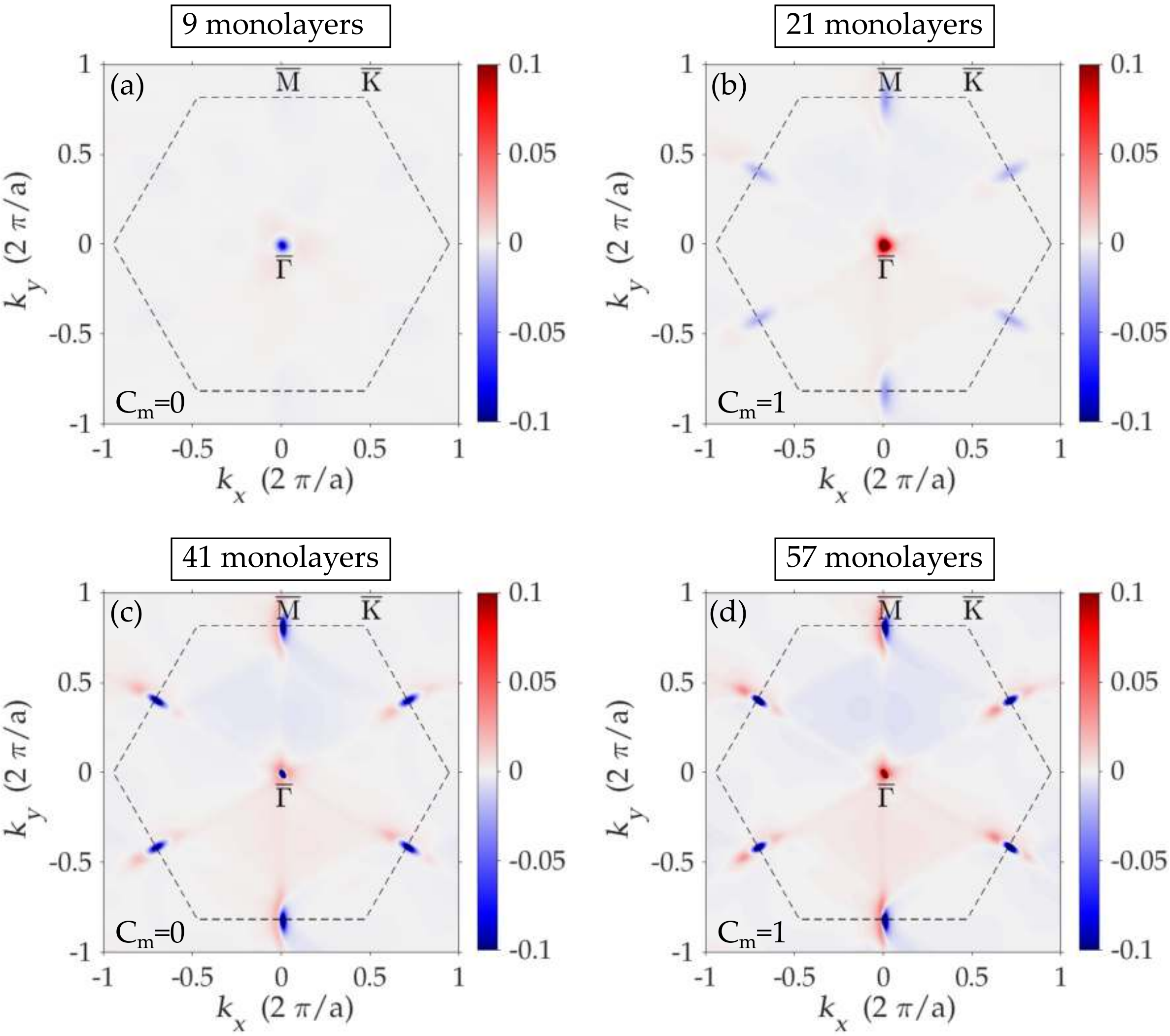

Figure 5.21: The calculation of Berry curvatures related to the $+i$ of (111) mirror subspace for cationic TP thin films: (a) 9 monolayer-thick, (b) 21 monolayer-thick, (c) 41 monolayer-thick, and (d) 57 monolayer-thick SnTe films. The BZ boundaries are indicated by dashed lines and the value of mirror Chern number is shown in each inset.

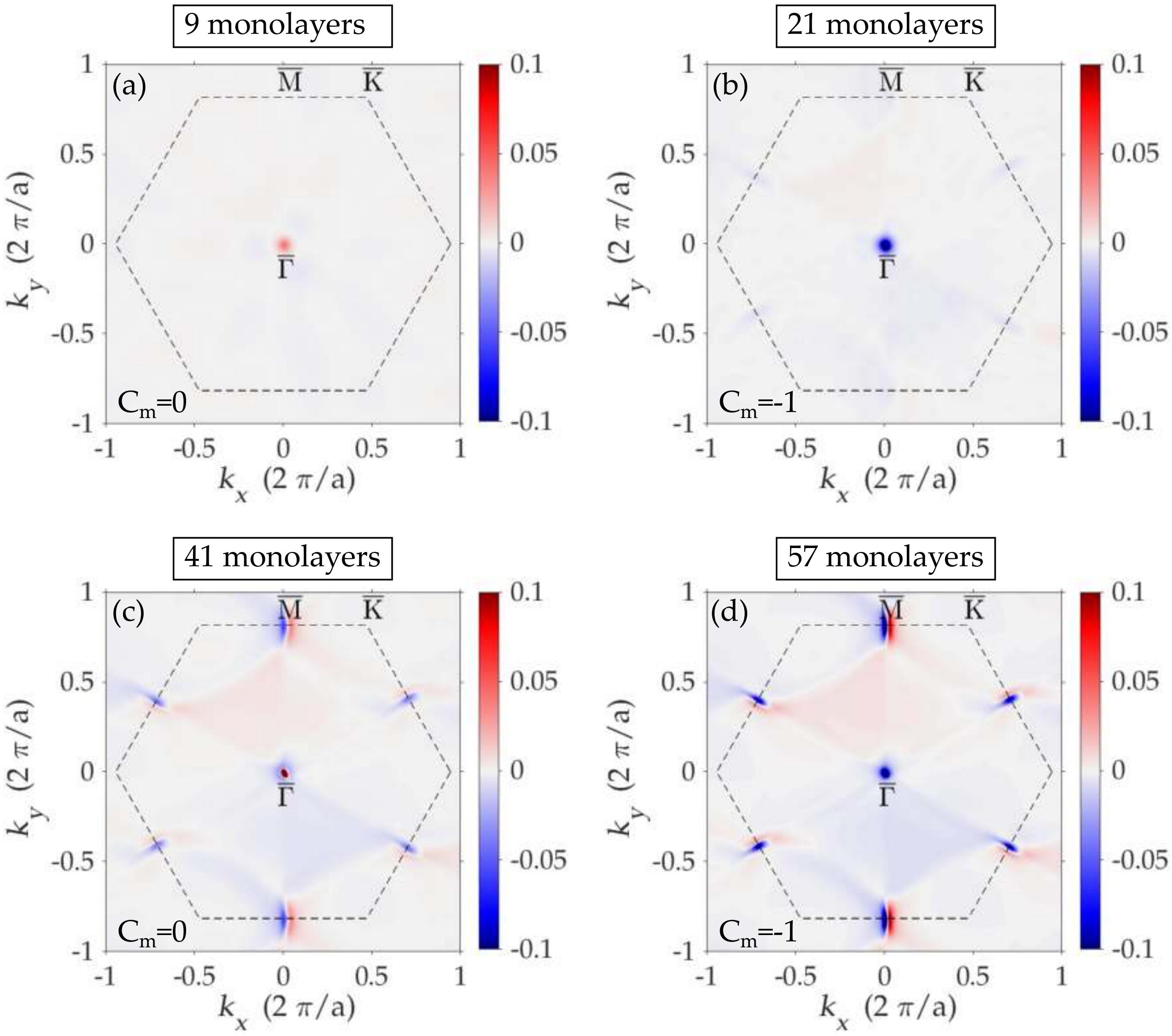

Figure 5.22: The calculation of Berry curvatures related to the $+i$ of (111) mirror subspace for anionic TP thin films: (a) 9 monolayer-thick, (b) 21 monolayer-thick, (c) 41 monolayer-thick, and (d) 57 monolayer-thick SnTe films. The BZ boundaries are indicated by dashed lines and the value of mirror Chern number is shown in each inset.

thickness slabs ($\sim$57 atomic layers), the wavefunctions of the two (111) surfaces experience minimal mixing, however, the effect of surface states hybridization still cancel out the effect of TP curvature at M points [compare Figs 5.20, 5.21(d) and 5.22(d)]. In the limit of sufficiently large slabs (as shown in the previous section, Fig. 5.13), the hybridizations of two (111) surface wavefunctions become negligible. However, the slabs exhibit gapless surface states band structures, which make it impossible to calculate Chern number beacuse of zero energy gap.

5.3.2 Edge spectral Green functions

The emergence of gapless edge states within the 2D bulk gap provides evidence for the nontrivial phase indicated by a nonzero mirror Chern number and $\mathbb{Z}_2$ invariant. In the current scenario, the calculated mirror Chern number is equal to $|C_m| = 1$ due to a single band inversion occurring at the high-symmetry $\overline{\Gamma}$ point. Consequently, a gapless helical edge states is expected to occur at the projection line of $\overline{\Gamma}$, which are protected by both time-reversal and (111) mirror symmetries.

For the sake of clarity, we have used recursive Green's function method to calculate the edge spectral function of the film. In Figs. 5.23 and 5.24 we present the $[11\bar{2}]$ edge spectral functions of a (111)-oriented SnTe film with a single TP, where both surfaces host same types of atom as TP. The bulk density of states for a 21 monolayers cation-terminated film with cationic TP at $\overline{\overline{\Gamma}}$ and $\overline{\overline{\mathrm{M}}}$ are presented in Fig. 5.23(a) and Fig. 5.23(b) respectively. Associated with these bulks, their edge states are shown in Fig. 5.23(c) and Fig. 5.23(d). The density of states results for another film consisting of 13 monolayers at $\overline{\overline{\Gamma}}$ and $\overline{\overline{\mathrm{M}}}$ are shown in Fig. 5.23(e) and Fig. 5.23(f). In agreement with the $\mathbb{Z}_2$ and C_m invariant calculations, the linear-dispersion gapless state is obtained for 21 monolayers at $\overline{\overline{\Gamma}}$ point but not at $\overline{\overline{\mathrm{M}}}$. The corresponding topological invariants for 21-layer film are calculated and equal to $\nu = 1$ and $C_m = -1$. However, for 13 atomic-layer film the band gap is not inverted and the calculated toplogical invariants are $\nu = 0$ and $C_m = 0$, indicating a trivial 2D TIs. Similarly a set of calculations has been done for anion-terminated film with anionic TP (see Fig. 5.24). Appearing the Dirac crossing at $\overline{\overline{\Gamma}}$ point for a 21 monolayers film, verifies the nontriviality of the film indicated by $\nu = 1$ and $C_m = 1$ corresponds to QSH phase.

Ultimately, $G_\uparrow$ and $G_\downarrow$, the contributions of the spin up and spin down (111) projections in the edge spectral function have been calculated. The sign of $G_\uparrow - G_\downarrow$ difference corresponds to spin-polarization of the edge states. Figure 5.25(a) displays a single spin-polarized Dirac cone of the 21-monolayer SnTe for cation-terminated with cationic TP film

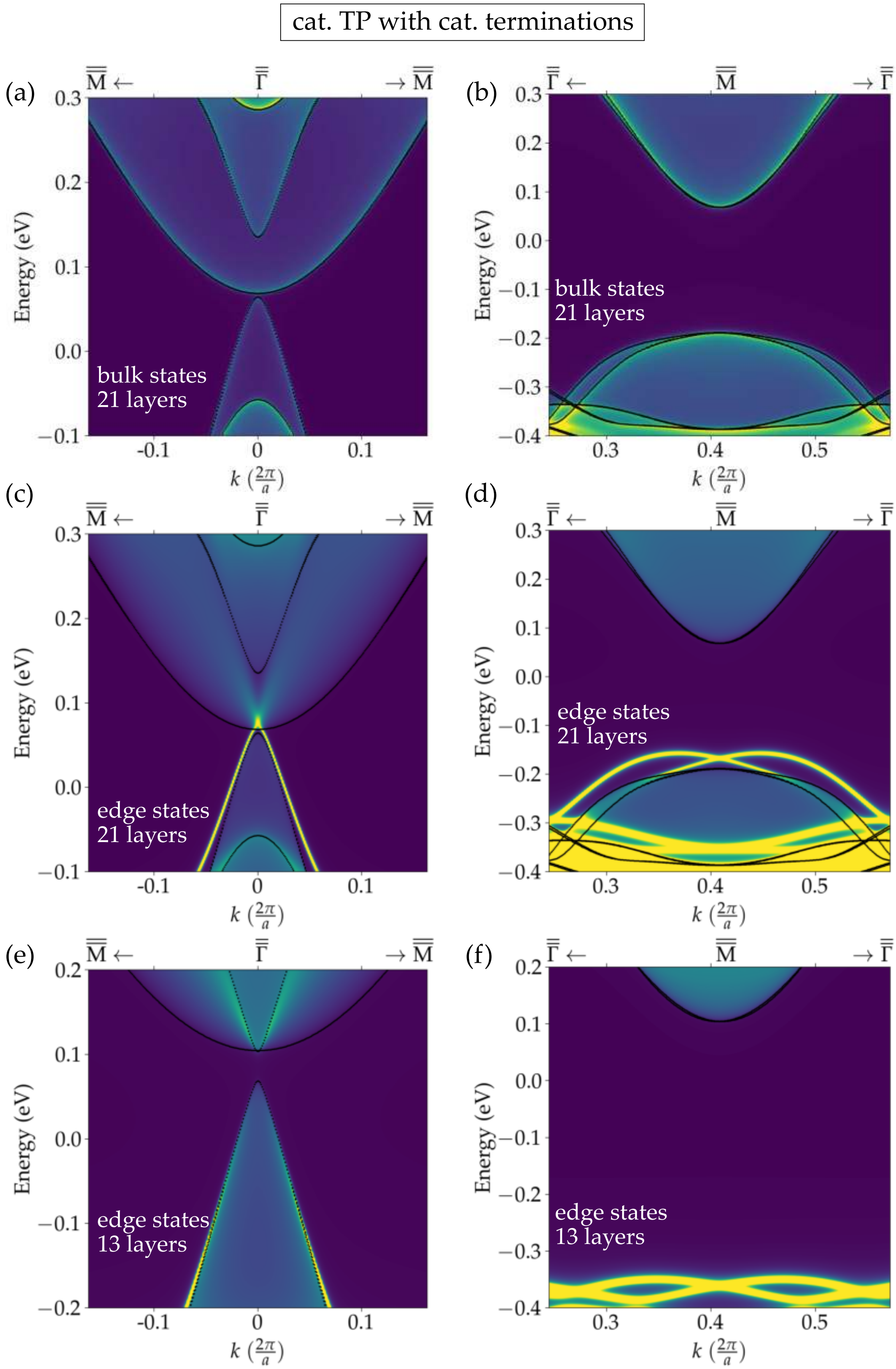

Figure 5.23: Spectral functions of cation-terminated (111)-SnTe film along 1DBZ of its $[11\bar{2}]$ edge with cationic TP in the vicinity of $\overline{\overline{\Gamma}}$ (left column) and $\overline{\overline{\mathrm{M}}}$ (right column) points. Outlines of the 2D film bands projected to the edge are denoted by black dotted lines.

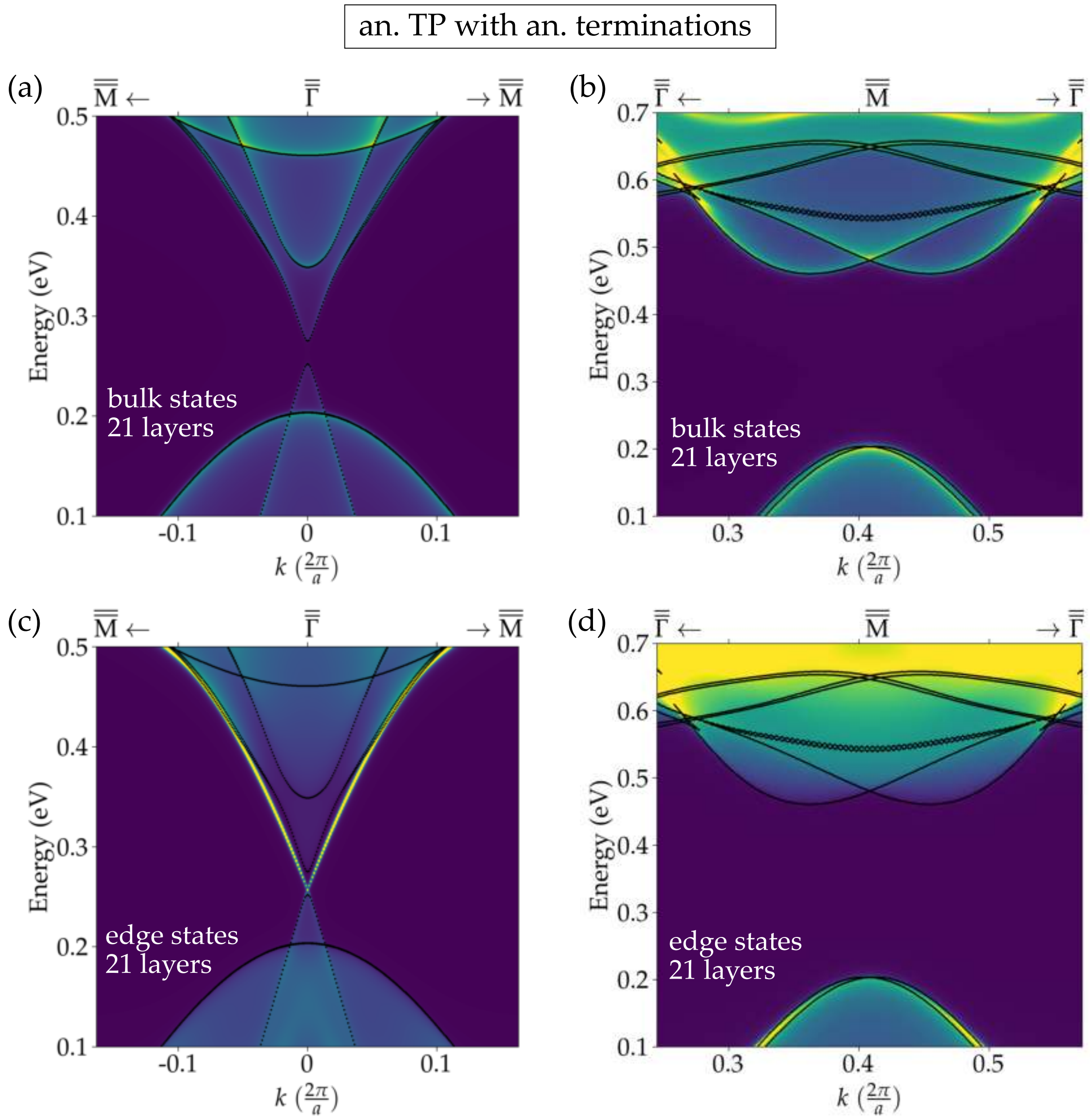

Figure 5.24: Spectral functions of anion-terminated (111)-SnTe film along 1DBZ of its $[11\bar{2}]$ edge with anionic TP in the vicinity of $\bar{\bar{\Gamma}}$ (left column) and $\bar{\bar{\mathrm{M}}}$ (right column) points. Outlines of the 2D film bands projected to the edge are denoted by black dotted lines.

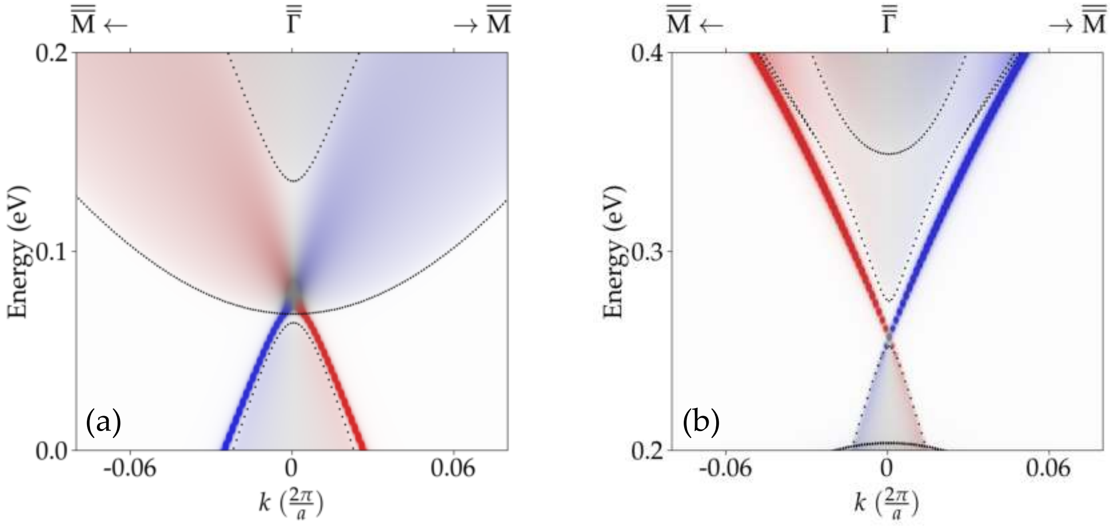

Figure 5.25: Spin density of sates of (111)-SnTe film along 1DBZ of its $[11\bar{2}]$ edge with (a) a cationic TP (b) an anionic TP for 21 monolayer-thick film having $|C_m| = 1$. The blue and red colors indicate the spin-down and spin-up polarizations, respectively. Outlines of the 2D film bands projected to the edge are denoted by black dotted lines.

near the $\overline{\overline{\Gamma}}$ point ($k = 0$), consistent with $\nu = 1$ ($|C_m| = 1$). The red and blue color indicate the spin-down and spin-up polarizations, respectively. Figure 5.25(b) indicates the spin density of a (111)-oriented SnTe film with anionic TP and anionic terminations, featuring a 21-monolayer height, where the Z_2 invariants and mirror Chern number obtained in the bulk film are $\nu = 1$ and $|C_m| = 1$, respectively. The appearance of spin-polarized edge states at the $\overline{\overline{\Gamma}}$ point of the 1D edge of the 2D film is obtained. It should be reminded that the black dotted lines through the spectral figures imply the border of slab states projection onto the edge.

5.4 Topological crystalline insulator nanowires

A low-dimensional nanostructures, e.g., films, heterostructures, composed of SnTe TCI material have gained substantial attention in recent years for investigating topological physics and developing innovative quantum devices [18, 86]. In addition, a number of publications have been focused on the synthesis and characterization, with distinct facets and morphologies in NWs and nanocrystals [141–148]. The growth mechanisms and crystal shape engineering of SnTe nanostructures have been investigated, aiming to understand the impact of crystal shape on material characteristics [142, 144]. Moreover, the topological surface transport properties of SnTe nanowires have been studied, shedding light on their potential applications in nanoscale electronics and spintronics devices [143].

To date, there has been a greater emphasis on the fabrication of SnTe NWs rather than the experimental investigation of their topological properties. However, this situation is anticipated to evolve as there are continuous advancements in nanowire fabrication techniques [147, 148]. In parallel, some theoretical investigations have been conducted on cubic rocksalt NWs grown along the [001] direction [105, 106]. For instance, Nguyen et al. carried out a systematic study on the symmetries and topological invariants in SnTe NWs, revealing the existence of various types of topological states achieved through the utilization of tunable symmetry-breaking fields [105]. In addition, the possible existence of corner and hinge modes in these NWs has been investigated, highlighting their potential as platforms for exploring Majorana bound states in the proximity of a superconductor [105]. Furthermore, it has been recently shown that NWs possessing a pentagonal cross-section grown along the [011] direction can be achieved through the utilization of molecular beam epitaxy (MBE) techniques in the presence of a catalyst, in the $\mathrm{Pb_{1-x}Sn_xTe}$ material system [137].

The objective of this section is to explore the topological characteristics of wires that have been grown in two different directions, namely [011] and [001], with pentagonal and square cross-sectional shapes, respectively. In [001] NWs, the possible presence of similar hinge states has been proposed and characterized as a second-order topological phase [105]. In [011] NWs, however, we will show that the origin of hinge states is not attributed to a second-order phase, but rather arises from the topological properties of the twin planes arranged radially from the center to the five hinges.

5.4.1 Pentagonal cross-section nanowires grown along [011] direction

In this discussion, we will leverage the topological characteristics of individual twin boundaries to demonstrate the presence of one-dimensional dissipationless spin-polarized channels known as topological core states (TCS) at the NW core. Specifically, in the case of a cationic twin boundary, these TCS show up together with oppositely directed counterparts on the surface. However, in the case of an anionic twin boundary, such gapless modes are absent. Our symmetry analysis will also address the underlying mechanisms behind the emergence of these states and their topological protection.

The current study focuses on two different models: SnTe constructed with only p-orbitals up to second nearest neighbor and an empirical model for $Pb_{0.6}Sn_{0.4}Se$ within nearest neighbor sp^3d^5-orbital TB approximations (see Chapter 4).

5.4.1.1 Wire structure

The pentagonal-shaped NW is grown in the [011] crystallographic direction. The structure model can be seen in figure 5.26(b). It is made up of five trigonal segments that have a uniform rocksalt lattice. Each segment has a termination of (100), $(\bar{1}1\bar{1})$, and $(\bar{1}\bar{1}1)$ planes. The segments are rotated around the $[011]$ axis by integer multiples of 72° and are joined together such that the NWs' faces are composed of (100) planes, while 111 planes act as boundaries between the segments. Due to the properties of $\{111\}$ planes in rocksalt lattice, the TPs must be exclusively cationic or anionic.

This study focuses on the qualitative characteristics of pentagonal NWs, while disregarding their stability and relaxation of the atomic structures. It is worth noting, however, that the pentagonal NW exhibits inherent circumferential strain due to the angle between the two $\{111\}$ planes in a cubic structure, which is approximately 70.53 degrees, or approximately 1.47 degrees less than 72 degrees (i.e., a fifth of the full angle) [see Figs. 5.26(c),5.26(d)]. As a result, each of the five sections experiences uniaxial stress in the local $[01\bar{1}]$ direction, resulting in a strain of approximately 2%. Using the known stiffness constants for SnTe and PbSe and deformation potentials [149, 150], the two remaining non-zero components of the strain tensor in the [100] and $[01\bar{1}]$ directions can be estimated. Knowing also deformation potentials [150, 151], it is possible to rate the change of the energy gap in valleys perpendicular to and tilted towards the wire direction. The changes are below 10% of the gap of the unstrained bulk crystal for SnTe and below 20% for $Pb_{0.6}Sn_{0.4}Se$, and since these gap changes are not significant for the topological properties of the wire, they are not considered in further studies.

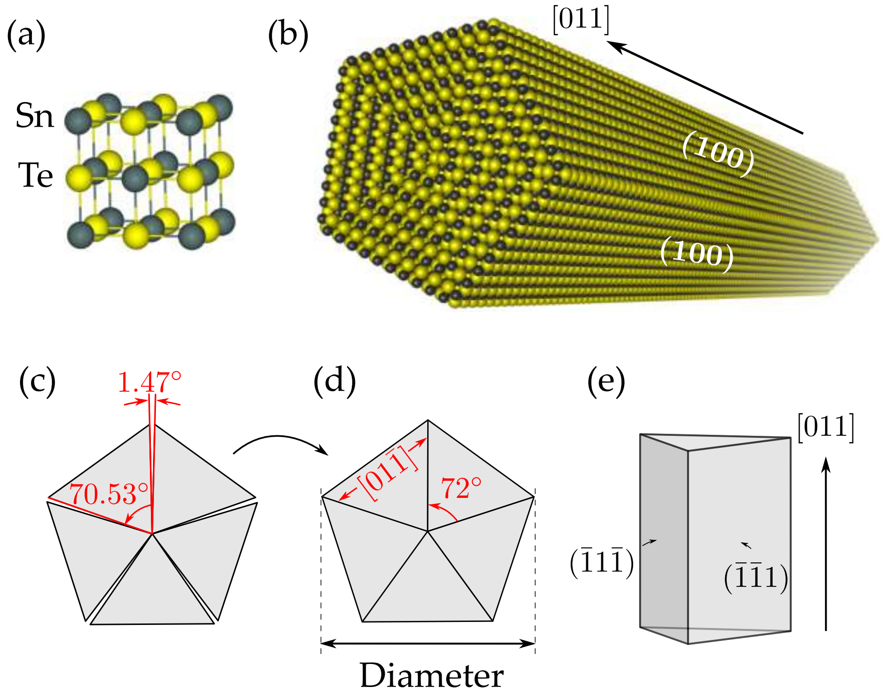

Figure 5.26: (a) The rocksalt crystal structure of IV-VI semiconductors. (b) The structure model of five-fold twinned nanowires grown along [011] axis, consisting of five $\{100\}$ facets and five $\{111\}$ TPs that can be made up of cationic or anionic atoms. (c) Sketch of cross-sectional view of NWs with 1.47° mismatching angle in each boundary of NWs (7.35° in total). A fully recovered pentagonal section shown in (d) by stretching of atomic sites in local $[01\bar{1}]$ directions towards $\{111\}$ twin plane boundaries. (e) Side view of one triangle of NWs.

In Figure 5.27, we can see a comparison between the one-dimensional BZ (1DBZ) of a nanowire and the fcc 3DBZ of the bulk. In the 3DBZ, the L points are projected in pairs onto two distinct points, namely $\overline{\mathrm{Z}}$ at the end of the 1DBZ and $\overline{\Gamma}$ in the middle, regardless of the wire section. As a result, the energy gaps of the wire and Dirac crossings are expected to be located around these points.

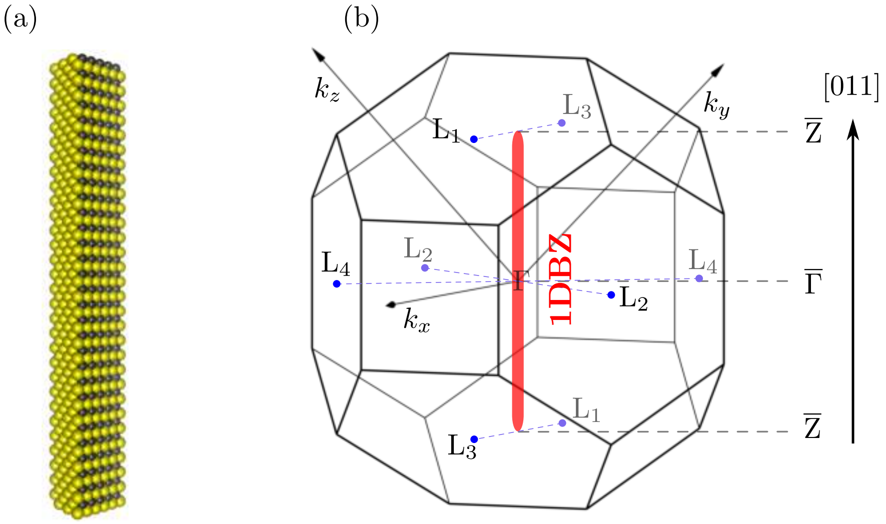

Figure 5.27: (a) Vertically perspective of one triangle of pentagonal NW along growth axis. (b) Three-dimensional face centered cubic (fcc) BZ and 1DBZ of the NWs. The projection of high symmetry L points of 3DBZ, is shown schematically as $\overline{\Gamma}$ and $\overline{\mathrm{Z}}$ points into 1DBZ. The 1DBZ repeated appropriately for each triangle section of NW.

5.4.1.2 Band structure of SnTe pentagonal nanowires

The low-energy band spectra of SnTe pentagonal wire is shown in Fig. 5.28. Due to the relatively big energy gap, which is equal to 330 meV for the parametrization used, the shown results include mainly surface, core and hinge states. Topologically protected surface states emerge due to the $(01\bar{1})$ mirror plane symmetry in each of the (100) facets of the wire [see Fig. 5.29(c) as an example]. Due to the confinement effect, however, they are gaped and split in many subbands.

Henceforth, we shall deliberate upon the origin of core and hinge states that exhibit a Dirac dispersion with zero mass. Notably, the manifestation of this phenomenon becomes perceptible in NWs of large thicknesses, where the localization length of the NW surfaces is significantly less than the NW diameter. Our computational analysis reveals that a minimum thickness of 14 nm is required for the observation of gapless hinge states. Remarkably, this feature is exclusive to TPs of cationic atomic type (Sn), while for the anionic case (Te) the states are always gapped. The wave function weight of atomic sites within the core (approximately two rings in radius) and on the surface (last three rings) is

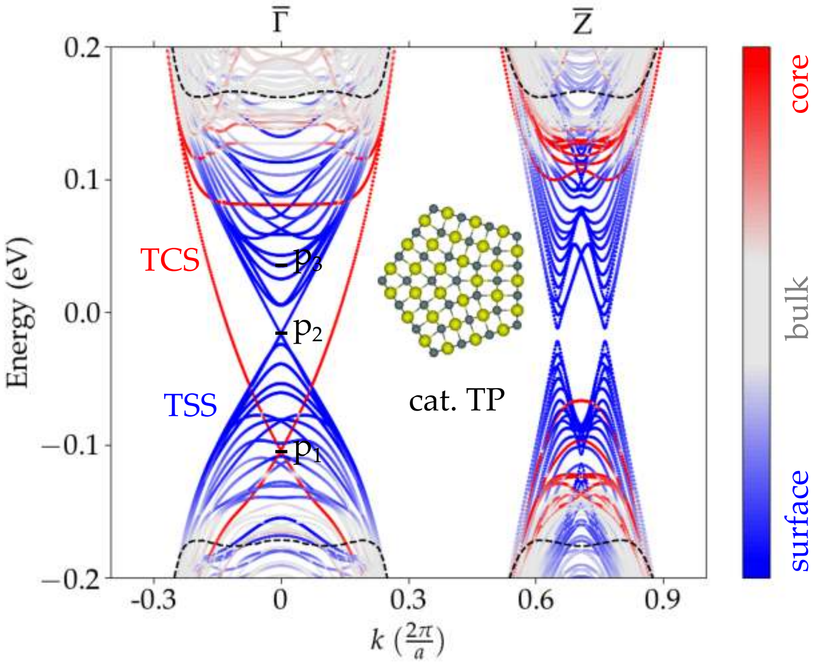

Figure 5.28: Band structure calculation of SnTe NWs with cationic TPs. Inset: schematic pentagonal NW cross section with cationic TPs. Observation of TCS and TSS in the spectrum obtained for 14 nm (20 rings) thickness only at $\overline{\Gamma}$ point. The red and blue indicate the wave function weight on core and surface atomic sites, respectively, while gray indicates the bulk-like intermediate sites. Outlines denote the projected continuum bulk bands into 1DBZ edge given by dashed lines.

indicated by red and blue components, respectively. The localization of the core state at the Dirac point p_1 (compare with Fig. 5.28), indicates the presence of a topological core defect as shown in Fig. 5.29(a). Furthermore, the gapless core state coexists with the gapless surface states on the $\{100\}$ sides of the wire, and for the energies close to the Dirac point p_2 are localized at the hinges [Fig. 5.29(b)]. Henceforth, these states will be referred to as hinge states. The calculated localization map corresponds to the gapless hinge states, denoted by p_2 in Fig. 5.28. Figure 5.29(c) illustrates the localization map of the quantized surface states at p_3 in Fig. 5.28. These states originate from the bulk properties of SnTe TCI due to the presence of the $(01\bar{1})$ mirror plane in each triangular section perpendicular to the (100) wire sides.

It is worth mentioning that the gapless hinge states can hybridize with each other and with surface states. Even as the diameter of the nanowire increases, the hinge and surface states remain intertwined, and their mixing cannot be eliminated without introducing a gap in the intermediate $\{100\}$ surfaces. Despite the presence of five vertices in a cross-sectional view of the wire, which would theoretically generate five distinct hinge states, we have observed that only one pair of nondegenerate states forms the Dirac crossing. Through an analysis of the wire's eigenstates, we have determined that this pair belongs

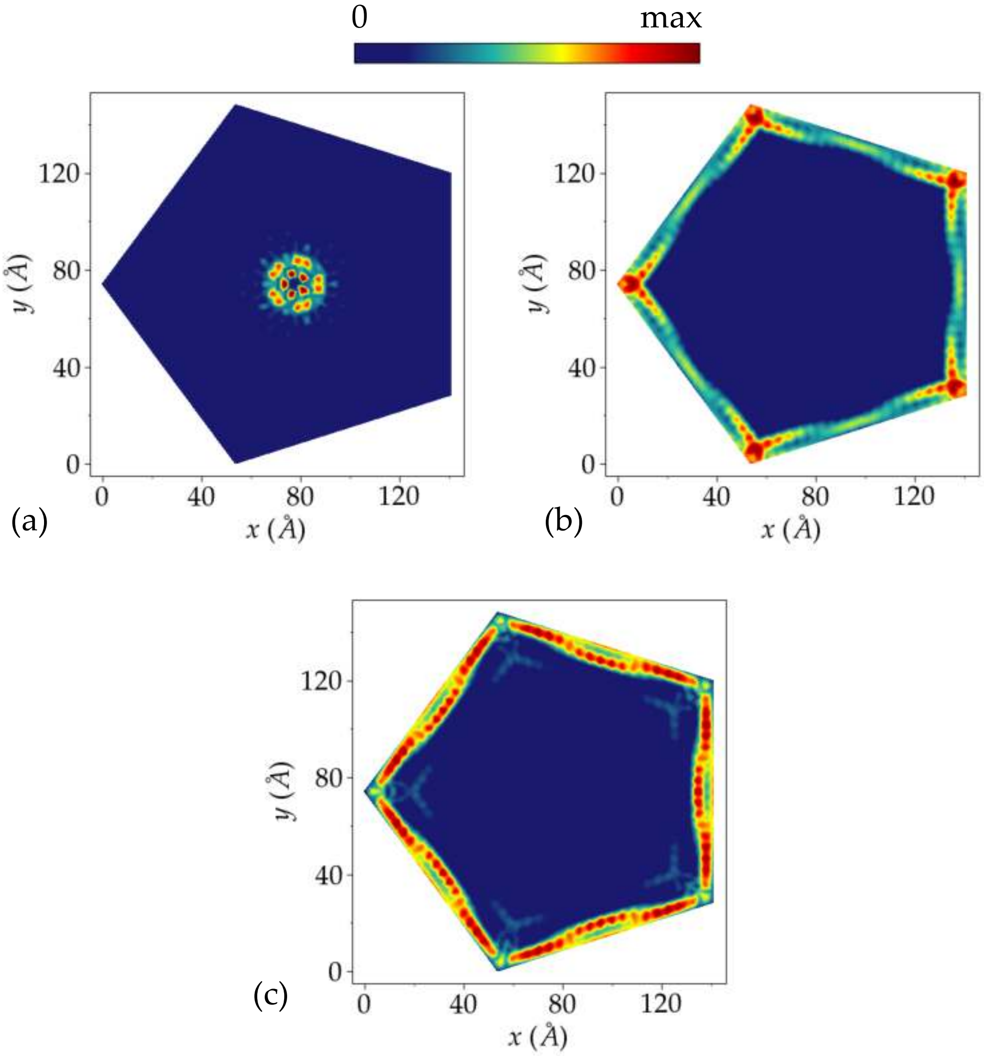

Figure 5.29: Spatial distribution of localized Dirac-like (a) core state (at p_1), (b) hybridized hinge states (at p_2) and (c) conventional TCI surface states (at p_3) presented by sum of the squared moduli of the wave functions, respectively. The calculation obtained for 14 nm (20 rings) thickness for cationic TP and the p_i, $i = 1, \ldots 3$ is shown in Fig. 5.28.

to a subspace of the C_5 symmetry operator, corresponding to the eigenvalue of $\lambda = -1$. The appealing result of band structure calculation is shown in Fig. 5.30(c). The computed band structures depicted in Figs. 5.30(a),(b),(d), and (e) exhibit trivial states with an open gap that corresponds to the subspaces $\lambda = e^{-i\frac{3\pi}{5}}$, $e^{-i\frac{\pi}{5}}$, $e^{i\frac{\pi}{5}}$, $e^{i\frac{3\pi}{5}}$, respectively. Additionally, the symmetry analysis reveals that $[C_5, M_{(01\bar{1})}] = 0$ in $\lambda = -1$ subspace. Thus, we can decompose the Hamiltonian of the eigenspace of $C_5^{\lambda=-1}$ to the mirror eigenvalues of $M_{(01\bar{1})}$. The band structure obtained from this decomposition exhibits the coexistence of the gapless core state and the gapless hinge state with opposite chirality within $C_5^{\lambda=-1}$ and M_{-i}, as demonstrated in Fig. 5.30(f).

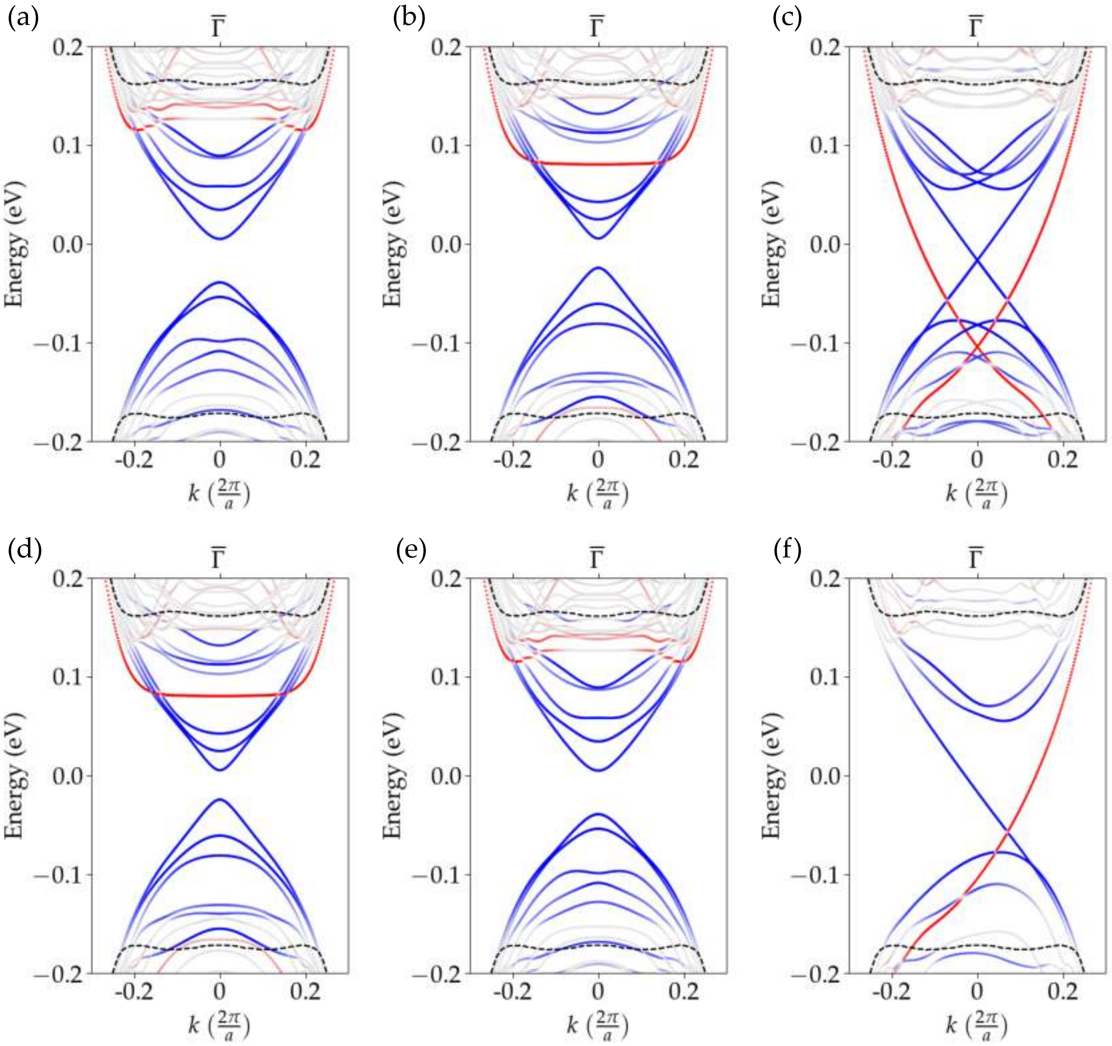

Figure 5.30: The decomposition of the Hamiltonian into C_5 rotation symmetry subspaces. Panels (a)-(e) depict the band structures corresponding to the eigenvalues $\lambda = e^{-i\frac{3\pi}{5}}$, $e^{-i\frac{\pi}{5}}$, -1, $e^{i\frac{\pi}{5}}$, $e^{i\frac{3\pi}{5}}$, respectively. Panel (c) illustrates the presence of non-trivial TCS, along with its counterpart TSS, in the $C_5 = -1$ eigenspace. Panel (f) illustrates the $-i$ subspace of the $M_{(01\bar{1})}$ mirror plane within the $C_5 = -1$ decomposed Hamiltonian.

Also electronic states forming Dirac cross in the core belong to the same subspace of C_5. The appealing result may be suspected by the missing atomic bond in the center of NWs, which leave an extra charge in the system in both cationic and anionic twin-plane NWs. However, it can be verified that there are no states belonging to $C_5 = -1$ subspace localized on the central atom built with s and p orbitals. In other words, central atom plays no role in existence of TCS and Dirac core states are made up with orbitals of atoms forming rings around center of wire [4].

It is important to note that altering the atomic order does not impact the overall atomic structure of the wire section. Rather, it solely affects the TP atomic sites, which consequently alters the type of core atom [compare insets in Figs. 5.28 and 5.31]. Figure 5.31 illustrates a fivefold wire structure with an anion at its core. Analysis of the solutions within the midgap bands suggests a lack of connection between the valence and conduction bands, indicating that the system is topologically trivial. It is noteworthy that despite the core state displayed in the figure touches conduction bands, it does not possess topological nontriviality. This is attributed to the absence of core mode which is not concomitant with Dirac-like dispersion near the $\overline{\Gamma}$ point. It is worth highlighting that the anti-crossing persists even for much greater thicknesses of the NWs.

The results presented in Ref. [133] support the idea that there are two topologically distinct properties corresponding to the two types of TPs in the [111] TSL implementation, where the topological identification of TP is defined by (111) mirror Chern number. The research has demonstrated explicitly that cationic and anionic TPs exhibit topologically different behavior upon the appropriate (111) section of the 3D hexagonal BZ. Additionally, the edge calculations of the TP slab supercell and NWs along similar direction of its 1DBZ indicate that cationic-type TPs exhibit topologically nontrivial states while anionic-type TPs have trivial states at the $\overline{\Gamma}$ point.

5.4.1.3 Band structure of $\mathrm{Pb_{0.6}Sn_{0.4}Se}$ pentagonal nanowires

In this section we are conducting a study on ternary alloys comprising of $\mathrm{Pb_{1-x}Sn_xSe}$ semiconductor nanowires with a 40% concentration of tin with the similar growth axis [011]. The compound exhibits a nontrivial topological phase in its 3D bulk, with an inverted band gap of approximately 190 meV. We conducted a comprehensive study of the electronic properties of this material across a wide range of diameters, including both

---

[4] The above analysis conducted by Rafał Rechciński proves that contributions involving d and f orbitals can indeed exist in the central atom for $C_5 = -1$ subspace

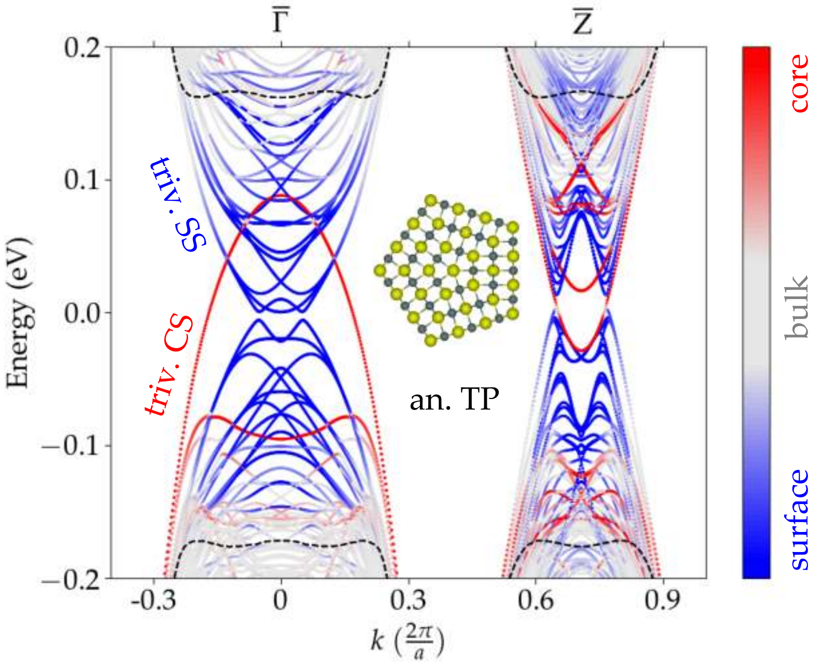

Figure 5.31: Band structure calculation of SnTe NWs with anionic TPs. Inset: schematic pentagonal NW cross section with anionic TPs. Observation of topologically trivial (triv.) CS and SS in the spectrum obtained for 14 nm (20 rings) thickness. The blue and red project the wave function weight on core and surface atomic sites, respectively. Dashed lines denote the projected of top of valence and bottom of conduction bands in the continuum bulk.

cationic [Figs. 5.32(a)–(d)] and anionic [Figs. 5.32(e)–(h)] twin planes. The calculated spectra in Fig. 5.32 indicate that a Dirac crossing may only exist near the $\overline{\Gamma}$ point, while anti-crossings always appear near $\overline{Z}$. We started with a thickness of $w = 14.3$ nm for both types of nanowires, and the weight of wave functions around central atomic sites is represented by the color red. The selected radius corresponds to approximately two rings around the central atom. The narrow nanowires exhibit a confinement effect that causes nearly zero energy states to hybridize with surface states, leading to the opening of a gap and anti-crossing band dispersion. However, in cationic nanowires with diameters larger than $w = 28.6$ nm (40 rings), linear gapless dispersion can be observed at the $\overline{\Gamma}$ point, as depicted in Figs. 5.32(c) and 5.32(d).

As in the case of SnTe wires, despite the core state and its partner being localized in all $\{100\}$ facets, a significant number of states exist within the band gap. These states are surface states that become quantized as a result of confinement. Moreover, in $Pb_{0.6}Sn_{0.4}Se$ nanowires with anionic twin boundaries, it is observed that as the thickness increases (up to 35.6 nm), the core state makes an attempt to retrieve anti-crossing behavior while the hybridization effect diminishes. Similar to the anionic-type NWs in SnTe, the core state in $Pb_{0.6}Sn_{0.4}Se$ NWs with anionic TPs is topologically trivial, as shown in Fig. 5.32(h).

It should be emphasized that this phenomenon is not attributed to any structural defects. This is evident from the observation that no Dirac crossings are present in systems with a lower Sn content ($x < 0.2$) that are topologically trivial. Thus, the negative sign of the band gap plays a critical role in the observation of such phenomena.

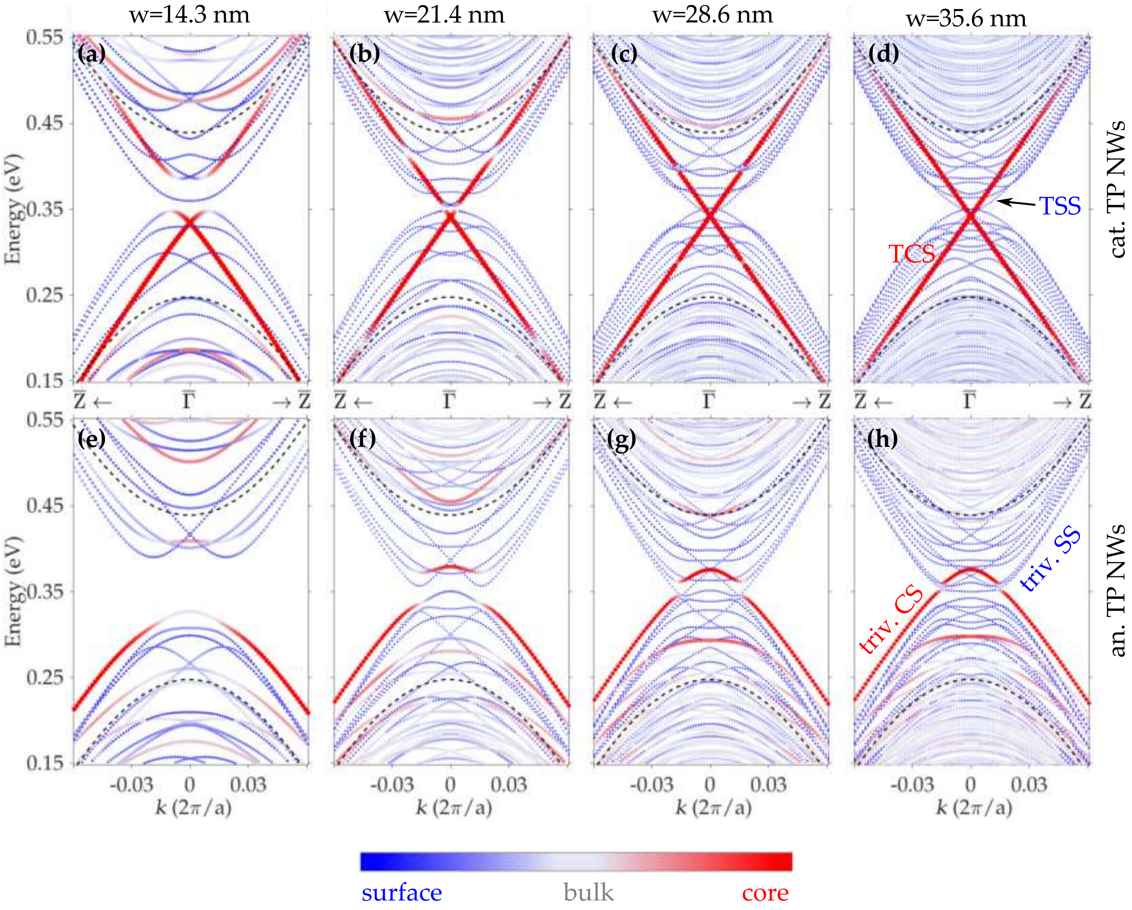

Figure 5.32: The various calculated band structures of $Pb_{0.6}Sn_{0.4}Se$ NWs with cationic (upper row) and anionic (lower row) TPs. The spectra obtained by TB model using sp^3d^5 orbitals and with spin-orbit coupling. The nontrivial core state is presented in upper row, however in (a) and (b) due to a small size and confinement effect the core sates hybridize with surface states which open the gap. In (c) and (d) for sufficiently large diameter the TCS and TSS can be found at $\overline{\Gamma}$. Panels (e)-(f) represent the anti-crossing trivial core state of the NW hosting twin boundaries with anions. Similar confinement effects can be seen in respective systems. The red (blue) dotted lines display the weight of wave functions near core atom (surfaces). Dashed lines denote the projected of top of valence and bottom of conduction bands in the continuum bulk.

5.4.1.4 Band structure of SnTe NWs with $(21\bar{1})$ crystallographic facets

In this section, we present the band structure calculations for NWs with $(21\bar{1})$ facets oriented along the [011] direction. The cross-sectional configurations of the NWs are built by the positioning of the TP in the center of each of the five facet sides. As a consequence,

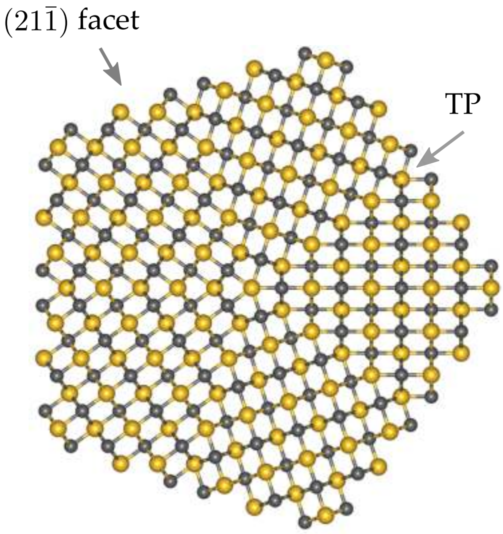

Figure 5.33: Cross-section of a pentagonal wire with $(21\bar{1})$ facets, showing the position of the TPs in the center of each surface.

the NW hinges are not located at the edges of the TPs. Figure 5.33 depicts the structural arrangement of the NWs in which the TP is indicated by Te (shown by arrow).

As discussed in the preceding section, the intriguing topology of interest manifests in the $C_5 = -1$ subspace. Therefore, it suffices to perform band structure calculations solely within the $C_5 = -1$ subspace. In the case of cationic TP, the band structure of SnTe for a thickness of 16 nm is depicted in Fig. 5.34(a). Notably, the topological core state (indicated in red) is observed alongside its counterpart surface states (shown in blue). By examining the wavefunction at the Dirac point $p1$, it becomes evident that the states are well-localized around the center [Fig. 5.34(b)]. In contrast, at the Dirac point $p2$, the wavefunctions spread across the entire surfaces [Fig. 5.34(c)]. Similarly, band structure calculations were performed for anionic TP within the $C_5 = -1$ subspace, which revealed that no Dirac crossing appears in the midgap [see Fig. 5.35], in line with the results obtained for (100) facet NWs.

The above results verify that the topological core state is depended on the individual topological properties of the TP and is unaffected by the positioning of the TP as long as C_5 symmetry preserved.

The results presented above confirm that the *single* topological core state is dependent on the intrinsic topological properties of an individual TP and remains unaffected by its position within the NW cross-section, provided that the C_5 symmetry is preserved.

5.4.1.5 Hinge states in a pentagonal NWs

In Section 5.4.1.2, we conducted a rigorous investigation of the electronic properties of the SnTe NWs through band structure calculations based on p orbital TB parametrization. We

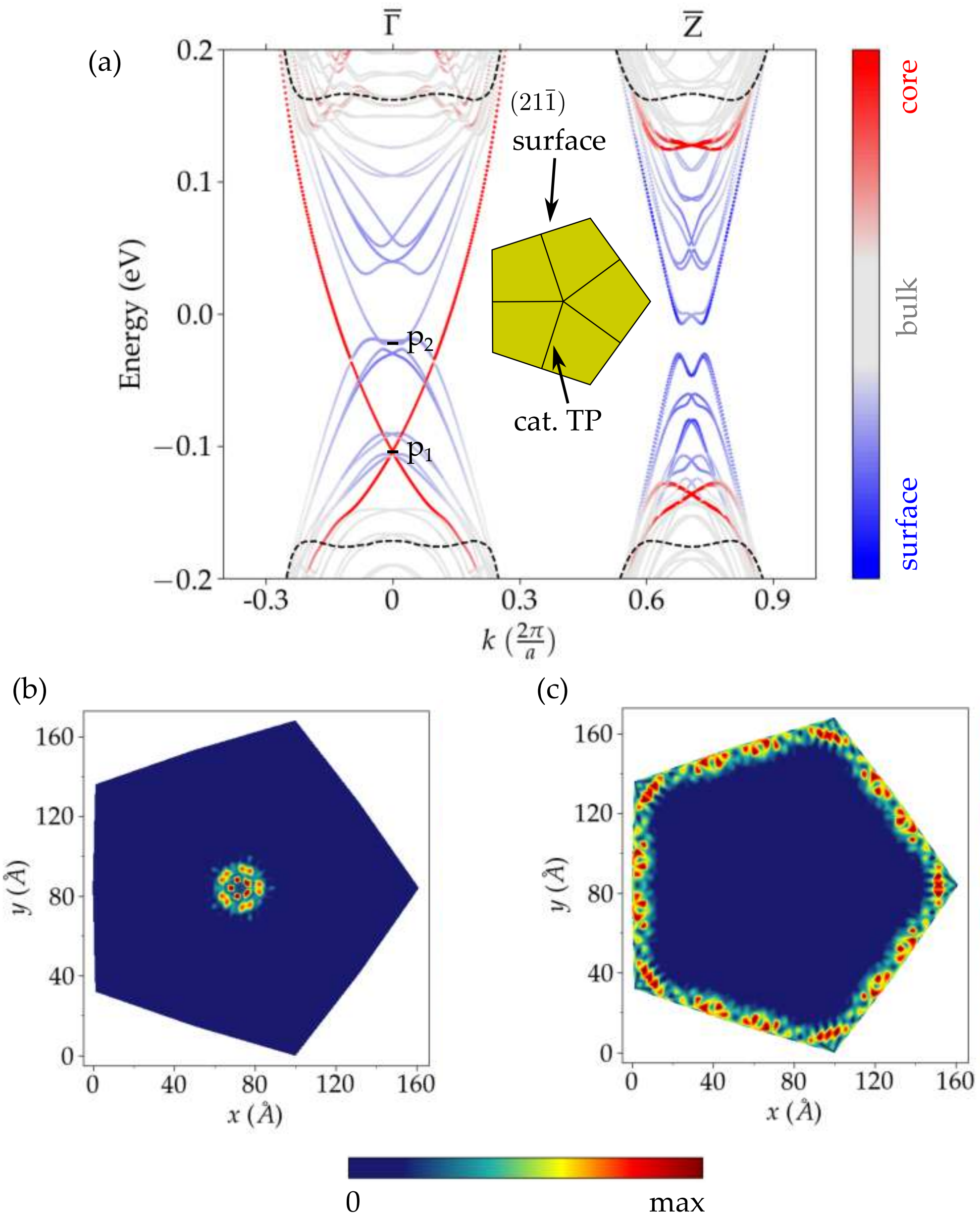

Figure 5.34: The electronic band structure of a SnTe pentagonal wire is calculated within $C_5 = -1$ subspace system, where cationic TPs are present. Inset: a schematic cross-section of a pentagonal NW, with (21$\bar{1}$) facets and cationic TPs located at the center of each surface. (a) The presence of TCS and TSS in the spectrum obtained for ca. 16 nm thickness at $\overline{\Gamma}$ point. The blue and red project the wave function weight on core and surface atomic sites, respectively, while gray indicates the bulk-like intermediate sites. (b) and (c) illustrate the spatial distribution of localized Dirac-like core state (at p_1) and hybridized hinge-surface states (at p_2). Outlines denote the projected continuum bulk bands into 1DBZ edge given by dashed lines.

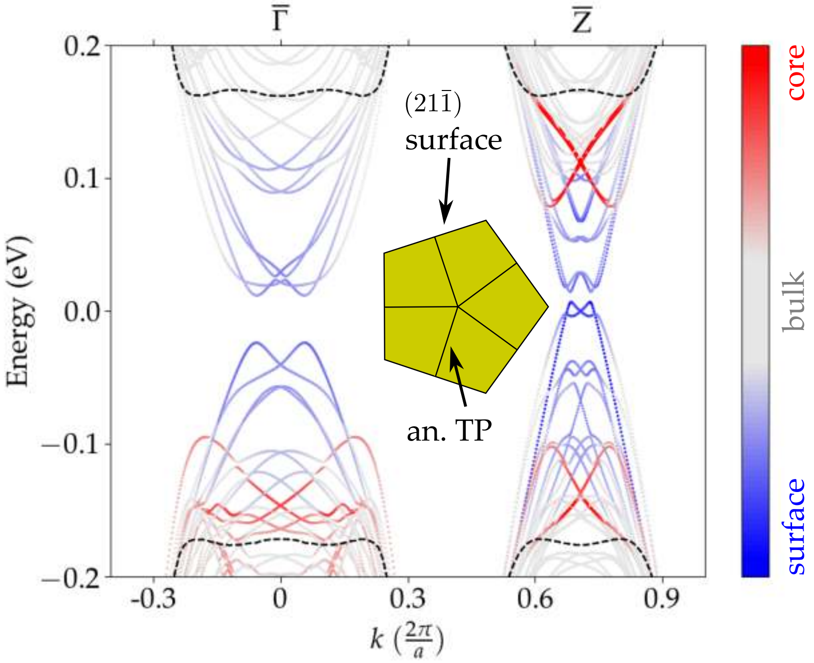

Figure 5.35: The electronic band structure of a SnTe pentagonal wire within $C_5 = -1$ subspace system. Inset: a schematic cross-section of a pentagonal NW, with $(21\bar{1})$ facets and anionic TPs located at the center of each surface. A topologically trivial (triv.) core state and hinge-surface states are observed in the spectrum obtained for a thickness of ca. 16 nm. The blue and red project the wave function weight on core and surface atomic sites, respectively. Dashed lines denote the top of valence and bottom of conduction bands in the continuum bulk.

showed that there exists a counterpart of core states on the hinges of the NWs belonging exclusively to the $C_5 = -1$ subspace. We noted that the Dirac modes associated with these hinges have little contribution from each of the $\{100\}$ facets. The emergence of quantized surface states in the middle of the bulk gap can be attributed to the global bulk nature of the system, wherein $\{110\}$ mirror plane symmetry exists. However, these states are gapped due to the confinement size of the NWs.

To uncover the source of the intersection effect, one can consider a scenario where the contribution of surface states to the hinge states is eliminated. To study, we impose perturbation Hamiltonian term to those atoms where located at the faces of pentagonal wire. This term locally breaks all relevant mirror symmetries, such as the $(01\bar{1})$ mirror symmetry (in each NW triangle), of the last atomic layer on the five (100) side surfaces, while preserving the C_5 rotational symmetry.

The presence of five-fold symmetrical disorders at the sides of the NWs allows us to observe five pairs of Dirac crossings in the gap that correspond to each of the C_5 subspaces, located at the five hinges. By introducing perturbations, we can push the initial surface states into the bulk of the NWs, effectively separating the hinge modes from the surface states and preventing any interference or mixing between the two. This enhances the emergence of well-localized hinge states, thereby providing valuable insights into the electronic properties of the NWs.

To break the five-fold degeneracy and observe the individual five hinges, we introduce onsite potentials at the five corners of the wire that are symmetric with respect to the global $(01\bar{1})$ mirror plane. This leads to a slight shift of nearly zero energy bands to the left and right, resulting in being symmetric with respect to $k = 0$, as depicted in Fig. 5.36.

5.4.1.6 Low-energy theory of the core and hinge states

In order to understand why we observe only one pair of hinge states instead of five, we model the electronic spectrum of the pentagonal wire using a low-energy theory of hinge states. We make the assumption that the low energy degrees of freedom are primarily determined by the edge physics of the twin planes. Therefore, in the case when the TPs are cationic, we must consider the core as the termination edge of five different two-dimensional topological insulators. The spectrum of such a core is a result of hybridization between five pairs of topological spin-polarized edge modes.

We begin our analysis by considering a perfectly symmetric NW with cationic TPs. The NW thickness is much larger than the localization length of twin-plane edge modes. Therefore, for five separated twin-plane edges, the spectrum would be simply a five-fold

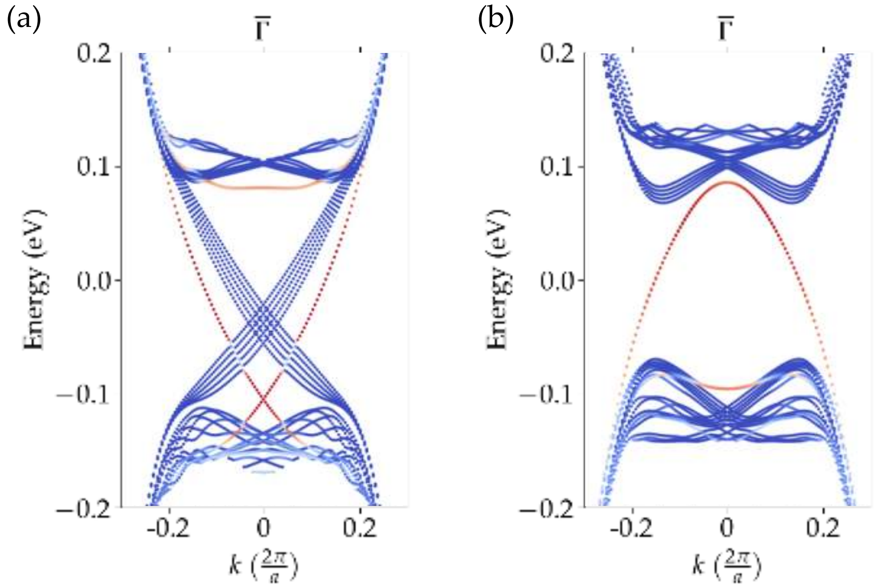

Figure 5.36: (a) Cationic twin plane, one Dirac crossing at the core (red) and five Dirac crossings at the hinges. (b) Anionic twin plane, no Dirac crossings become visible. The spectrum obtained for 14 nm (20 rings) thicknesses and the blue and red project the wave function weight on core and surface (including hinges) atomic sites, respectively

degenerate Dirac crossings, as each of the edges would host a pair of counter-propagating, oppositely spin-polarized modes. Thus, the appropriate basis to describe the core is five pairs of oppositely polarized spin-$\frac{1}{2}$ states.

The results of the 10-band symmetry analysis conducted by Rafał Rechciński prove that the spectrum within $\lambda = -1$ subspace is gapless and has non-degenerate states (depicted as black solid lines in Fig. 5.37) with linearly dispersing bands of opposite spin polarization. They are protected by five σ_v mirror plane symmetries parallel to the wire axis. In other subspaces, the states are mixed by five σ_v mirror planes and open the gap due to hybridization of one to another. These states are two-fold degenerate and are shown by dashed lines in Fig. 5.37.

Importantly, as long as the crossing in the $\lambda = -1$ is separated in energy from other bands, it cannot be opened by weak time-reversal-symmetry preserving perturbations of the wire. Therefore, exact crystalline symmetry is not necessary for the crossing to emerge.

The above analysis applies not just to the core states, but also to the hinge states. We interpret the hinge states as the edge modes of the twin planes, opposite to the ones that are localized near the core. In an ideal wire the symmetry group of the NW core and the NW surface is the same, and the symmetry transformations can be represented by the same matrices as for the core states. Hence, the form of the Hamiltonian of the hybridized

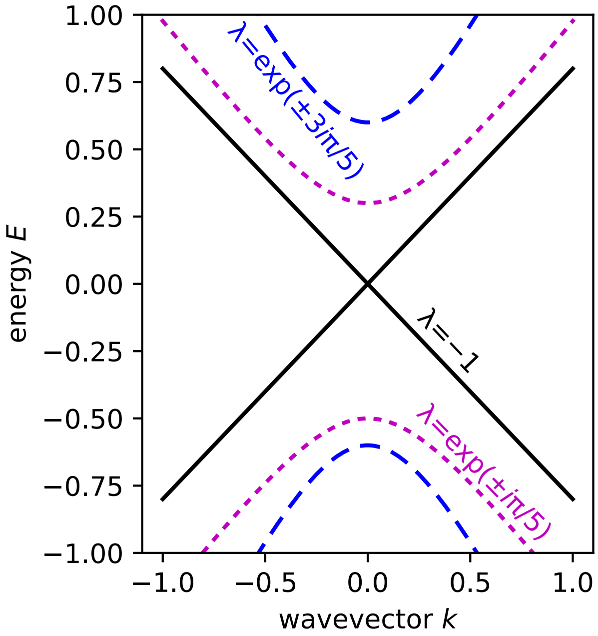

Figure 5.37: An example of the spectrum of the hybridized hinge (core) states in C_5-symmetric NWs. The solid black lines denote non-degenerate bands belonging to $\lambda = -1$ subspace of the C_5 operator. The dashed colored lines denote twice degenerate bands belonging to the remaining subspaces.

hinge states is the same as for the core states. We note, however, that while for the core states the hybridization is merely due to the close proximity of the five edges of the five twin planes, in the case of hinge states, the hybridization is mediated by the surface states that lie in the same energy and momentum range. Therefore, the hybridization does not vanish with increasing the NW thickness, but can be lifted by gapping out the surface states as demonstrated in Fig. 5.36.

It is crucial to highlight that the symmetry analysis mentioned earlier should also be applicable to the $\overline{\mathrm{Z}}$ point. However, the TB calculations reveal an anti-crossing behavior at the $\overline{\mathrm{Z}}$ point, with a visible gap even for significantly thick NWS. We intend to investigate this matter in future research to acquire a more profound understanding of the underlying cause behind the observed effect.

5.4.2 Square cross-section nanowires grown along [001] direction

In order to assess the effect of hybridization on edge proximity, we extend our investigation to a square cross-section NWs grown along the [001] crystallographic axis. Recent research has indicated the emergence of hinge modes in SnTe materials when examining the electronic band structures of cubic rocksalt NWs along the [001] axis [105]. Here,

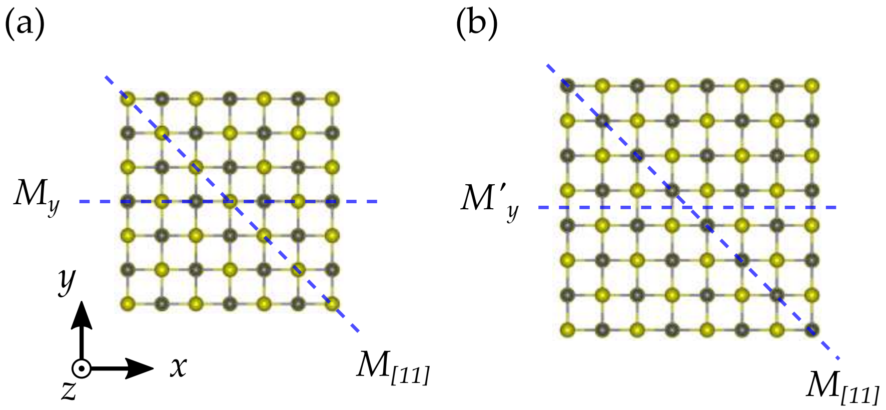

Figure 5.38: Cross-sections of [001]-oriented square NWs, taken along (001) atomic planes. Gray and yellow denote cations and anions, respectively. Panels (a) and (b) show the first and the second class of square NWs, respectively. M_y and $M_{[11]}$ denote selected mirror plane symmetries of the structures, while M'_y denotes a glide plane symmetry.

we will recover the electronic band structures of SnTe model and discuss hinge (edge) proximity effect for square cross-section NW.

There is a freedom to choose the atomic kind in the corner of square NWs which eventually gives rise to two different classes, namely, C_4 symmetry and 4_2 screw axis symmetry presented in Fig. 5.38. In the C_4 symmetric wires all corner atoms are the same species in a fixed (001) atomic plane. The NWs with second class (4_2 screw axis symmetry) in a fixed plane possess two opposing corners host cations, while the other two host anions. In [001]-oriented NWs all four L points from the 3DBZ are projected onto the edge of the 1DBZ at the $\overline{\text{Z}} = \pi/a(0,0,1)$ point. Its vicinity accommodates both the surface states localized on the NW faces, as well as hinge states, on which the following analysis is focused.

We used a TB model that exclusively considers p orbitals to perform electronic structure calculations for both the first (C_4) and second (4_2) classes of square nanowires (NWs) in the SnTe compound. These calculations were carried out for 41 (40) atomic thicknesses, and the results are presented in Fig. 5.39 and 5.40 for the first and second classes of NWs, respectively. Our findings demonstrate the presence of surface (hinge) states in the vicinity of $\overline{\text{Z}}$ with an open gap for both classes. Therefore, there are no nontrivial gapless modes within C_4-symmetric NWs due to hinge hybridization. However, as the thickness of the wire increases, the degree of hybridization gradually decreases. Consequently, each hinge can be treated as an isolated entity that is not influenced by others. For a sufficiently thick wire, the hinges will decouple and form four nearly degenerate topological hinge states protected by the bulk nature of the $\{110\}$ mirror plane symmetry, as shown in Fig.5.41 [17].

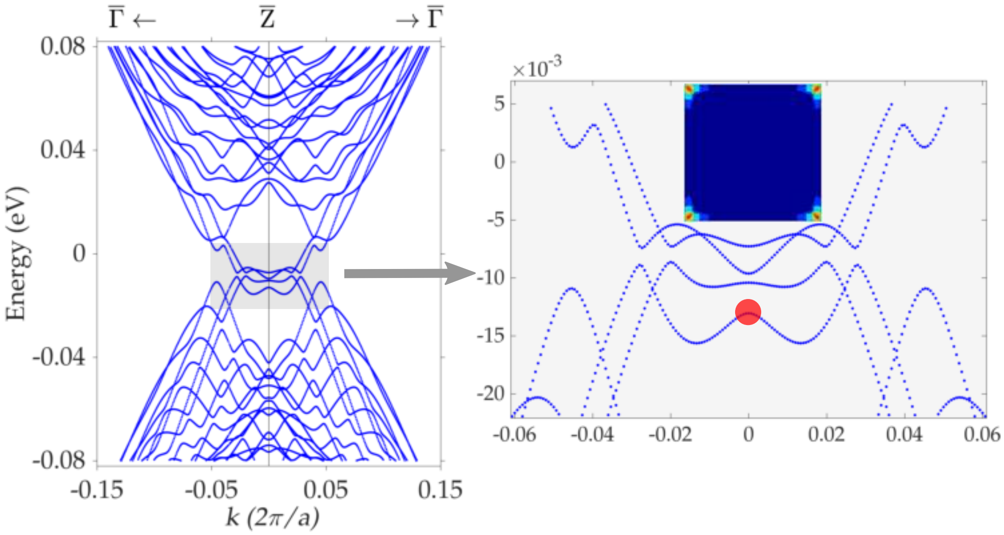

Figure 5.39: Band structure calculation of C_4-symmetric square SnTe NWs. The spectrum obtained by 41-atomic thickness. Right: The close-up view of shaded region (left) shown by local density of states denoted by red dot. The hybridization of hinges open the gap near $\overline{Z}$ point.

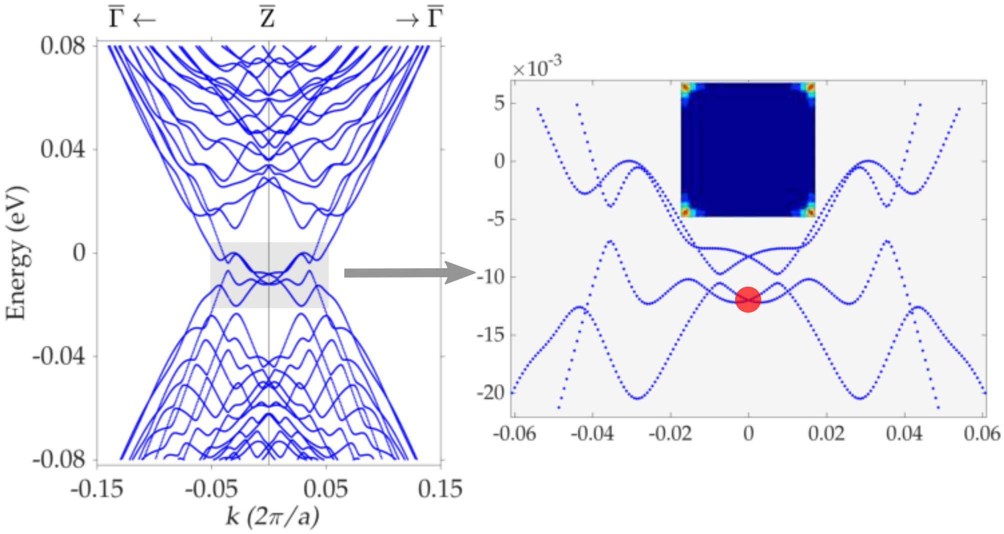

Figure 5.40: Band structure calculation of 4_2-screw-axis-symmetric square SnTe NWs. The spectrum obtained by 40-atomic thickness with alternative atomic types. Right: The close-up view of shaded region (left) shown by local density of states denoted by red dot. The hybridization of hinges open the gap near $\overline{Z}$ point.

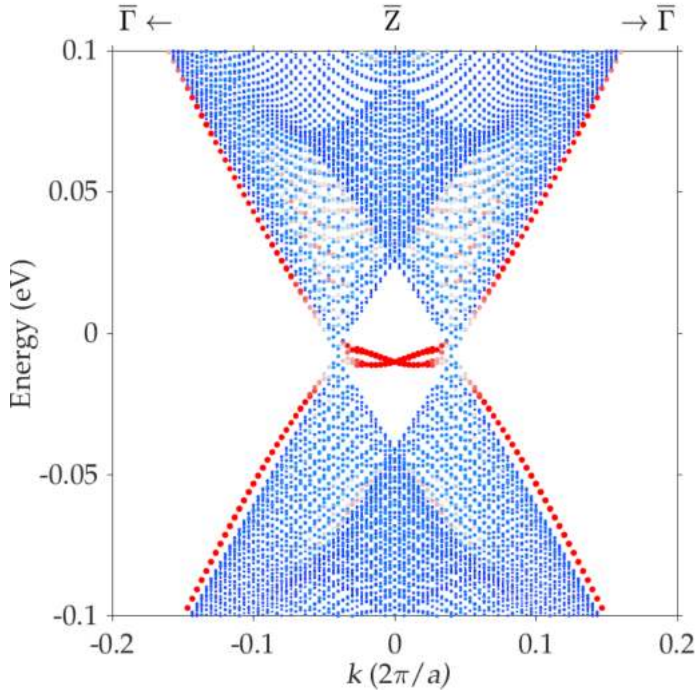

Figure 5.41: Band structure calculation of 4_2-screw-axis-symmetric square SnTe NWs. The spectrum obtained by 120-atomic thickness with alternative atomic type edges. Well-separated degenerate gapless hinge modes are revealed in the spectrum (red). In large enough thick wire each hinge can be treated as an isolated non-interacting edge.

We utilize $k.p$ analysis near the $\overline{Z}$ point to examine the impact of hybridization of four pairs of counter-propagating edge modes. Assuming that each NW hinge contains a pair of localized states at $\bar{Z}$ with opposite spin polarization, we select them as the basis and establish the gauge such that their wave function phase is zero at a hinge cation. The spectra of hybridized hinge states for C_4-symmetric square NWs and 4_2-screw-axis-symmetric square NWs are displayed in Fig. 5.42(a) and Fig. 5.42(b), respectively. The hybridization leads to a gapped Dirac spectrum for both classes where the full Hamiltonian features twice degenerate spectra for each band. We note that the resulting symmetry analysis is reliably corroborated with TB calculations in the vicinity of $\overline{Z}$ point. [5]

Based on TB calculations and complementary symmetry analysis, we can conclude that in systems with n-odd C_n rotation symmetry, such as a pentagonal wire, the hybridization effect of spin-polarized hinge states results in the existence of a single subspace with nondegenerate states. These states remained unaffected and are not mixed with other subspaces by the mirror plane σ_v. Conversely, in systems with n-even rotation symmetry, such as C_4, the Dirac spectrum becomes gapped, indicating hybridization with other symmetries.

---

[5] The low-energy analysis performed by Rafał Rechciński and the details are not included in the thesis.

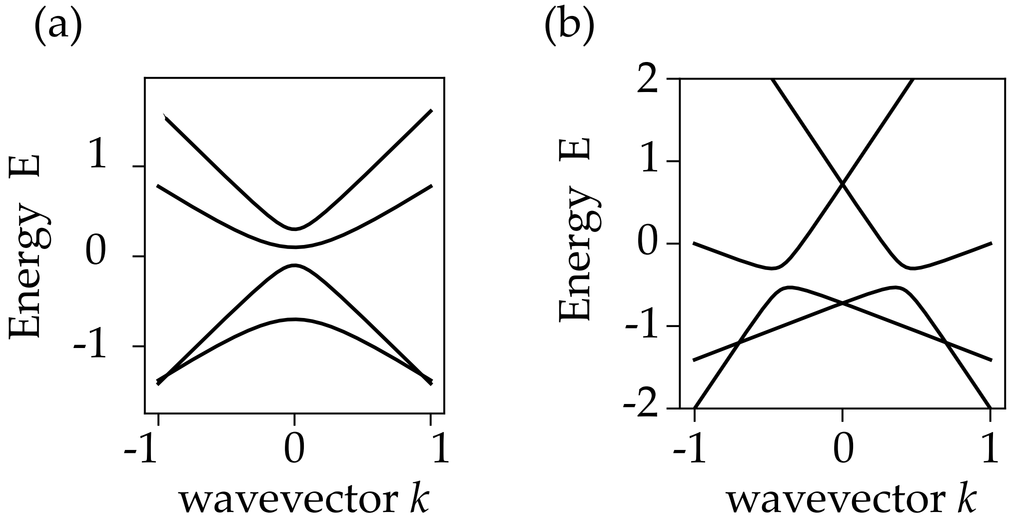

Figure 5.42: (a) Sample spectra of hybridized hinge states in C_4-symmetric square NWs. (b) Sample spectra of hybridized hinge states in 4_2-screw-axis-symmetric square NWs.

Chapter 6

Summary

In the present dissertation, within theoretical framework, the topological properties of selected geometry of IV-VI SnTe class of nanostructures were studied within tight binding approximation. Firstly, a comprehensive survey has been conducted on topological phenomena, accompanied by pedagogical examples, utilizing band theory. Second, the TB model presented based on the Slater-Koster approximation, providing the TB hopping parameters for both nearest and next nearest neighbors for various IV-VI rocksalt crystal structures. Subsequently, for each geometry explored in the study, an examination of topological properties was conducted through electronic band structure calculations. The recursive Green's spectral function method was employed to calculate spectra for a semi-infinite system. The corresponding topological invariants were presented for both 3D and 2D systems. In the case of the 1D system, however, a symmetry k.p analysis was provided.

In the first study, we expanded the research on the impact of lattice defects on the electronic structure topology to include TPs within a supercell framework. The theoretical analysis of the SnTe class of TCI materials demonstrates that a TP defect along the [111] direction functions as a 2D topological system protected by (111) mirror symmetry. The topological phases are exhibited through the (111) mirror Chern number, with the cationic TP featuring $C_m = 2$ and the anionic TP featuring $C_m = 1$. To further confirm the observed effect for a single twin boundary, a (111)-oriented slab with a single TP positioned at the center was considered. The slab is large enough to suppress any hybridization between states localized on the surfaces and on the TP. Nevertheless, the (111) surface of SnTe TCI exhibits gapless surface states, making it challenging to directly characterize the TP. To overcome this obstacle, both magnetic and non-magnetic surface perturbations are employed to induce the opening of the Dirac cones on the surfaces. It turns out that the topology of the entire slab relies on the topology of the incorporated TP. The $\{110\}$ mirror symmetry still exists in the structure while it is broken on top and bottom surface layers. It was shown that the topological invariants for a gapped surface states perfectly align with those obtained for the TSL systems. The topologically distinctive feature that sets apart the cationic and anionic TPs is attributed to the opposite sign of the Berry curvature observed around the Γ point in the 2D BZ. It has been proven that each type of TP forms the 2D mirror-plane-protected topological crystalline insulator. Performing similar calculations with the trivial compound (PbTe) reveals that the TP is topologically trivial in such case. This implies that the nontrivial properties of TPs stem from the introduction of a new mirror plane within an already topologically nontrivial bulk, where the bulk topology is determined by the inverted gap at the $\mathrm{L}^{\mathrm{fcc}}$ points.

Motivated by the experimental synthesis of pentagonal NWs $\mathrm{Pb}_{1-x}\mathrm{Sn}_x\mathrm{Te}$) with five $\{111\}$ twin boundaries in their cross-section, an investigation was carried out to examine the topological properties of these NWs. The study specifically focused on analyzing the influence of TPs on the NWs. It was shown that NWs with a pentagonal cross-section composed of SnTe class compounds harbor robust Dirac states within their core and corresponding states on their surfaces and hinges at $\overline{\Gamma}$ point. These states emerge only if the bulk topological phase of the compound is non-trivial and when the five twin planes dividing the NW segments are cationic. In n-odd C_n rotation symmetry, such as a pentagonal wire, the hybridization effect of spin-polarized hinge (core) states results in the existence of a single subspace with nondegenerate states. As a result, the core (hinge) supports only one, rather than five, Dirac crossing. In addition, the low-energy spectrum of the pentagonal NWs features surface states originating from the TCI phase of the bulk compound. For a sufficiently thick NW, say, 14 nm (35 nm) in case of SnTe ($\mathrm{Pb}_{0.6}\mathrm{Sn}_{0.4}\mathrm{Se}$), the core states are well separated in space from the surface bands. However, the hinge modes hybridize strongly with the surface bands which effectively couple the five hinges. Upon opening the surface gap by adding perturbation Hamiltonian to those atoms where located at the faces of wire, one can recover the five hinge modes. It was verified by low-energy theory that the Dirac modes are protected by the time-reversal symmetry and are therefore robust against non-magnetic disorder, imperfections and distortions of the crystalline structure.

In light of the influence exerted by a TP on the topological phases in the previously mentioned systems, we proceeded to explore the effect of TP in the realm of ultrathin films. The topological phase transition was determined through $\mathbb{Z}_2$ invariant and (111) mirror Chern number, which ranged from 3 to 60 for films with an odd number of atomic heights. We have shown that TP topology combined with finite-size effects influence how the topological invariants change with growing film thickness in comparison with previously studied (111)-SnTe films without TP.

The promising findings of these studies call for further research both in simulation and experiment. It is especially interesting to determine what is the energetically favourable kind of twin boundaries can be observed in experiment, and whether it can be controlled by growth conditions. Further studies are needed also to assess which of the SnTe class compounds and solid solutions can form stable NW and TSL structures in the presence of TPs. The current theoretical studies propose to possible measurement of transport properties of the topological materials in different geometries studied in this thesis.

Appendix A

TP and TSLs

A.1 Electronic structures along high-symmetry lines in ALH plane

To corroborate the findings presented in section 5.1, we conducted a further investigation into the electronic structures of cat-cat/an-an TSLs along different paths in the 3DBZ. Specifically, we examined the spectra of cat-cat/an-an TSLs along the A-L-H-A high-symmetry lines, as illustrated in Fig. A.1, for a 200-monolayer supercell height [133]. The structures observed were highly similar to those obtained in the ΓMK plane for each type of TSL. Notably, the states localized in the vicinity of the TPs, indicated by the color red in the figure, exhibited the same dispersion as in the ΓMK plane. However, as shown in Table 5.1, the calculated mirror Chern numbers were distinct between ΓMK and ALH, and were found to be zero in the latter plane for TSLs containing the same type of TPs.

This result arises from the fact that upon mirror reflection, the wave functions corresponding to the ALH plane acquire a phase difference of -1 between the two TPs present in the supercell, rendering this plane trivial for cat-cat/an-an TSLs.

A.2 Projection rule of M points in arbitrary edge of the 2D hexagonal lattice

Here, we present a general principle to determine whether the Γ point and M points are always paired in any crystallographic direction. It is important to note that the same principle also applies to the A and L points. To construct infinitely periodic lattices in real space, we define the 2D primitive lattice vectors as $\vec{t}_1 = a(0, \sqrt{3})$ and $\vec{t}_2 = a\left(\frac{3}{2}, \frac{\sqrt{3}}{2}\right)$. The corresponding reciprocal lattice vectors are $\vec{b}_1 = \frac{2\pi}{a}\left(-\frac{1}{3}, \frac{\sqrt{3}}{3}\right)$ and $\vec{b}_2 = \frac{2\pi}{a}\left(\frac{2}{3}, 0\right)$, which

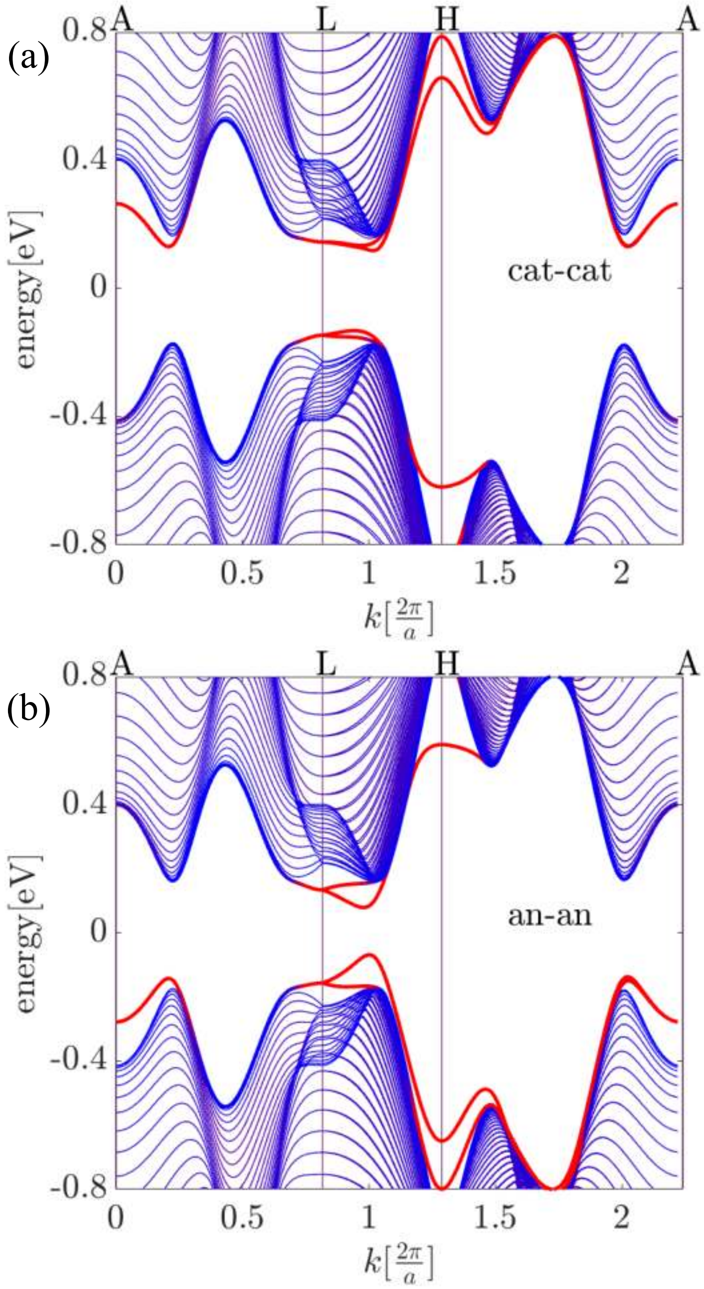

Figure A.1: Band structures of 200-monolayer-height [111]-oriented SnTe TSLs along the A-L-H-A high-symmetry lines of the 3DBZ. The TSLs are created with either all-cationic or all-anionic TPs, and the color scale from red to blue represents the degree of wave function localization on the TPs and bulk-like atoms [133]. Copyright (2023) by the American Physical Society.

define a 2D hexagonal BZ. The net vectors of the M_i points ($i = 1, 2, 3$) and the Γ point are defined as follows [133]:

$$\Gamma = \vec{G}\,, \tag{A.1}$$

$$\vec{M}_1 = \frac{1}{2}(\vec{b}_1 + \vec{b}_2) + \vec{G}\,, \tag{A.2}$$

$$\vec{M}_2 = \frac{1}{2}\vec{b}_2 + \vec{G}\,, \tag{A.3}$$

$$\vec{M}_3 = -\frac{1}{2}\vec{b}_1 + \vec{G}\,. \tag{A.4}$$

The direction of projection, denoted as $\vec{d}$, is determined by $\vec{d} = -p\vec{t}_1 + q\vec{t}2$. This direction is perpendicular to the $\vec{d}_\perp = p\vec{b}_2 + q\vec{b}_1$, where $\vec{G}$ represents the reciprocal net vector $n'\vec{b}_1 + m'\vec{b}_2$, and n' and m' are integers. It is important to mention that the edge indices (p, q) need to be coprime. To achieve the projection in pairs, the following conditions must be satisfied

$$(\vec{M}_i - \vec{M}_j) \cdot \vec{d}_\perp = 0, \qquad \text{(pair of } M \text{ points)}, \tag{A.5}$$

$$\vec{M}_k \cdot \vec{d}_\perp = 0, \qquad \text{(pair of } \Gamma \text{ \& } M \text{ points)}. \tag{A.6}$$

Through the analysis of all possible combinations of M points and leveraging the characteristics of coprime edge indices (p, q), it can be observed that the Γ point and the three M points are consistently projected into two distinct pairs, as follows:

1. (M_2, M_3) and (Γ, M_1), when both p and q are odd.
2. (M_1, M_2) and (Γ, M_3), when p is even and q is odd.
3. (M_1, M_3) and (Γ, M_2), when p is odd and q is even.

Bibliography

[1] K. v. Klitzing, G. Dorda, and M. Pepper, “New method for high-accuracy determination of the fine-structure constant based on quantized Hall resistance”, Phys. Rev. Lett. **45**, 494–497 (1980).

[2] D. J. Thouless, M. Kohmoto, M. P. Nightingale, and M. den Nijs, “Quantized Hall conductance in a two-dimensional periodic potential”, Phys. Rev. Lett. **49**, 405–408 (1982).

[3] F. D. M. Haldane, “Model for a quantum Hall effect without landau levels: condensed-matter realization of the "parity anomaly"”, Phys. Rev. Lett. **61**, 2015–2018 (1988).

[4] D. Hsieh, D. Qian, L. Wray, Y. Xia, Y. S. Hor, R. J. Cava, and M. Z. Hasan, “A topological dirac insulator in a quantum spin Hall phase”, Nature **452**, 970–974 (2008).

[5] H. Zhang, C.-X. Liu, X.-L. Qi, X. Dai, Z. Fang, and S.-C. Zhang, “Topological insulators in Bi_2Se_3, Bi_2Te_3 and Sb_2Te_3 with a single Dirac cone on the surface”, Nature physics **5**, 438–442 (2009).

[6] Y. Xia, D. Qian, D. Hsieh, L Wray, A. Pal, H. Lin, A. Bansil, D. Grauer, Y. S. Hor, R. J. Cava, et al., “Observation of a large-gap topological-insulator class with a single dirac cone on the surface”, Nature physics **5**, 398–402 (2009).

[7] T. H. Hsieh, H. Lin, J. Liu, W. Duan, A. Bansil, and L. Fu, “Topological crystalline insulators in the SnTe material class”, Nat. Commun. **3**, 982 (2012).

[8] Y. Tanaka, T. Shoman, K. Nakayama, S. Souma, T. Sato, T. Takahashi, M. Novak, K. Segawa, and Y. Ando, “Two types of Dirac-cone surface states on the (111) surface of the topological crystalline insulator SnTe”, Phys. Rev. B **88**, 235126 (2013).

[9] S.-Y. Xu, C. Liu, N Alidoust, M Neupane, D Qian, I Belopolski, J. Denlinger, Y. Wang, H Lin, L. a. Wray, et al., “Observation of a topological crystalline insulator phase and topological phase transition in $Pb_{1-x}Sn_xTe$”, Nat. Commun. **3**, 1192 (2012).

[10] P Dziawa, B. Kowalski, K Dybko, R Buczko, A Szczerbakow, M Szot, E Łusakowska, T Balasubramanian, B. M. Wojek, M. Berntsen, et al., “Topological crystalline insulator states in $Pb_{1-x}Sn_xSe$”, Nat. Mater. **11**, 1023 (2012).

[11] S. Safaei, M. Galicka, P. Kacman, and R. Buczko, "Quantum spin Hall effect in IV-VI topological crystalline insulators", New J. Phys. **17**, 063041 (2015).

[12] J. Liu and L. Fu, "Electrically tunable quantum spin Hall state in topological crystalline insulator thin films", Phys. Rev. B **91**, 081407 (2015).

[13] J. Liu, T. H. Hsieh, P. Wei, W. Duan, J. Moodera, and L. Fu, "Spin-filtered edge states with an electrically tunable gap in a two-dimensional topological crystalline insulator", Nat. mater. **13**, 178–183 (2014).

[14] P. Sessi, D. D. Sante, A. Szczerbakow, F. Glott, S. Wilfert, H. Schmidt, T. Bathon, P. Dziawa, M. Greiter, T. Neupert, G. Sangiovanni, T. Story, R. Thomale, and M. Bode, "Robust spin-polarized midgap states at step edges of topological crystalline insulators", Science **354**, 1269–1273 (2016).

[15] R. Rechciński and R. Buczko, "Topological states on uneven (Pb, Sn) Se (001) surfaces", Physical Review B **98**, 245302 (2018).

[16] W. Brzezicki, M. M. Wysokiński, and T. Hyart, "Topological properties of multilayers and surface steps in the SnTe material class", Physical Review B **100**, 121107 (2019).

[17] F. Schindler, A. M. Cook, M. G. Vergniory, Z. Wang, S. S. Parkin, B. A. Bernevig, and T. Neupert, "Higher-order topological insulators", Sci. Adv. **4**, eaat0346 (2018).

[18] Y. Ando and L. Fu, "Topological crystalline insulators and topological superconductors: from concepts to materials", Annual Review of Condensed Matter Physics **6**, 361–381 (2015).

[19] M. A. Brzezińska, "Beyond the ten-fold way: novel topological phases in low-dimensional systems", PhD thesis (Wroclow univeristy of science, 2020) Chap. 1.

[20] M. Nakahara, *Geometry, topology and physics* (CRC press, 2018).

[21] J Cayssol and J. N. Fuchs, "Topological and geometrical aspects of band theory", Journal of Physics: Materials **4**, 034007 (2021).

[22] J. K. Asbóth, L. Oroszlány, and A. Pályi, "A short course on topological insulators", Lecture notes in physics **919**, 166 (2016).

[23] R. Jackiw and C. Rebbi, "Solitons with fermion number ½", Phys. Rev. D **13**, 3398–3409 (1976).

[24] E. Fradkin, E. Dagotto, and D. Boyanovsky, "Physical realization of the parity anomaly in condensed matter physics", Phys. Rev. Lett. **57**, 2967–2970 (1986).

[25] D. B. Kaplan, "A method for simulating chiral fermions on the lattice", Physics Letters B **288**, 342–347 (1992).

[26] G. E. Volovik, *The universe in a helium droplet*, Vol. 117 (OUP Oxford, 2003).

[27] H. Nielsen and M. Ninomiya, "The Adler-Bell-Jackiw anomaly and Weyl fermions in a crystal", Physics Letters B **130**, 389–396 (1983).

[28] J. Kellendonk, T. Richter, and H. Schulz-Baldes, "Edge current channels and CHERN numbers in the integer quantum Hall effect", Reviews in Mathematical Physics **14**, 87–119 (2002).

[29] T. Fukui, K. Shiozaki, T. Fujiwara, and S. Fujimoto, "Bulk-edge correspondence for Chern topological phases: a viewpoint from a generalized index theorem", Journal of the Physical Society of Japan **81**, 114602 (2012).

[30] G. M. Graf and M. Porta, "Bulk-edge correspondence for two-dimensional topological insulators", Communications in Mathematical Physics **324**, 851–895 (2013).

[31] E. Prodan and H. Schulz-Baldes, *Bulk and boundary invariants for complex topological insulators* (Springer, 2016).

[32] J. C. Y. Teo and C. L. Kane, "Topological defects and gapless modes in insulators and superconductors", Phys. Rev. B **82**, 115120 (2010).

[33] F. Schindler, A. M. Cook, M. G. Vergniory, Z. Wang, S. S. P. Parkin, B. A. Bernevig, and T. Neupert, "Higher-order topological insulators", Science Advances **4**, eaat0346 (2018).

[34] M. V. Berry, "Quantal phase factors accompanying adiabatic changes", Proceedings of the Royal Society of London. A. Mathematical and Physical Sciences **392**, 45–57 (1984).

[35] D. Xiao, M.-C. Chang, and Q. Niu, "Berry phase effects on electronic properties", Rev. Mod. Phys. **82**, 1959–2007 (2010).

[36] T. Kato, "On the adiabatic theorem of quantum mechanics", Journal of the Physical Society of Japan **5**, 435–439 (1950).

[37] A. Messiah, *Quantum mechanics, vol ii* (North Holland Publishing Company, Amsterdam, 1962).

[38] Y. Aharonov and D. Bohm, "Significance of electromagnetic potentials in the quantum theory", Phys. Rev. **115**, 485–491 (1959).

[39] F. Wilczek and A. Zee, "Appearance of gauge structure in simple dynamical systems", Phys. Rev. Lett. **52**, 2111–2114 (1984).

[40] J. Zak, "Berry's phase for energy bands in solids", Phys. Rev. Lett. **62**, 2747–2750 (1989).

[41] F. Bloch, "Über die quantenmechanik der elektronen in kristallgittern", Zeitschrift für physik **52**, 555–600 (1929).

[42] K. von Klitzing, "Developments in the quantum Hall effect", Philosophical Transactions of the Royal Society A: Mathematical, Physical and Engineering Sciences **363**, 2203–2219 (2005).

[43] R. B. Laughlin, "Quantized Hall conductivity in two dimensions", Phys. Rev. B **23**, 5632–5633 (1981).

[44] J. E. Avron, R. Seiler, and B. Simon, “Homotopy and quantization in condensed matter physics”, Phys. Rev. Lett. **51**, 51–53 (1983).

[45] C.-X. Liu, X.-L. Qi, X. Dai, Z. Fang, and S.-C. Zhang, “Quantum anomalous hall effect in $Hg_{1-y}Mn_yTe$ quantum wells”, Phys. Rev. Lett. **101**, 146802 (2008).

[46] Q.-Z. Wang, X. Liu, H.-J. Zhang, N. Samarth, S.-C. Zhang, and C.-X. Liu, “Quantum anomalous hall effect in magnetically doped inas/gasb quantum wells”, Phys. Rev. Lett. **113**, 147201 (2014).

[47] C.-Z. Chang, J. Zhang, X. Feng, J. Shen, Z. Zhang, M. Guo, K. Li, Y. Ou, P. Wei, L.-L. Wang, Z.-Q. Ji, Y. Feng, S. Ji, X. Chen, J. Jia, X. Dai, Z. Fang, S.-C. Zhang, K. He, Y. Wang, L. Lu, X.-C. Ma, and Q.-K. Xue, “Experimental observation of the quantum anomalous Hall effect in a magnetic topological insulator”, Science **340**, 167–170 (2013).

[48] X.-L. Qi, Y.-S. Wu, and S.-C. Zhang, “Topological quantization of the spin Hall effect in two-dimensional paramagnetic semiconductors”, Phys. Rev. B **74**, 085308 (2006).

[49] B. A. Bernevig, in *Topological insulators and topological superconductors* (Princeton university press, 2013).

[50] M. C. Chang, *Lecture notes on topological insulators*, `https://phy.ntnu.edu.tw/~changmc/Teach/Topo/Topo.html`.

[51] C. L. Kane and E. J. Mele, “Quantum spin Hall effect in graphene”, Phys. Rev. Lett. **95**, 226801 (2005).

[52] C. L. Kane and E. J. Mele, “Z_2 Topological order and the quantum spin Hall effect”, Phys. Rev. Lett. **95**, 146802 (2005).

[53] B. A. Bernevig and S.-C. Zhang, “Quantum spin Hall effect”, Phys. Rev. Lett. **96**, 106802 (2006).

[54] B. A. Bernevig, T. L. Hughes, and S.-C. Zhang, “Quantum spin Hall effect and topological phase transition in HgTe quantum wells”, Science **314**, 1757–1761 (2006).

[55] M. König, S. Wiedmann, C. Brüne, A. Roth, H. Buhmann, L. W. Molenkamp, X.-L. Qi, and S.-C. Zhang, “Quantum spin Hall insulator state in HgTe quantum wells”, Science **318**, 766–770 (2007).

[56] M. König, H. Buhmann, L. W. Molenkamp, T. Hughes, C.-X. Liu, X.-L. Qi, and S.-C. Zhang, “The quantum spin Hall effect: theory and experiment”, Journal of the Physical Society of Japan **77**, 031007 (2008).

[57] C. Xu and J. E. Moore, “Stability of the quantum spin Hall effect: effects of interactions, disorder, and $\mathbb{Z}_2$ topology”, Phys. Rev. B **73**, 045322 (2006).

[58] L. Fu and C. L. Kane, “Time reversal polarization and a Z_2 adiabatic spin pump”, Phys. Rev. B **74**, 195312 (2006).

[59] L. Fu and C. L. Kane, “Topological insulators with inversion symmetry”, Phys. Rev. B **76**, 045302 (2007).

[60] T. Fukui and Y. Hatsugai, “Quantum Spin Hall Effect in Three Dimensional Materials: Lattice Computation of Z_2 Topological Invariants and Its Application to Bi and Sb”, Journal of the Physical Society of Japan **76**, 053702 (2007).

[61] T. Fukui, T. Fujiwara, and Y. Hatsugai, “Topological meaning of Z_2 numbers in time reversal invariant systems”, Journal of the Physical Society of Japan **77**, 123705 (2008).

[62] R. Roy, “Z_2 Classification of quantum spin Hall systems: an approach using time-reversal invariance”, Phys. Rev. B **79**, 195321 (2009).

[63] X.-L. Qi, T. L. Hughes, and S.-C. Zhang, “Topological field theory of time-reversal invariant insulators”, Phys. Rev. B **78**, 195424 (2008).

[64] T. Fukui, Y. Hatsugai, and H. Suzuki, “Chern numbers in discretized Brillouin zone: efficient method of computing (spin) Hall conductances”, Journal of the Physical Society of Japan **74**, 1674–1677 (2005).

[65] M. P. L. Sancho, J. M. L. Sancho, J. M. L. Sancho, and J Rubio, “Highly convergent schemes for the calculation of bulk and surface Green functions”, J. Phys. F: Met. Phys. **15**, 851–858 (1985).

[66] L. Fu, C. L. Kane, and E. J. Mele, “Topological insulators in three dimensions”, Phys. Rev. Lett. **98**, 106803 (2007).

[67] J. E. Moore and L. Balents, “Topological invariants of time-reversal-invariant band structures”, Phys. Rev. B **75**, 121306 (2007).

[68] R. Roy, “Characterization of three-dimensional topological insulators by two-dimensional invariants”, New Journal of Physics **12**, 065009 (2010).

[69] E. Prodan, “Robustness of the spin-Chern number”, Phys. Rev. B **80**, 125327 (2009).

[70] D. Hsieh, Y. Xia, D. Qian, L Wray, J. Dil, F. Meier, J Osterwalder, L Patthey, J. Checkelsky, N. P. Ong, et al., “A tunable topological insulator in the spin helical dirac transport regime”, Nature **460**, 1101–1105 (2009).

[71] L. Fu, “Topological crystalline insulators”, Phys. Rev. Lett. **106**, 106802 (2011).

[72] T. Neupert and F. Schindler, in *Topological matter* (Springer International Publishing, 2018), pp. 31–61.

[73] Y Tanaka, Z. Ren, T Sato, K Nakayama, S Souma, T Takahashi, K. Segawa, and Y. Ando, “Experimental realization of a topological crystalline insulator in SnTe”, Nat. Phys. **8**, 800 (2012).

[74] J. C. Y. Teo, L. Fu, and C. L. Kane, “Surface states and topological invariants in three-dimensional topological insulators: Application to $\mathrm{Bi}_{1-x}\mathrm{Sb}_x$”, Phys. Rev. B **78**, 045426 (2008).

[75] J. Liu, “A short review on first-principles study of gapped topological materials”, Computational Materials Science **195**, 110467 (2021).

[76] V. Sukhovatkin, S. Hinds, L. Brzozowski, and E. H. Sargent, “Colloidal quantum-dot photodetectors exploiting multiexciton generation”, Science **324**, 1542–1544 (2009).

[77] E. H. Sargent, “Infrared photovoltaics made by solution processing”, Nat. Photon. **3**, 325–331 (2009).

[78] O. E. Semonin, J. M. Luther, S. Choi, H.-Y. Chen, J. Gao, A. J. Nozik, and M. C. Beard, “Peak external photocurrent quantum efficiency exceeding 100% via MEG in a quantum dot solar cell”, Science **334**, 1530–1533 (2011).

[79] D. Hsieh, Y. Xia, L. Wray, D. Qian, A. Pal, J. H. Dil, J. Osterwalder, F. Meier, G. Bihlmayer, C. L. Kane, Y. S. Hor, R. J. Cava, and M. Z. Hasan, “Observation of unconventional quantum spin textures in topological insulators”, Science **323**, 919–922 (2009).

[80] J. Dimmock, I. Melngailis, and A. Strauss, “Band structure and laser action in $\mathrm{Pb_xSn_{1-x}Te}$”, Physical Review Letters **16**, Cited by: 346, 1193 – 1196 (1966).

[81] J. Liu, W. Duan, and L. Fu, “Two types of surface states in topological crystalline insulators”, Phys. Rev. B **88**, 241303 (2013).

[82] R. Buczko and P. Kacman, “Comment on “tuning topological surface states by cleavage angle in topological crystalline insulators””, Phys. Rev. B **101**, 157103 (2020).

[83] S. Safaei, P. Kacman, and R. Buczko, “Topological crystalline insulator (Pb,Sn)Te: Surface states and their spin polarization”, Phys. Rev. B **88**, 045305 (2013).

[84] C. M. Polley, P. Dziawa, A. Reszka, A. Szczerbakow, R. Minikayev, J. Z. Domagala, S. Safaei, P. Kacman, R. Buczko, J. Adell, M. H. Berntsen, B. M. Wojek, O. Tjernberg, B. J. Kowalski, T. Story, and T. Balasubramanian, “Observation of topological crystalline insulator surface states on (111)-oriented $\mathrm{Pb}_{1-x}\mathrm{Sn}_x\mathrm{Se}$ films”, Phys. Rev. B **89**, 075317 (2014).

[85] C. Yan, J. Liu, Y. Zang, J. Wang, Z. Wang, P. Wang, Z.-D. Zhang, L. Wang, X. Ma, S. Ji, K. He, L. Fu, W. Duan, Q.-K. Xue, and X. Chen, “Experimental observation of dirac-like surface states and topological phase transition in $\mathrm{Pb}_{1-x}\mathrm{Sn}_x\mathrm{Te}(111)$ films”, Phys. Rev. Lett. **112**, 186801 (2014).

[86] M. Z. Hasan, S.-Y. Xu, and M. Neupane, “Topological insulators, topological crystalline insulators, topological semimetals and topological kondo insulators”, arXiv preprint arXiv:1406.1040 (2014).

[87] Y. Okada, M. Serbyn, H. Lin, D. Walkup, W. Zhou, C. Dhital, M. Neupane, S. Xu, Y. J. Wang, R. Sankar, F. Chou, A. Bansil, M. Z. Hasan, S. D. Wilson, L. Fu, and

V. Madhavan, “Observation of dirac node formation and mass acquisition in a topological crystalline insulator”, Science **341**, 1496–1499 (2013).

[88] M. Neupane, S.-Y. Xu, R. Sankar, N. Alidoust, G. Bian, C. Liu, I. Belopolski, T.-R. Chang, H.-T. Jeng, H. Lin, et al., “Observation of a three-dimensional topological dirac semimetal phase in high-mobility Cd_3As_2”, Nature communications **5**, 3786 (2014).

[89] I. Zeljkovic, Y. Okada, C.-Y. Huang, R. Sankar, D. Walkup, W. Zhou, M. Serbyn, F. Chou, W.-F. Tsai, H. Lin, et al., “Mapping the unconventional orbital texture in topological crystalline insulators”, Nature Physics **10**, 572–577 (2014).

[90] A Gyenis, I. Drozdov, S Nadj-Perge, O. Jeong, J Seo, I Pletikosić, T Valla, G. Gu, and A. Yazdani, “Quasiparticle interference on the surface of the topological crystalline insulator Pb_{1-x} Sn $_x$ Se”, Physical Review B **88**, 125414 (2013).

[91] T. Liang, Q. Gibson, J. Xiong, M. Hirschberger, S. P. Koduvayur, R. J. Cava, and N. P. Ong, “Evidence for massive bulk dirac fermions in $Pb_{1-x}Sn_xSe$ from nernst and thermopower experiments”, Nature communications **4**, 2696 (2013).

[92] B. M. Wojek, R. Buczko, S. Safaei, P. Dziawa, B. J. Kowalski, M. H. Berntsen, T. Balasubramanian, M. Leandersson, A. Szczerbakow, P. Kacman, T. Story, and O. Tjernberg, “Spin-polarized (001) surface states of the topological crystalline insulator $Pb_{0.73}Sn_{0.27}Se$”, Phys. Rev. B **87**, 115106 (2013).

[93] Y. J. Wang, W.-F. Tsai, H. Lin, S.-Y. Xu, M. Neupane, M. Z. Hasan, and A. Bansil, “Nontrivial spin texture of the coaxial dirac cones on the surface of topological crystalline insulator SnTe”, Phys. Rev. B **87**, 235317 (2013).

[94] I. Pletikosić, G. D. Gu, and T. Valla, “Inducing a lifshitz transition by extrinsic doping of surface bands in the topological crystalline insulator $Pb_{1-x}Sn_xSe$”, Physical Review Letters **112**, 146403 (2014).

[95] H. Ozawa, A. Yamakage, M. Sato, and Y. Tanaka, “Topological phase transition in a topological crystalline insulator induced by finite-size effects”, Phys. Rev. B **90**, 045309 (2014).

[96] C. Fang, M. J. Gilbert, and B. A. Bernevig, “Large-chern-number quantum anomalous Hall effect in thin-film topological crystalline insulators”, Phys. Rev. Lett. **112**, 046801 (2014).

[97] M. Serbyn and L. Fu, “Symmetry breaking and landau quantization in topological crystalline insulators”, Phys. Rev. B **90**, 035402 (2014).

[98] E. Tang and L. Fu, “Strain-induced partially flat band, helical snake states and interface superconductivity in topological crystalline insulators”, Nature Physics **10**, 964–969 (2014).

[99] A. W. W. Ludwig, M. P. A. Fisher, R. Shankar, and G. Grinstein, “Integer quantum Hall transition: an alternative approach and exact results”, Phys. Rev. B **50**, 7526–7552 (1994).

[100] L. Fu and C. L. Kane, “Topology, delocalization via average symmetry and the symplectic anderson transition”, Phys. Rev. Lett. **109**, 246605 (2012).

[101] M. Geier, L. Trifunovic, M. Hoskam, and P. W. Brouwer, “Second-order topological insulators and superconductors with an order-two crystalline symmetry”, Phys. Rev. B **97**, 205135 (2018).

[102] W. A. Benalcazar, B. A. Bernevig, and T. L. Hughes, “Quantized electric multipole insulators”, Science **357**, 61–66 (2017).

[103] W. A. Benalcazar, B. A. Bernevig, and T. L. Hughes, “Electric multipole moments, topological multipole moment pumping, and chiral hinge states in crystalline insulators”, Phys. Rev. B **96**, 245115 (2017).

[104] F. Schindler, Z. Wang, M. G. Vergniory, A. M. Cook, A. Murani, S. Sengupta, A. Y. Kasumov, R. Deblock, S. Jeon, I. Drozdov, et al., “Higher-order topology in bismuth”, Nat. Phys. **14**, 918–924 (2018).

[105] N. M. Nguyen, W. Brzezicki, and T. Hyart, “Corner states, hinge states, and majorana modes in SnTe nanowires”, Phys. Rev. B **105**, 075310 (2022).

[106] R. M. Skiff, F. de Juan, R. Queiroz, S. Mathimalar, H. Beidenkopf, and R. Ilan, “Confined vs. extended Dirac surface states in topological crystalline insulator nanowires”, SciPost Phys. Core **6**, 011 (2023).

[107] H. C. Po, A. Vishwanath, and H. Watanabe, “Symmetry-based indicators of band topology in the 230 space groups”, Nature communications **8**, 50 (2017).

[108] E. Khalaf, H. C. Po, A. Vishwanath, and H. Watanabe, “Symmetry indicators and anomalous surface states of topological crystalline insulators”, Phys. Rev. X **8**, 031070 (2018).

[109] Z. Song, T. Zhang, Z. Fang, and C. Fang, “Quantitative mappings between symmetry and topology in solids”, Nature communications **9**, 3530 (2018).

[110] T. Zhang, Y. Jiang, Z. Song, H. Huang, Y. He, Z. Fang, H. Weng, and C. Fang, “Catalogue of topological electronic materials”, Nature **566**, 475–479 (2019).

[111] M.-C. Jung, K.-W. Lee, and W. E. Pickett, “Perovskite $\mathbf{ThTaN_3}$: a large-thermopower topological crystalline insulator”, Phys. Rev. B **97**, 121104 (2018).

[112] T. H. Hsieh, J. Liu, and L. Fu, “Topological crystalline insulators and Dirac octets in antiperovskites”, Phys. Rev. B **90**, 081112 (2014).

[113] X. Zhou, C.-H. Hsu, T.-R. Chang, H.-J. Tien, Q. Ma, P. Jarillo-Herrero, N. Gedik, A. Bansil, V. M. Pereira, S.-Y. Xu, H. Lin, and L. Fu, “Topological crystalline insulator states in the Ca_2As family”, Phys. Rev. B **98**, 241104 (2018).

[114] F. Tang, H. C. Po, A. Vishwanath, and X. Wan, "Comprehensive search for topological materials using symmetry indicators", Nature **566**, 486–489 (2019).

[115] J. C. Slater and G. F. Koster, "Simplified LCAO method for the periodic potential problem", Phys. Rev. **94**, 1498–1524 (1954).

[116] S. Safaei, "The properties of the topological crystalline insulator surface states-theoretical analysis", PhD thesis (Institute of Physics, Polish Academy of Sciences, 2015).

[117] P. Löwdin, "On the non-orthogonality problem connected with the use of atomic wave functions in the theory of molecules and crystals", The Journal of Chemical Physics **18**, 365–375 (1950).

[118] D. A. Papaconstantopoulos and M. J. Mehl, "The Slater–Koster tight-binding method: a computationally efficient and accurate approach", Journal of Physics: Condensed Matter **15**, R413 (2003).

[119] T. Rauch, "Topological insulators and semimetals: theory for bulk and surface electronic properties", PhD thesis (Martin-Luther-Universitat Halle-Wittenberg, 2016).

[120] M. Jaffe and J. Singh, "Inclusion of spin-orbit coupling into tight binding band structure calculations for bulk and superlattice semiconductors", Solid State Communications **62**, 399–402 (1987).

[121] M. D. Jones and R. C. Albers, "Spin-orbit coupling in an f-electron tight-binding model: electronic properties of Th, U, and Pu", Phys. Rev. B **79**, 045107 (2009).

[122] C. S. Lent, M. A. Bowen, J. D. Dow, R. S. Allgaier, O. F. Sankey, and E. S. Ho, "Relativistic empirical tight-binding theory of the energy bands of GeTe, SnTe, PbTe, PbSe, PbS, and their alloys", Superlattices and Microstructures **2**, 491–499 (1986).

[123] I. C. Fulga, N. Avraham, H. Beidenkopf, and A. Stern, "Coupled-layer description of topological crystalline insulators", Phys. Rev. B **94**, 125405 (2016).

[124] J. Henk and W. Schattke, "A subroutine package for computing Green's functions of relaxed surfaces by the renormalization method", Computer Physics Communications **77**, 69–83 (1993).

[125] F. Wei, S. Ma, and Z. Zhang, "Experimental observation of two types of linear magnetoresistance in topological crystalline insulator heterostructures", Journal of Physics D: Applied Physics **52**, 285301 (2019).

[126] G. Yang, J. Liu, L. Fu, W. Duan, and C. Liu, "Weak topological insulators in pbte/snte superlattices", Phys. Rev. B **89**, 085312 (2014).

[127] H. Zhang, B. Man, and Q. Zhang, "Topological crystalline insulator snte/si vertical heterostructure photodetectors for high-performance near-infrared detection", ACS Applied Materials & Interfaces **9**, PMID: 28398029, 14067–14077 (2017).

[128] C. M. Polley, R. Buczko, A. Forsman, P. Dziawa, A. Szczerbakow, R. Rechciński, B. J. Kowalski, T. Story, M. Trzyna, M. Bianchi, A. Grubišić Čabo, P. Hofmann, O. Tjernberg, and T. Balasubramanian, "Fragility of the Dirac cone splitting in topological crystalline insulator heterostructures", ACS Nano **12**, PMID: 29251489, 617–626 (2018).

[129] R. Rechciński, M. Galicka, M. Simma, V. V. Volobuev, O. Caha, J. Sánchez-Barriga, P. S. Mandal, E. Golias, A. Varykhalov, O. Rader, G. Bauer, P. Kacman, R. Buczko, and G. Springholz, "Structure inversion asymmetry and rashba effect in quantum confined topological crystalline insulator heterostructures", Adv. Funct. Mater., 2008885 (2021).

[130] J. C. Teo and T. L. Hughes, "Topological defects in symmetry-protected topological phases", Annual Review of Condensed Matter Physics **8**, 211–237 (2017).

[131] M. Geier, I. C. Fulga, and A. Lau, "Bulk-boundary-defect correspondence at disclinations in rotation-symmetric topological insulators and superconductors", SciPost Phys. **10**, 092 (2021).

[132] D. Iaia, C.-Y. Wang, Y. Maximenko, D. Walkup, R. Sankar, F. Chou, Y.-M. Lu, and V. Madhavan, "Topological nature of step-edge states on the surface of the topological crystalline insulator $\mathrm{Pb_{0.7}Sn_{0.3}Se}$", Phys. Rev. B **99**, 155116 (2019).

[133] S. Samadi, R. Rechciński, and R. Buczko, "Topological electronic structure of twin boundaries and twinning superlattices in the SnTe material class", Phys. Rev. B **107**, 205401 (2023).

[134] R. W. Cahn, "Twinned crystals", Advances in Physics **3**, 363–445 (1954).

[135] Z. Ikonic, G. P. Srivastava, and J. C. Inkson, "Electronic properties of (111) twin boundaries and twinning superlattices in lead sulfide", Phys. Rev. B **52**, 13734–13737 (1995).

[136] Z. Ikonić, G. Srivastava, and J. Inkson, "Electronic structure of AgBr (111) twin boundaries", Journal of Physics and Chemistry of Solids **62**, 579–584 (2001).

[137] D Janaszko, P Dziawa, S Kret, A Kaleta, S Kryvyi, B Kurowska, M Bilska, J Polaczyński, J Turczyński, and J Sadowski, The XVII$^{\text{th}}$ International Conference on Electron Microscopy, 2020.

[138] Z Ikonić, G. Srivastava, and J. Inkson, "Electronic properties of twin boundaries and twinning superlattices in diamond-type and zinc-blende-type semiconductors", Physical Review B **48**, 17181 (1993).

[139] I. Knez, R.-R. Du, and G. Sullivan, "Evidence for helical edge modes in inverted InAs/GaSb quantum wells", Phys. Rev. Lett. **107**, 136603 (2011).

[140] X. Qian, J. Liu, L. Fu, and J. Li, "Quantum spin Hall effect in two-dimensional transition metal dichalcogenides", Science **346**, 1344–1347 (2014).

[141] M. d. l. Mata, X. Zhou, F. Furtmayr, J. Teubert, S. Gradečak, M. Eickhoff, A. Fontcuberta i Morral, and J. Arbiol, "A review of MBE grown 0D, 1D and 2D quantum structures in a nanowire", J. Mater. Chem. C **1**, 4300–4312 (2013).

[142] Z. Li, S. Shao, N. Li, K. McCall, J. Wang, and S. X. Zhang, "Single crystalline nanostructures of topological crystalline insulator SnTe with distinct facets and morphologies", Nano Letters **13**, PMID: 24138562, 5443–5448 (2013).

[143] M. Safdar, Q. Wang, M. Mirza, Z. Wang, K. Xu, and J. He, "Topological surface transport properties of single-crystalline SnTe nanowire", Nano letters **13**, 5344–5349 (2013).

[144] M. Safdar, Q. Wang, M. Mirza, Z. Wang, and J. He, "Crystal shape engineering of topological crystalline insulator SnTe microcrystals and nanowires with huge thermal activation energy gap", Crystal Growth & Design **14**, 2502–2509 (2014).

[145] J. Shen, Y. Jung, A. S. Disa, F. J. Walker, C. H. Ahn, and J. J. Cha, "Synthesis of SnTe Nanoplates with $\{100\}$ and $\{111\}$ Surfaces", Nano Letters **14**, PMID: 24910959, 4183–4188 (2014).

[146] Y. Zou, Z. Chen, J. Lin, X. Zhou, W. Lu, J. Drennan, and J. Zou, "Morphological control of SnTe nanostructures by tuning catalyst composition", Nano Research **8**, 3011–3019 (2015).

[147] J. Sadowski, P. Dziawa, A. Kaleta, B. Kurowska, A. Reszka, T. Story, and S. Kret, "Defect-free SnTe topological crystalline insulator nanowires grown by molecular beam epitaxy on graphene", Nanoscale **10**, 20772–20778 (2018).

[148] P. Liu, H. J. Han, J. Wei, D. Hynek, J. L. Hart, M. G. Han, C. J. Trimble, J. Williams, Y. Zhu, and J. J. Cha, "Synthesis of narrow SnTe nanowires using alloy nanoparticles", ACS Appl. Electron. Mater. **3**, 184–191 (2021).

[149] A. Miller, G. Saunders, and Y. Yogurtcu, "Pressure dependences of the elastic constants of PbTe, SnTe and $Ge_{0.08}Sn_{0.92}Te$", J. Phys. C: Solid State Phys. **14**, 1569–1584 (1981).

[150] I. I. Zasavitskii, E. A. de Andrada e Silva, E. Abramof, and P. J. McCann, "Optical deformation potentials for PbSe and PbTe", Phys. Rev. B **70**, 115302 (2004).

[151] S. Rabii, "Energy-band structure and electronic properties of SnTe", Phys. Rev. **182**, 821–828 (1969).